Master's thesis

NTNU
Norwegian University of Science and Technology
Department of Physics

Lidia Luque

Multi-Instrument Investigation of Spectral Width in the Polar Ionosphere

Master's thesis in Physics

Supervisor: Lisa Baddeley and Patrick Joseph Espy

September 2020

Katie Herlingshaw

NTNU
Norwegian University of Science and Technology

UNIS

Lidia Luque

Multi-Instrument Investigation of Spectral Width in the Polar Ionosphere

Master's thesis in Physics
Supervisor: Lisa Baddeley and Patrick Joseph Espy
September 2020

Norwegian University of Science and Technology
Department of Physics

NTNU
Norwegian University of
Science and Technology

Acknowledgements

Thanks first and foremost to my supervisors Lisa Baddeley and Patrick Joseph Espy. To Lisa, for teaching me most of what I know about space physics and for all the time you have dedicated to answering my many questions, but above all, for encouraging me when nothing seemed to be going right. To Patrick, for making me choose this field, which lead me to Svalbard and its many adventures. Thanks also to Emma Bland, Noora Partamies, Katie Herlingshaw, Mikko Syrjäsuo, Dag Lorentzen and everyone else at the space physics group for answering countless questions and perhaps more importantly, being really fun to be around. Last, but certainly not least, a very special thanks to friends and family: I shudder at the thought of having had no one to whine to.

Abstract

Spectral widths are one of the parameters measured by Super Dual Auroral Radar Network (SuperDARN) radars. Although they are extensively used in literature, there is currently no consensus on the cause of the spectral width variations seen in the polar ionosphere. The goal of this thesis is to provide further insight into the causes of the spectral width variations, and specifically into the relationship between spectral widths and particle precipitation. To that end, data from three instruments with overlapping fields of view are used: the Meridian Scanning Photometer (MSP) in Svalbard, the European Incoherent Scatter Svalbard Radar (ESR) and the SuperDARN Hankasalmi radar in Finland. After processing a list of over 200 events in order to find the events with co-located data from all three instruments, we are left with 10 events. Of those, four are treated as case studies, while the rest are used in a small statistical study. We find that, for these events, the spectral widths are not strongly correlated with the electron temperatures, which are used as an ionospheric signature of particle precipitation. This suggests that processes unrelated to particle precipitation are causing the spectral width variations detected. We find evidence pointing to the role of turbulence with varying origins (velocity shears, ion up-flow and polar cap patches merging with the auroral oval) as the cause of high spectral widths in the four case studies reviewed.

Table of Contents

Abbreviations

AACGM	=	Altitude-Adjusted Corrected Geomagnetic coordinates
ACF	=	Auto-Correlation Function
BPS	=	Boundary Plasma Sheet
CME	=	Coronal Mass Ejection
CPS	=	Central Plasma Sheet
CRB	=	Convection Reversal Boundary
DaVitTpy	=	Data and Visualization Toolkit in Python
EISCAT	=	European Incoherent Scatter
ESR	=	EISCAT Svalbard Radar
EUV	=	Extreme Ultraviolet
GLAT	=	Geographic Latitude
GUISDAP	=	Grand Unified Incoherent Scatter Design and Analysis Package
IMAGE	=	International Monitor for Auroral Geomagnetic Effects
IMF	=	Intraplanetary Magnetic Field
ISR	=	Incoherent Scatter Radar
KHO	=	Kjell Henriksen Observatory
LLBL	=	Low-Latitude Boundary Layer
MLAT	=	Magnetic Latitude
MLT	=	Magnetic Local Time
MSP	=	Meridian Scanning Photometer
OCB	=	Open-Closed field line Boundary
PDS	=	Power Density Sprectrum
PMAF	=	Polarward Moving Auroral Form
PyDARN	=	Python data visualization library for SuperDARN
RST	=	Radar Software Toolkit
SuperDARN	=	Super Dual Auroral Radar Network
SW	=	Spectral Width
SWB	=	Spectral Width Boundary
UHF	=	Ultra High Frequency
ULF	=	Ultra Low Frequency
UT	=	Universal Time
VHF	=	Very High Frequency

Chapter 1

Introduction

The Earth's magnetic field protects our planet from the majority of the ionized gas that is ejected by the Sun. The field forms a protective bubble around the Earth called the magnetosphere. At certain locations, however, this ionized gas, called plasma, can enter into the magnetosphere. The magnetosphere itself consists of different plasma populations separated by so-called magnetospheric boundaries. Due to the size of the magnetosphere, studying these regions and boundaries in-situ is not practical. Fortunately, plasma is able to precipitate towards Earth in the polar regions, depositing its energy into the ionosphere, the partly ionized upper part of the atmosphere. Because the ionosphere is intimately linked to the magnetosphere, magnetospheric processes can be studied by probing the ionosphere.

Radars are one type of instrument used to study the ionosphere. The Super Dual Auroral Radar Network (SuperDARN) is an international network of high-frequency radars located in the mid-latitudes and in the polar regions. Each of the radars in the network sends signals that are backscattered by density irregularities in the ionosphere, before being received by the same radar. From this received signal, three parameters are calculated: the power of the signal, the line-of-sight velocity of the plasma and a quantity called spectral width. Mathematically, the spectral width can be though of as the width of the velocity distribution measured by the radar, and it is related to the small-scale structuring in the irregularities from which the signal backscatters.

Spectral widths have several applications. Some of the backscatter received by SuperDARN radars is not actually scattered by the ionosphere, but rather by the ground or the sea. The fitting routine used by the radars uses an algorithm where this so-called ground scatter is separated from ionospheric scatter based on low spectral widths and low line-of-sight velocities (Blanchard et al., 2009). Spectral widths are also used to infer the ionospheric footprint of various magnetospheric regions and their boundaries, particularly the open-closed field line boundary (OCB) and the cusp. The OCB is the boundary polarward of which any precipitating plasma comes directly from the Sun, without being directly affected by the magnetosphere, and the cusp is the region in the dayside into

where most of this plasma coming directly from the Sun precipitates. The first attempt at identifying a magnetospheric region through spectral widths was published in an article by Baker et al. (1995). The authors found that the distribution of spectral widths in the cusp was Gaussian with a peak around $220\,\mathrm{m\,s^{-1}}$, while spectral widths equatorward of the cusp were typically lower ($< 50\,\mathrm{m\,s^{-1}}$). However, instances of high spectral widths in this region were also found. In the nightside sector, a statistical study by Chisham and Freeman (2004) found the boundary between high and low spectral widths to be a good proxy for the OCB. However, a case study examined by Parkinson et al. (2004) showed that this spectral width boundary appears to be a better proxy for the poleward edge of the region of high conductivities in the ionosphere caused by auroral activity.

Despite the spectral width boundary being routinely used to identify the ionospheric footprints of magnetospheric boundaries, there is as of now no agreed upon cause for the increased spectral widths seen at high latitudes. Various mechanisms have been proposed, amongst others turbulence caused by Kelvin-Helmholtz instabilities (e.g. Schiffler et al. 1997), ultra low frequency waves (e.g. André et al. 2000) and low-energy (soft) particle precipitation (e.g. Baker et al. 1995). Additionally, Chisham et al. (2005a) reported an inverse relationship between the energy flux of the precipitating electrons and spectral widths, which was interpreted as an indication that high-energy precipitation suppresses spectral widths.

Moen et al. (2000) first proposed using a combination of three instruments to examine the possible relationship between particle precipitation and spectral widths: the Meridian Scanning Photometer (MSP) in Svalbard, the European Incoherent Scatter Svalbard Radar (shortened to ESR) and the SuperDARN Hankasalmi radar in Finland. The reason for using these instruments is that they have overlapping fields of view, allowing for independent datasets describing the same ionospheric volume. The ESR makes it possible to measure the electron and ion temperatures in the ionosphere, while the MSP is an optical instrument that can be used to locate the OCB.

This combination of instruments was used by Woodfield et al. (2002) to study one event in the morning sector. The authors found that the spectral width boundary was equatorward of the OCB as seen in the MSP data, and thus not a good proxy for the OCB. They went on to compare the electron temperatures measured by the ESR to the spectral widths, and found a positive correlation that they interpreted as an indication that soft electron precipitation leads to increased spectral widths.

In 2016, Chen X.C. and co-workers gathered a list of events where the MSP was turned on while ionospheric backscatter in the field of view of the MSP was recorded by the Hankasalmi radar (this list formed the basis for the Chen et al. 2016 study). This thesis uses this list of events as a starting point to continue the line of work started by Woodfield et al. (2002). The spectral widths from a series of events will be compared to both the temperatures measured by the ESR and the conductivities derived from models using ESR measurements as inputs. This, together with data from the MSP used to pinpoint the position of the radar data relative to the OCB, gives insight into the relationship between spectral widths and particle precipitation.

This thesis starts with three theoretical chapters. Chapter 2 introduces the basics of

plasma physics and the concepts needed to understand how the polar ionosphere is affected by plasma. This is followed by a discussion of the instrumentation in Chapter 3. Chapter 4 lays out the work previously done on spectral widths relevant to this thesis. In Chapter 5 the experimental methodology is presented, before presenting and discussing the results in Chapter 6. Finally, a summary is given in Chapter 7 which ends by suggesting some possibilities for further research.

Chapter 2

Background Theory

In this chapter, we first go through the basics of plasma physics before diving into three elements that interact to give rise to the processes studied in this thesis: the solar wind, the magnetosphere and the ionosphere. Unless otherwise stated, the material in this chapter is based on two books: *Physics of the Upper Polar Atmosphere* by Brekke (2013) and *Introduction to Space Physics* by Kivelson and Russell (1995). For section 2.1, the book *Basic Space Plasma Physics* by Baumjohann and Treumann (1997) has also been used as background material.

2.1 Space plasma

Most of the visible universe, up to 99% according to some estimates, is made of plasma (Gurnett and Bhattacharjee, 2005). A plasma is a gas so hot that at least a portion of its constituent atoms are slit up into ions and electrons that move as independent particles. Because plasma is made of charged particles, it interacts strongly with electrostatic and electromagnetic forces, which can lead to complex and interesting behaviours.

2.1.1 Definition of a plasma

For a gas of charged particles to be a plasma, it must fulfil two requirements: the plasma must be *quasineutral* and consist of *free particles*. Quasineutrality means that the plasma, on large enough scales, is charge neutral: it has equal numbers of positive and negative charge carriers. At small scales, charges might separate, but this will be readily neutralized since plasmas are very good electrical conductors. Thus, as a whole, a plasma must be electrically neutral. For a particle to be considered a free particle, its motion must be (close to) free from the influence of other charged particles nearby. That is to say, the particle's

average electric potential energy due to its nearest neighbour must be much smaller than its random kinetic (thermal) energy. Note that the gas does not need to be fully ionized to be considered a plasma. Indeed, the plasma in Earth's ionosphere consists of a mixture of neutrals and ionized particles, as we will see in section 2.4.

2.1.2 Debye length

The Debye length is the distance from an ionized particle in a plasma where the electric potential caused by the particle decreases by $1/e$. In a plasma the Debye length λ_D is approximated by

$$\lambda_D \approx \sqrt{\frac{k_B \epsilon_0 T_e}{n_e e^2}} \tag{2.1}$$

where k_B is the Boltzmann constant, ϵ_0 is the vacuum permittivity, e the electric charge, T_e denotes the electron temperature and n_e is the number density of electrons. The importance of the Debye length relies on it being the minimum distance over which a plasma can exhibit collective behaviour. If a plasma phenomenon varies over scale lengths smaller than or similar to the Debye length, the plasma at the scale of interest may not be neutral, and the ions and electrons will behave as individual particles.

2.1.3 Electron plasma oscillations and Langmuir waves

The electron plasma frequency is the most fundamental time scale in plasma physics. When a plasma is disturbed by an external force, quasineutrality breaks down at small scales. The electrons are accelerated by the resulting electric field, while the much more massive ions remain nearly static. The electrons' momentum makes them overshoot, initiating an oscillation. The frequency of this oscillation, the electron plasma frequency ω_{pe} (often shortened to plasma frequency) is given by

$$\omega_{pe} = \sqrt{\frac{n_e e^2}{m_e \epsilon_0}} \tag{2.2}$$

where m_e denotes the electron mass. Equation 2.2 assumes the electrons to be "cold", meaning it does not take into account their thermal motion. When we allow for thermal motion, the oscillations propagate forming a *Langmuir wave*. The frequency ω_{pl} and wavenumber k_{pl} of the Langmuir wave are related by its dispersion relation as follows:

$$\omega_{pl} = \omega_{pe}(1 + 3k_{pl}^2 \lambda_D^2) \tag{2.3}$$

Langmuir waves are useful for measuring the density of the plasma in the ionosphere, as we will see in section 3.3.

2.1.4 Ion acoustic waves

Much like acoustic waves traveling in a neutral gas, longitudinal waves called *ion acoustic waves* can travel through a plasma. In the limit where the wavelength is much larger than the Debye length ($k_{ia}^2\lambda_D^2 \ll 1$ where k_{ia} is the wavenumber of the ion acoustic wave), the dispersion relation is given by

$$\omega_{ia} \approx kC_s = k_{ia}\sqrt{\frac{k_B T_e + 3k_B T_i}{m_i}} \tag{2.4}$$

where ω_{ia} is the frequency of the wave and $C_s = \sqrt{(k_B T_e + k_B 3T_i)/m_i}$ is the ion acoustic speed with the electron and ion temperature denoted T_e and T_i respectively. Ion acoustic waves make it possible to measure a variety of plasma properties in the ionosphere, as we will see in section 3.3.

2.1.5 Particle motion in magnetized plasma

The full momentum equation for a plasma species is given by the gravitational force, the pressure gradient force, the electromagnetic forces and the kinetic forces due to collisions between the given species and other species (both plasma and neutral). In many plasmas the electromagnetic forces are, by far, the biggest driver of particle motion. When the dominant force involved is the Lorentz force, the momentum equation for a plasma particle is reduced to

$$m\frac{d\boldsymbol{v}}{dt} = q\left(\boldsymbol{E} + \boldsymbol{v} \times \boldsymbol{B}\right) \tag{2.5}$$

where $\boldsymbol{v}$ is the velocity of the particle, q is its charge, $\boldsymbol{E}$ denotes the electric field and $\boldsymbol{B}$ the magnetic field.

In the absence of an electric field and given a constant magnetic field, equation 2.5 results in a circular motion around a magnetic field line, since the force exerted on the charged particle by the magnetic field is always perpendicular to its velocity. Since the force is proportional to the charge of the particle, electrons gyrate clockwise while ions gyrate in an anticlockwise orbit. With $\boldsymbol{v}_\perp$ denoting the velocity component perpendicular to $\boldsymbol{B}$, the right hand side of equation 2.5 becomes $q\boldsymbol{v}_\perp\boldsymbol{B}$. This force and the centripetal force must balance which, using scalar quantities for simplicity, gives

$$qv_\perp B = \frac{mv_\perp^2}{r_g} \tag{2.6}$$

where r_g is the gyroradius. Solving for r_g gives

$$r_g = \frac{mv_\perp}{qB} \tag{2.7}$$

which shows that ions, which are much heavier than electrons, will gyrate around magnetic field lines with a much larger radius than electrons. The angular frequency of the particle,

also called the gyrofrequency ω_g, is given by

$$\omega_g = \frac{qB}{m} \tag{2.8}$$

Note that the gyrofrequency is independent of the velocity. Due to the mass dependence, electrons will gyrate faster than ions.

So far we have seen how charged particles gyrate around a point in space. The total movement of a plasma particle can be seen as a superposition of this gyration and a drift. If the plasma particle has an initial velocity with a component parallel to $\boldsymbol{B}$, the particle will drift along the magnetic field line as it gyrates, resulting in a helical orbit. Particles can also drift perpendicular to the magnetic field. There are several drivers for this drift, amongst others a gradient or a curvature in the magnetic field, an external force such as gravity and the presence of an electrical field. We will concentrate on the later since it is of greater relevance in this thesis.

We now assume that both $\boldsymbol{B}$ and $\boldsymbol{E}$ are constant and not equal to zero. Equation 2.5 is a first order linear differential equation and as such the solution is a superposition of the particular and the homogeneous solution. Since we are only interested in the steady-state motion of the particle (that is, $d\boldsymbol{v}/dt = 0$), finding the homogeneous solution is enough. To do so we need to solve $q\left(\boldsymbol{E} + \boldsymbol{v_D} \times \boldsymbol{B}\right) = 0$ for $\boldsymbol{v_D}$, the drift velocity. Rearranging and taking the cross product of both sides with $\boldsymbol{B}$ gives $\boldsymbol{E} \times \boldsymbol{B} = -\left(\boldsymbol{v_D} \times \boldsymbol{B}\right) \times \boldsymbol{B} = \boldsymbol{v_D}B^2 - \boldsymbol{B}\left(\boldsymbol{v_D} \cdot \boldsymbol{B}\right)$. We can drop the term $\boldsymbol{B}\left(\boldsymbol{v_D} \cdot \boldsymbol{B}\right)$ since it is a vector along $\boldsymbol{B}$, which is not a component of $\boldsymbol{E} \times \boldsymbol{B}$. Rearranging results in

$$\boldsymbol{v_D} = \frac{\boldsymbol{E} \times \boldsymbol{B}}{B^2} \tag{2.9}$$

where $\boldsymbol{v_D}$ is the drift velocity of a plasma particle in a uniform electric and magnetic field, called the E×B-drift. The total motion of said particle will be a superposition of the E×B-drift and the gyration around $\boldsymbol{B}$ as seen in figure 2.1. The E×B-drift is independent of the charge and thus ions and electrons move in the same direction and with the same drift velocity, but with different gyroradiuses and gyrofrequencies and seen in equations 2.7 and 2.8.

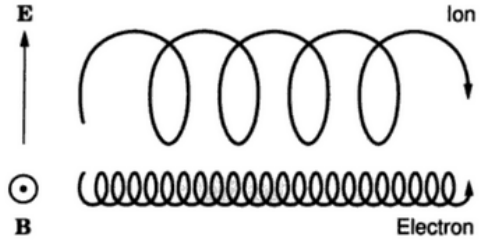

Figure 2.1: Motion of an ion and an electron in an electric field perpendicular to the magnetic field. Figure taken from Baumjohann and Treumann (1997).

In the upper atmosphere, in the so-called F-region, the plasma is nearly collisionless

and the assumption that the electromagnetic forces dominate holds. The horizontal plasma drift in this region is thus accurately described by the E×B-drift equation (equation 2.9).

2.1.6 Frozen-in field

The induction equation, derived from Maxwell's equations and Ohm's law, states that local changes in the magnetic field are caused by either convection of the plasma or by diffusion

$$\frac{\partial \boldsymbol{B}}{\partial t} = \nabla \times (\boldsymbol{v} \times \boldsymbol{B}) + \frac{1}{\mu_0 \sigma} \nabla^2 \boldsymbol{B} \tag{2.10}$$

where $\boldsymbol{v}$ is the velocity of the plasma, μ_0 is the vacuum permeability and σ is the electrical conductivity, which is assumed to be constant. Convection and diffusion are described respectively by the first and the second term on the right-hand side. When $\sigma \to \infty$, the diffusion term disappears and we are left with only the convection term

$$\frac{\partial \boldsymbol{B}}{\partial t} = \nabla \times (\boldsymbol{v} \times \boldsymbol{B}) \tag{2.11}$$

It can be shown that this means that a movement in the magnetic field must imply a movement in the plasma, and correspondingly, moving plasma transports the field line with it. This is called the Alfvén's frozen-in theorem, often shortened to frozen-in theorem. Plasma with infinite conductivity satisfies the frozen-in condition, and thus can move along magnetic field lines as seen in section 2.1.5, but not across them.

2.1.7 Magnetic reconnection

As we will see in section 2.3, the Earth is surrounded by a magnetic field called the magnetosphere. Straight forward application of the frozen-in field theorem, which mostly holds given the very large conductivities in these regions, dictates that solar wind plasma and magnetospheric plasma cannot mix, since they are frozen-in to their respective magnetic field lines. We know based on observations, however, that they do. The aurora is one example of the results of solar wind gaining access to the magnetosphere. Magnetic reconnection is a process during which the frozen-in field condition breaks down, resulting in the mixing of plasma across magnetic field lines which would otherwise be prohibited.

Magnetic reconnection is not yet well understood, but the basic concept is as follows (adapted from Clausen 2014): When plasmas carrying antiparallel magnetic field lines are brought together, a strong current sheet is established. This is described by Ampere's law which, in the case of a static electric field reads $\oint \boldsymbol{B} \cdot ds = \mu_0 I_{enc}$. It states that the line integral of the magnetic field around a closed loop is proportional to the electric current flowing through the loop. The currents needed to sustain the opposing magnetic fields become so strong that even plasma with close to infinite conductivity cannot sustain them and the current locally breaks down, which is equivalent to a counter current being created. The superposition of the original current and the locally created opposing current gives rise to a magnetic quadrupole as shown in figure 2.2 at $t > 0$. The previously opposing

magnetic field lines have now merged, and the new field lines and the plasma that carried them are expelled along the perpendicular directions due to the tension force generated. This process converts magnetic potential energy into kinetic and thermal energy, and thus the outflowing plasma is both hotter and faster compared to the plasma inflow.

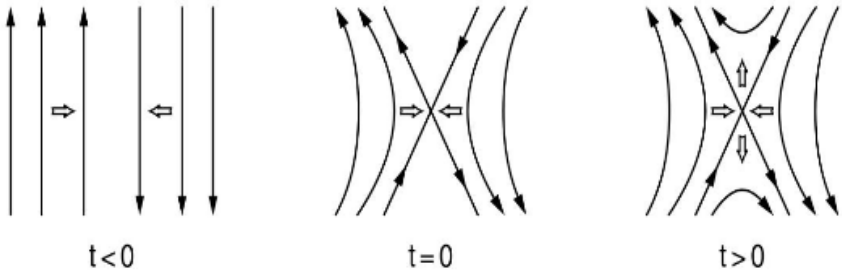

Figure 2.2: Oppositely directed magnetic field lines are shown reconnecting at $t = 0$. In the merging region plasma diffusion occurs and magnetic potential energy is converted to kinetic and thermal energy. The plasma influx and outflux is shown by the arrows at $t > 0$. Figure taken from Baumjohann and Treumann (1997).

Magnetic reconnection is crucial in many ionospheric processes. Is allows mixing of plasma across boundaries, letting the solar wind into the magnetosphere while increasing its energy. It also drives the Dungey cycle, as we will see in section 2.3.1.

2.2 The solar wind

The Sun radiates with a spectrum very close to that of a black body at $5780\,\mathrm{K}$, matching the temperature of the layer in the Sun called the photosphere from which the photons escape. Above the photosphere, the temperature decreases and creates the convection zone where hot plasma rises, cools by radiating some of its heat into space and heats as it sinks to start the cycle again. Yet above that, the Sun's outer layer called the corona is so hot (temperatures exceed $1 \times 10^6\,\mathrm{K}$) that some electrons have enough kinetic energy to escape the Sun's atmosphere, pulling the ions and the frozen-in magnetic field with them. This stream of plasma is called the solar wind and consists of electrons, protons and alpha particles with energies of about $1\,\mathrm{eV}$ to $10\,\mathrm{eV}$ with typical velocities of $300\,\mathrm{km\,s^{-1}}$ to $500\,\mathrm{km\,s^{-1}}$. The associated magnetic field frozen in to the plasma is often called the interplanetary magnetic field, or IMF for short.

The Sun's magnetic field has a complex structure with regions of concentrated magnetic field flux that inhibit convection, thus creating cooler darker areas in the photosphere called *sunspots*. Magnetic field lines above sunspot groups can form loops that suddenly break off through reconnection (see section 2.2) releasing bubbles of high density high velocity solar wind consisting of plasma frozen in to the magnetic field. These events are called coronal mass ejections (CMEs). CMEs take an average of 3 to 4 days to reach Earth. The $\sim$11 years periodicity in the variations in the magnetic field is called the solar cycle

and affects the number of solar spots present and thus the likelihood of CME events. As of 2020 the Sun is close to its solar minimum with few sunspots and a relatively calm solar wind leading to a decrease in auroral activity.

The IMF is a vector quantity with three perpendicular components defined from an Earth frame of reference, as can be seen in figure 2.3. The first two components are parallel to the ecliptic, with B_x pointing along the noon-midnight meridional plane towards the Sun and B_y 90° eastward from B_x. B_z is perpendicular to both B_x and B_y with the positive direction being defined northwards.

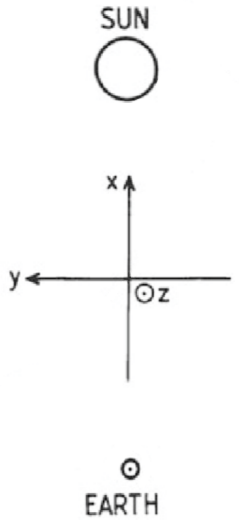

Figure 2.3: Components of the IMF with the Sun and the Earth as reference. Figure modified from Baumjohann and Treumann (1997).

2.3 The magnetosphere

Most of the Earth's magnetic field is produced by a dynamo process in the liquid layer of Earth's core. It can be approximated as the field of a magnetic dipole located at the center of the Earth and offset by about 10° from the Earth's axis of rotation. The magnetic poles are therefore not co-located with the geographic poles. Earth's magnetic field is continuously changing its orientation and the magnetic north pole has been moving roughly towards the geographic north pole since the end of the 19th century. The magnetic field strength is approximately $6 \times 10^4\,\mathrm{nT}$ at the poles and decreases to approximately $3 \times 10^4\,\mathrm{nT}$ at the equator. The dipole approximation is used to define a coordinate system of magnetic coordinates. In this thesis we will often use the magnetic latitude (MLAT), which is analogous to the geographic latitude, except that it is defined relative to

the magnetic poles instead of the geographic poles.

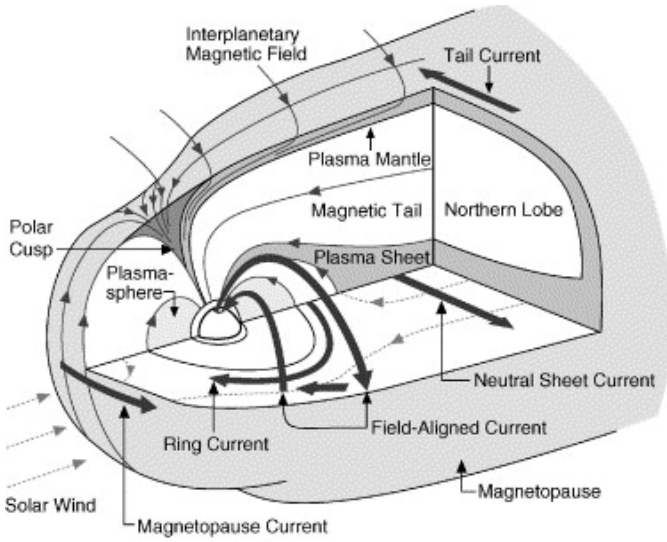

Figure 2.4: Schematic view of the magnetosphere. Figure taken from Russell (2001).

The dipole approximation does not, as shown in figure 2.4, give an accurate enough description of the magnetosphere, which is the cavity in which the Earth's magnetic field dominates. The boundary of the magnetosphere is defined to a first order by the pressure balance between the IMF on the one side and the magnetic pressure from the Earth's magnetic field on the other. The magnetosphere acts in much the same way a stone in a river makes water flow around it. In the dayside, the solar wind compresses the magnetosphere creating the *magnetopause* and in the nightside, it drags it to form the *magnetic tail*. The solar wind is supersonic and its deceleration creates a bow shock sunward of the magnetopause which heats the plasma and slows it down enough to be deflected by the magnetosphere. This bubble of decelerated plasma is called the *magnetosheath*. Waves called Kelvin-Helmholtz instabilities (KHI) are formed in the magnetopause, driven by the shear between magnetosheath and magnetospheric plasma. These can cause turbulence in the ionosphere, as we will see in section 4.2.

Although most of the solar wind does indeed flow around the magnetosphere, some is able to diffuse through the magnetopause due to magnetic reconnection. This plasma can precipitate into the ionosphere to the *polar cusp*, the ionospheric footprint of the funnel-like region in the poles where magnetosheath plasma has direct access to the ionosphere. It can also collect in the *plasma sheet*, the region inside the magnetic tail containing a relatively dense plasma that plays an important role in the nightside aurora, as we will see in section 2.4.1.

2.3.1 The Dungey cycle

The Dungey cycle is the process by which magnetic reconnection causes the convection of the Earth's magnetic field lines. It is named after J.W. Dungey who first proposed the mechanism in 1961. To understand the Dungey cycle we first need to understand what is meant by open and closed field lines. Without the interaction with the IMF, all magnetic field lines in Earth's magnetic field would have one footprint in the northern hemisphere, and one in the southern hemisphere. These are the so called *closed field lines*, where closed refers to the fact that they start and end on Earth. When the IMF and a closed field line from the Earth merge through reconnection, the newly formed magnetic field line has a footprint in the ionosphere and another in the Sun. These are called *open field lines*.

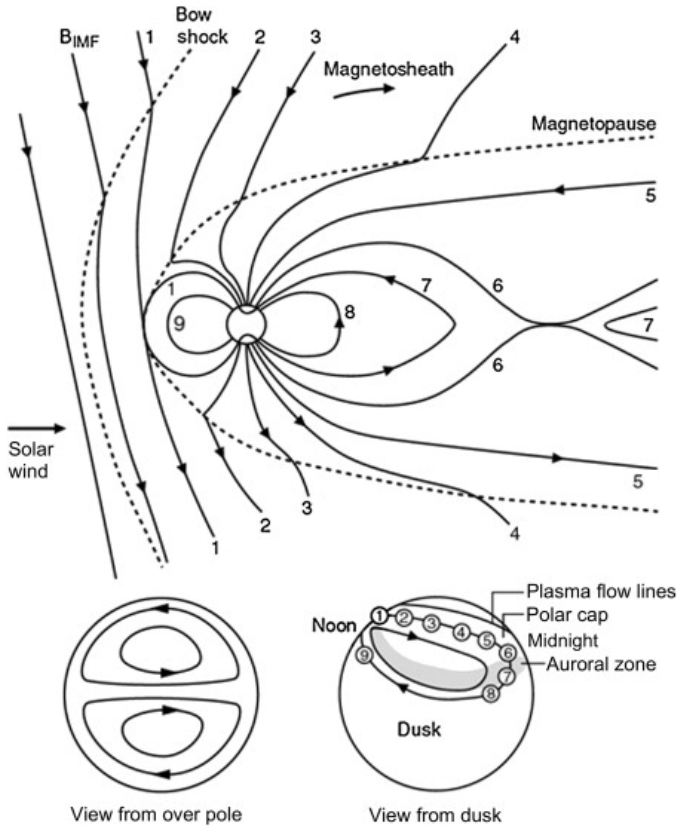

Figure 2.5: Schematic view of the Dungey cycle. Figure adapted from Kivelson and Russell (1995).

Figure 2.5 shows the time history of a magnetic field line as it interacts with the magnetosphere. The numbers 1-9 can be thought of as a time label, t. At the equatorial plane, the Earth's magnetic field points northwards, meaning that an IMF with a negative (southward) B_z component will merge through reconnection at $t = 1$. The newly opened magnetic field lines are dragged anti-sunward due to the flow of the solar wind (which

has the IMF embedded in it), as shown at t = 2-5. Once in the magnetotail, as the field lines are stretched further, the field lines with footprints in opposing hemispheres at $t = 6$ have opposing magnetic field directions and recombine. The resulting closed field line shortens due to magnetic tension and moves through the dawn or the dusk sector towards the initial position at $t = 1$. The ionospheric footprint of the Dungey cycle is a two celled convection pattern that goes from noon to midnight across the *polar cap* and back to noon through lower latitudes. The polar cap is the ionospheric region centered at the magnetic pole within which the magnetic field lines are open. Since the plasma in the upper regions of the ionosphere is frozen-in to the magnetic field, it will follow this convection pattern. Velocities of a few hundred meters per second are typical.

2.4 The ionosphere

In 1901 italian Guglielmo Marconi transmitted radio waves from England to Canada. If radio waves followed a straight line, the Earth's curvature would have stopped them. British scientists Oliver Heaviside and Arthur Kennelly concluded that the waves must have been reflected by an ionized layer in the atmosphere, thus discovering what we now call the ionosphere. The theory in this section is adapted from Kelley (2009) and Moen (2004).

The ionosphere is the upper region in the atmosphere. It consists mainly of neutral elements, but unlike the lower parts of the atmosphere, it also has a significant amount of ionized elements. This ionized gas is approximately charge neutral on the length scales of interest and can therefore be considered a plasma. The presence of plasma gives the ionosphere distinct properties, such as affecting the propagation path of radio waves. This allows us to study it with the help of radar, as we will see in section 3.2 and 3.3.

Since the ionosphere is characterized by the presence of plasma, it makes sense to use the plasma density to look at its structure. Figure 2.6 shows a typical altitude profile of electron density in the mid-latitudes. As seen in the figure, the electron density at noon is substantially higher than the electron density at midnight at all altitudes. This is because EUV (Extreme Ultraviolet) radiation from the Sun is the main driver for the production of plasma. In the high-latitude ionosphere impact ionization is also a very important ionization driver, which will be discussed in section 2.4.1. The increase in electron density during solar maximum is also caused by increased levels of EUV radiation, as the Sun produces more EUV radiation during solar maximums.

As seen in figure 2.6, the ionosphere can be divided into three regions: The F region (150-500km), the E region (95-150km) and the D region (60-95km). The altitude ranges are approximate and slightly different ranges are given in different publications.

The F region is where the highest electron densities are found. During the day EUV radiation from the Sun with wavelength $10\,\mathrm{nm} < \lambda < 90\,\mathrm{nm}$ ionizes some of the neutrals converting them to plasma. The two main neutral components of the F region are O and N_2. The primary ions O^+ and $N_2{}^+$ quickly react with neutrals to form the most abundant ions in this region: O^+, $O_2{}^+$ and NO^+. During the night, some of the plasma recombines to form neutrals, thus lowering the electron density. However, this effect is less pronounced

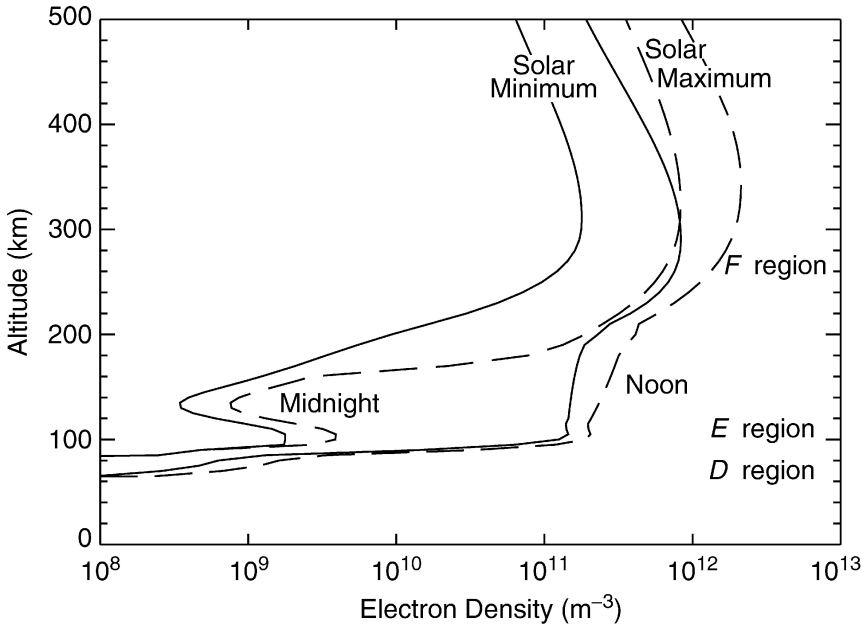

Figure 2.6: Altitude profile of electron density in the ionosphere at noon and midnight during solar minimum (solid lines) and solar maximum (dashed lines) with the D, E and F regions indicated. The measurements are taken at the Arecibo Observatory in Puerto Rico. Figure taken from Richmond (2007).

than in the lower regions of the ionosphere due to lower neutral densities which give a lower recombination rate. This results in a relatively small change of the electron densities between midnight and noon as seen in figure 2.6. The low density makes ion-neutral collisions rare and thus the conductivity of the plasma in this region is high enough that the frozen-in condition applies. During daytime or during periods of high geomagnetic activity the electron density can reach values in the order of $10^{12}\,\mathrm{m}^{-3}$.

In the E region the neutral atmosphere is mainly composed of O_2 and N_2. These are ionized by X-rays ($1\,\mathrm{nm} < \lambda < 10\,\mathrm{nm}$) and ultraviolet radiation ($100\,\mathrm{nm} < \lambda < 150\,\mathrm{nm}$) to form the primary ions $O_2{}^+$ and $N_2{}^+$. As it is the case in the F region, the $N_2{}^+$ reacts with O to form NO^+ which, together with $O_2{}^+$, are the dominating ions in the E region. There are sometimes thin layers formed within the E region called *sporadic E-layers*. These are caused by the ablation of meteors and consist of metal ions. As seen in figure 2.6, the electron density decreases sharply at night due to recombination. This effect is much stronger than in the F region due to the higher neutral density at these altitudes.

The main source of ionization in the upper D region is the Lyman-alpha spectral line ($\lambda = 121.6\,\mathrm{nm}$) and X-rays, while in the lower D region high-energy cosmic radiation dominates. Given the relatively high neutral densities, the primary ions react to form complex molecules with both positive as well as negative charge. During night only the cosmic radiation remains as an ionizing source, and a high recombination rate causes the

D region to nearly disappear. One important exception is during the rare but powerful solar proton events, which cause strong ionization in the polar cap regions independent of the time of the day.

2.4.1 The high latitude ionosphere

Particle precipitation

In the high latitudes, polarward of around 65° latitude, ionization in the ionosphere is not only caused by solar radiation and impact ionization from cosmic radiation, but also from impact ionization from the solar wind plasma. Because the magnetosphere is highly asymmetrical, as seen in section 2.4, the dayside and the nightside polar ionosphere are affected differently by incoming particles originating in the solar wind, so-called *particle precipitation*. These precipitating particles and the subsequent particle cascade ionize and excite atoms in the ionosphere, mainly in the E and lower F regions. The loss of this excitation energy through the emission of a photon in the visual spectrum causes the aurora. The green and the red aurora both come from different excitations of the oxygen atom, with the green spectral line at 5577 Å appearing from 100km to 200km, while the red spectral line at 6300 Å occurs mostly above that. Excited nitrogen produces a blue line at 4278 Å and tends to appear below 100km. As expected from the spectral lines, the excitation of nitrogen requires the most energetic particle precipitation, with green in second place and red happening from lower precipitation energies. As seen in figure 2.7, the aurora is usually located in an oval centered around the magnetic pole, but displaced slightly towards the nightside.

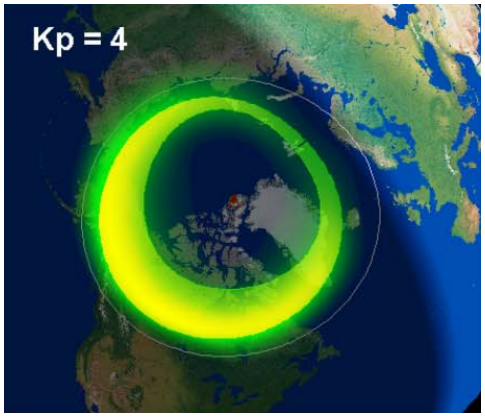

Figure 2.7: Predicted auroral oval at kp=4 (the kp index ranges from 0-9 and describes the disturbance of the Earth's magnetic field caused by the solar wind). The red dot was the position of the magnetic north pole in 2012. Figure taken from Sigernes et al. (2012).

Figure 2.8 shows a statistical average of the precipitation regions in the polar ionosphere based on satellite data (for negative IMF B_z and B_y). The map is centered at

the magnetic pole and shows a magnetic coordinates grid down to 60° magnetic latitude. Magnetic local times (MLT) are shown on the edge of the map. 12MLT, called magnetic noon, is the time at which an observer would be exactly between the magnetic pole and the Sun. 00MLT is magnetic midnight, where the magnetic pole is between an observer and the Sun, and 06MLT and 18MLT are often referred to as dawn and dusk respectively. From here on, the terms *dayside* and *nightside* are used to refer to MLTs around magnetic noon and midnight respectively. The different regions have different particle precipitation populations that can be mapped to different parts of the magnetosphere. In the nightside, the auroral oval maps to the plasma sheet (Boundary Plasma Sheet, BPS, and Central Plasma Sheet, CPA). This is due to reconnection in the plasma sheet in the magnetotail, also referred to as nightside reconnection. As discussed in section 2.2, the process of magnetic reconnection accelerates plasma along the resulting closed magnetic field line towards the ionosphere. Most of this plasma has high energies and precipitates in the nightside ionosphere. The particles that do not precipitate into the ionosphere after this initial injection undergo a gradient-curvature drift motion with ions drifting westward and electrons drifting eastward (the gradient-curvature drift, unlike the E$\times$B-drift, separates particles of opposite charges). At the same time, a process called pitch angle scattering causes the particles to precipitate into the ionosphere, where they create further auroral emissions in the flanks (MLTs around dawn and dusk). The aurora due to particles on closed magnetic field lines (from the plasma sheet) is thus more intense in the nightside, because of the higher particle flux in that region. In the dayside, particle precipitation happens also on open field lines. The dayside reconnection (merging) of the southward pointing IMF with the closed field lines from the magnetosphere does not lead to the same energy release as nightside reconnection due to lower magnetic tension forces, and the plasma that precipitates on these now opened field lines has lower energies. These magnetic field lines map first to the cusp where the precipitating particles, due to their lower energy, cause the red dayside aurora typical of this region. As the field lines convect through the polar cap, very low energy and low density plasma precipitates in this region. This precipitation is often called polar rain (P Rn). Note that only the area with the most dense polar rain is shown in figure 2.8, but it is present in the whole polar cap as noted by Newell et al. (2004). It is worth noting that the location of the cusp is not static and can in fact move several hours in MLT depending on the IMF B_y component. Figure 2.8 shows the average cusp location when $B_y < 0$, while a positive B_y will move the cusp towards dusk. In the dayside and in the flanks, plasma from the inner region of the magnetopause, called the low latitude boundary layer (LLBL), also contributes to the particle precipitation. This precipitation is more energetic than cusp precipitation, but less energetic (on average) than precipitation in the nightside.

The open-closed field line boundary

The ionospheric footprint of the boundary between the closed field lines at lower latitudes and the first open field lines at higher latitudes is called the open-closed field line boundary, or more simply the open-closed boundary (OCB). The polar cap is defined as the region inside the OCB (and is thus on open field lines) and the ionospheric footprint of the cusp is a small region in the dayside of the polar cap. The size of the polar cap is a function

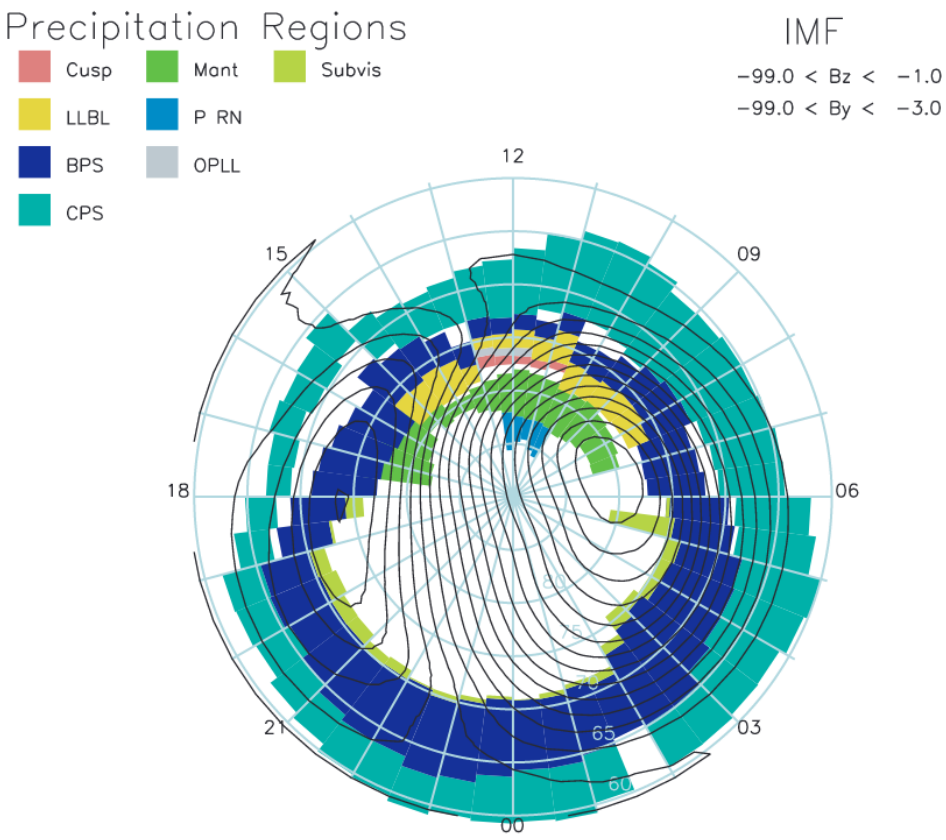

Figure 2.8: Magnetic latitude map of ionospheric precipitation according to the magnetospheric source region with superimposed typical convection cells. Data is an average over 11 years, using satellite data for the particle precipitation map and SuperDARN data for the convection cells, for negative B_z and B_y components of the IMF. Figure taken from Newell et al. (2004).

of the open magnetic flux within it: the polar cap expands, moving the OCB equatorward, when flux is added and contracts when it is removed, moving the OCB polarward. The mechanism adding open flux to the polar cap is dayside reconnection, which happens when the B_z component of the IMF is negative. In general, this leads to an equatorward movement of the OCB and thus the cusp, since the equatorward boundary of the cusp is the OCB. In the nightside, open flux is removed through reconnection in the magnetotail. Increased nightside reconnection rates during *substorms*, events where a disturbance in the magnetotail intensifies reconnection leading to stronger nightside auroras, removes open flux from the polar cap and leads to a polarward movement of the OCB. In the nigthside, the polarward edge of the auroral oval is located at the OCB.

While measuring the OCB directly is not possible, determining it through a proxy such as auroral emission lines or electron temperatures is. Rodger (2000) gives a review

of several ground based techniques used to detect the OCB. Here I will consider the three most relevant for this thesis.

Electron density and electron temperature measurements from incoherent scatter radars (see section 3.3) can be used to distinguish between the soft polar rain in the polar cap, the particle precipitation in the cusp ($< 1\,\mathrm{keV}$), and the high-energy (> 1–$10\ \mathrm{keV}$) particle precipitation from the BPL and CPS in the nightside. Particle precipitation is related to the electron density and temperature through collisional ionization, which causes the electron densities to increase, and collisional heating, which leads to increases in the electron temperatures. Precipitation in the cusp typically results in electron temperature and density enhancements in the F-region (see figure 3.9 for an example of cusp aurora as detected by the ESR radar). In the dayside, the equatorward boundary of these increases can be used as a proxy for the OCB. High-energy precipitation in the nightside typically causes electron density enhancements in both the F- and the E-region and electron temperature enhancements in the F-region (see figure 3.8 for an example of nightside aurora). Ion temperature enhancements due to frictional heating can also occur in the nightside aurora. Since polar rain is too low in energy and flux to cause significant enhancements, the polarward boundary in the high-energy precipitation signature can be used as a proxy for the OCB in the nightside. While in principle it is possible to place the OCB as explained above, in practice we usually only get one or two point-like measurements when using an incoherent scatter radar and often the best we can do is to estimate if particles are precipitating on open or closed field lines. It is important to note that closed field lines can exist in regions without current particle precipitation, thus making it hard to know if a lack of temperature and density enhancements in the nightside is due to open field lines or closed field lines without significant precipitation. Likewise, in the dayside, particle precipitation in the cusp is not necessarily significant enough to lead to the expected signature.

Optical measurements from, for example, a meridian scanning photometer (see section 3.4) can also be used to find a proxy for the OCB. Particle precipitation on closed field lines satisfies $I_{6300}/I_{5577} \ll 1$, meaning the intensity of the green emission line is much stronger than the intensity of the red emission line. This is because exciting oxygen to emit the $5577\,\text{Å}$ spectral line requires high-energy precipitation, while exciting it to emit the $6300\,\text{Å}$ requires significantly lower energies. Cusp aurora is mostly red (i.e. $I_{6300}/I_{5577} \gg 1$) since it is on open field lines, while particle precipitation equatorward of the cusp (hence on closed filed lines) is more energetic and therefore dominated by the green emission line. On closed field lines in the nightside, precipitation of even higher energies makes the aurora mostly green, with a sharp decrease in the intensity of the auroral emissions polarward of the OCB, since polar rain is not associated with emissions. Observations of the main auroral spectral lines as a function of latitude can thus be used as a proxy for the OCB. However, this method also requires there to be a particle precipitation flux high enough to make the resulting emission lines detectable, which is not always the case. When there is no dayside reconnection, cusp aurora will not be visible and similarly, low rates of nightside reconnection can make it impossible to detect auroral emissions.

Last but not least, variations in the spectral width parameter measured by coherent scatter radars can also be used to find a proxy for the OCB. This will be discussed in section 4.1.

2.4.2 Ionospheric conductivity

The ionospheric conductivity, measured in Siemens per meter (S/m), is a quantification of how easy it is for the ions and electrons to flow through the neutral atmosphere. At any point in the ionosphere, the current density is given by

$$\boldsymbol{j} = qn_e(\boldsymbol{v_i} - \boldsymbol{v_e}) \tag{2.12}$$

where n_e is the electron number density (quasi neutrality is assumed), q is the elementary charge, $\boldsymbol{v_i}$ is the ion velocity and $\boldsymbol{v_e}$ is the electron velocity. The full expression for the ion and electron velocities consist of three components, a component parallel to the electric field, a component parallel to the magnetic field and a component perpendicular to both the electric and the magnetic field (see chapter 5 in Brekke (2013) for the expressions and their derivations). Substituting $\boldsymbol{v_i}$ and $\boldsymbol{v_e}$ into equation 2.12 gives

$$\boldsymbol{j} = \sigma_P \boldsymbol{E}_\perp - \sigma_H \frac{\boldsymbol{E} \times \boldsymbol{B}}{B} + \sigma_\parallel \boldsymbol{E}_\parallel \tag{2.13}$$

where $\boldsymbol{E}_\perp$ and $\boldsymbol{E}_\parallel$ are the electric field components perpendicular to and parallel to $\boldsymbol{B}$. σ_P, σ_H and $\sigma_\parallel$ are the Pedersen, Hall and parallel conductivities respectively given by

$$\sigma_P = \frac{qn_e}{B}\left(\frac{k_e}{1+k_e^2} + \frac{k_i}{1+k_i^2}\right) \tag{2.14}$$

$$\sigma_H = \frac{qn_e}{B}\left(\frac{k_e^2}{1+k_e^2} - \frac{k_i^2}{1+k_i^2}\right) \tag{2.15}$$

$$\sigma_\parallel = \frac{qn_e}{B}(k_e + k_i) \tag{2.16}$$

Here, k_i and k_e are the ion and electron mobility coefficients:

$$k_i = \frac{\omega_i}{\nu_{in}} = \frac{qB}{\nu_{in} m_i} \tag{2.17}$$

$$k_e = \frac{\omega_e}{\nu_{en}} = \frac{qB}{\nu_{en} m_e} \tag{2.18}$$

where ω_i and ω_e are the gyrofrequencies as given in equation 2.8 and ν_{in} and ν_{en} are the collision frequencies between ions and neutrals and electrons and neutrals respectively. There are several methods to approximate the values of ν_{in} and ν_{en} in the ionosphere. In this thesis, the conductivities used have been calculated by using the expressions for collision frequencies as derived in Schunk and Nagy (2000) (see table 4.5 and 4.6 in the book). These expressions are a function of the densities of the species present and the ion, electron, and neutral temperatures.

Figure 2.9 shows an example of the altitude profiles from the three conductivities as derived from measurements by the EISCAT radar in Tromsø. Particle precipitation enhances electron densities, which in turn can increases the conductivities by a factor of 10 compared to a quiet time baseline. The maximum Hall conductivity is close to to the peak in the electron density profile, while the peak in the Pedersen conductivity happens at higher altitudes.

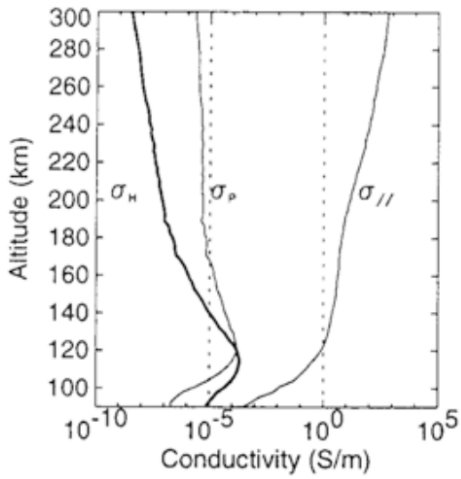

Figure 2.9: Example of Pedersen, Hall and parallel conductivity altitude profiles. Figure taken from Brekke (2013)

Chapter 3

Instrumentation

In this thesis we use three instruments to observe the high latitude ionosphere: A coherent scatter radar, an incoherent scatter radar and a meridian scanning photometer. We will start by describing some general radar physics before explaining the principles of how the two types of radar work. The theory in sections 3.1 and 3.2 is adapted from Chapter 2 in the PhD thesis by Bland (2016). The theory in section 3.3 is adapted from the compendium *UNIS AGF223: Radar Systems for Ionospheric Research* by Baddeley (2019). At the end of this chapter we describe the workings of the meridian scanning photometer, which is an optical instrument.

3.1 General radar theory

Radio Detection And Ranging, shortened to radar, is a remote sensing technique that uses electromagnetic waves to determine characteristics of an object such as its position, size and line-of-sight velocity. In its simplest version, a radar is an antenna that sends electromagnetic pulses and listens for echoes. This echo consists of a part of the original pulse that has been scattered by a target in the radars field of view. If an echo is received, the range R to the target producing it is given by

$$R = \frac{1}{2}ct \tag{3.1}$$

where c is the speed of light and t is the time it takes for the signal to travel to the target and back. The time allocated to listening for an echo must increase proportionally to the distance to the target, otherwise the echo will be received after the next pulse has been transmitted, and range aliasing will occur. Given the time between the transmission of the pulses, denoted by τ, the maximum range detectable without range aliasing R_{max} is

$$R_{max} = \frac{1}{2}c\tau \tag{3.2}$$

Another important parameter is the time length of each individual pulse, τ_p. The pulse length determines the range resolution ΔR of the radar given by equation 3.1 with $t = \tau_p$

$$\Delta R = \frac{1}{2} c \tau_p \tag{3.3}$$

Any velocity that the target has towards or away from the radar will Doppler-shift the echo. The line-of-sight velocity v, assuming non-relativistic speeds, can be calculated from the Doppler frequency shift Δf according to the relationship $\Delta f = 2vf_0/c$ where f_0 is the frequency of the transmitted pulse. The frequency shift is positive when the target moves towards the radar and negative when it moves away. However, using this method becomes problematic when using short pulses to measure velocities in the order of magnitude seen in the ionosphere. A typical F-region velocity of $400\,\mathrm{m\,s^{-1}}$ with a transmitted frequency of $15\,\mathrm{MHz}$ (typical in coherent scatter radars) produces a Doppler shift of $40\,\mathrm{Hz}$. Given that the standard pulse length τ_p of SuperDARN is $300\,\mu\mathrm{m}$, one pulse will only contain about 1% of the complete wave cycle, which makes it hard to measure accurately. Incoherent scatter radars use even shorter pulse lengths and higher frequencies, and so they suffer the same complication.

Another method to calculate the line-of-sight velocity that gets around the accuracy problem is to measure the phase shift between pairs of consecutive pulses separated by time τ. The phase shift between pulses $\Delta\phi$ is derived by simple geometry to be

$$\frac{\Delta\phi}{2\pi} = \frac{2\tau v f_0}{c} \tag{3.4}$$

which can be solved for v giving

$$v = \frac{c}{4\pi\tau f_0}\Delta\phi \tag{3.5}$$

If $\Delta\phi \geq \pi$, velocity aliasing will occur. To increase the velocity that the system can unambiguously measure, we must either decrease the transmitted frequency f_0 or decrease the time between pulses τ. The transmitted frequency must be chosen in accordance to the scales of interest in the plasma. This leaves a decrease in τ as the only way to increase the range of velocities that can be measured. However, if an echo produced by the first pulse at $t = 0$ has not returned to the receiver after $t = \tau$ when the second pulse is sent, it will lead to range aliasing. Equation 3.2 shows that a decrease in τ leads to a decrease in the maximum range that can be measured. To summarize, there are two conflicting requirements: decreasing the time between pulses makes it possible to detect larger velocities, but at the expense of the maximum range detected. The solution is to use a sequence of pulses separated by different multiples of the elementary pulse length τ_D, which is then repeated. This is called a multi-pulse technique and is used in SuperDARN and some incoherent scatter radars (like the one used in this thesis).

3.2 Coherent scatter radar

The Super Dual Auroral Radar Network (SuperDARN) is a global network of 35 high-frequency (HF) radars in the high and mid latitudes monitoring conditions in the F-region of the ionosphere. The transmitted frequency in SuperDARN radars is chosen so that they are sensitive to the decameter-scale magnetic field aligned density irregularities present in the E and F-regions. These irregularities move with the background E×B-drift and SuperDARN radars can therefore measure the horizontal ionospheric drift velocities. Refraction in the ionosphere bends the path of the transmitted radar pulse as shown in figure 3.2. For coherent scatter to occur, we need constructive interference which happens when the Bragg scatter condition is satisfied:

$$2d \sin\theta = n\lambda_r \tag{3.6}$$

Here, λ_r is the radar wavelength, n is an integer and as seen in figure 3.1, θ is the angle between the density irregularities (and thus the magnetic field lines) and the transmitted or reflected pulse and d is the distance between the irregularities. Satisfying the Bragg scatter condition, however, is not enough to get backscatter. The pulse is only backscattered when $\theta = 90°$, since it must travel the same path back to the radar to be detected (here we assume that the transmitter is co-located with the receiver). In this case equation 3.6 reduces to

$$2d = n\lambda_r \tag{3.7}$$

Since SuperDARN radars work at a typical frequency of $15\,\mathrm{MHz}$, which is equivalent to $\lambda_r = 20\,\mathrm{m}$, they are only sensitive to scale sizes of $\sim 10\,\mathrm{m}$ (setting $n = 1$).

SuperDARN radars do not always detect ionospheric backscatter. The pulse might be lost to space or it might scatter with $\theta \neq 90°$ so that the radar does not receive the pulse. Backscatter from the ground, so-called *ground scatter* shown in figure 3.2, is also common and can sometimes be confused with ionospheric scatter.

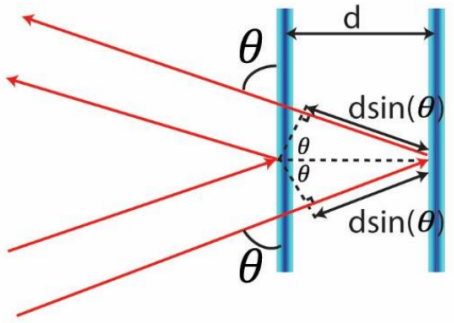

Figure 3.1: Geometry of Bragg scattering of an incoming EM wave by two structures separated by distance d. Figure taken from Baddeley (2019).

As mentioned in section 3.1, SuperDARN radars use the multi-pulse technique to determine the primary data products from the backscattered signal. The typical sequence

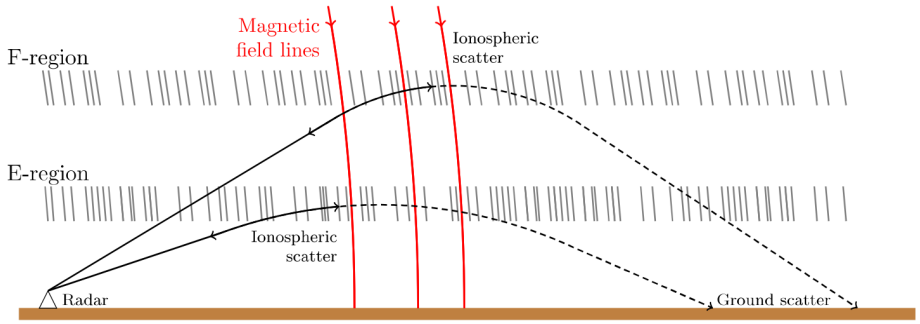

Figure 3.2: Schematic diagram showing the refraction of HF waves in the high latitude ionosphere. Figure taken from Bland (2016).

that SuperDARN uses consists of either 7 or 8 pulses of pulse length $\tau_p = 300\,\mu s$ sent at different multiples of time lag τ, where $\tau = n\tau_p$. Typically in SuperDARN radars, $n = 5$ or 8 making $\tau = 1.5\,\text{ms}$ or $2.4\,\text{ms}$. The maximum time between two consecutive pulses is 14τ, which using equation 3.2 is shown to make it possible to detect ranges of up to $0.5 \cdot 14\tau c = 3150\,\text{km}$. The shortest time between two of the pulses is 1τ, which given equation 3.5 with $\Delta\phi = \pi$ and a carrier frequency f_0 of between $8\,\text{MHz}$ to $20\,\text{MHz}$ (SuperDARN radars can operate in this frequency range) sets the maximum detectable line-of-sight velocity to $2500\,\text{m}\,\text{s}^{-1}$ to $6250\,\text{m}\,\text{s}^{-1}$.

To determine the primary data products, the autocorrelation functions (ACFs) for all possible pairs of pulses in the muti-pulse sequence are evaluated. The ACFs are determined separately for every range gate in a beam. A typical SuperDARN radar has 16 look directions, called beams, each divided into 75 range gates $45\,\text{km}$ long ($\Delta R = 0.5\tau_p c = 45\,\text{km}$)

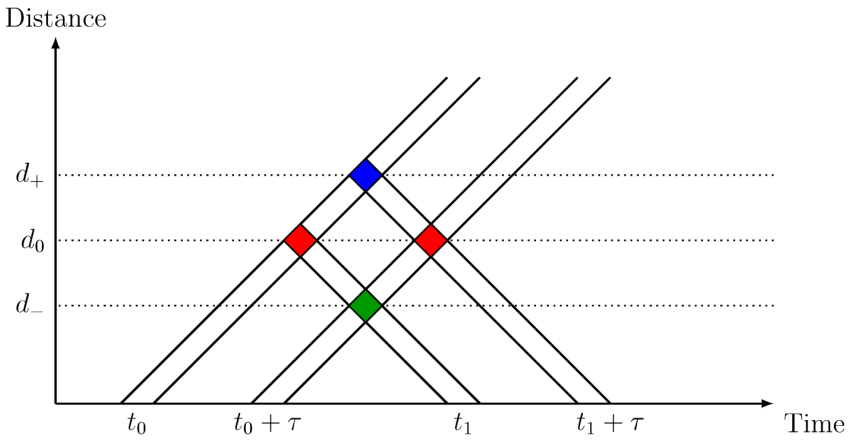

Figure 3.3: Range-time diagram for a two pulse sequence. Figure taken from Bland (2016).

As a simplified example, figure 3.3 shows a range-time diagram of a pair of pulses sent at time t_0 and $t_0 + \tau$. The signals scattered at range d_0 and d_- return simultaneously at time t_1, while the backscatter from range d_0 and d_+ returns at time $t_1 + \tau$. The ACF from this pair of pulses is calculated as follows

$$\begin{aligned} A(t_1) \cdot A(t_1 + \tau) &= [A_1(d_0) + A_2(d_-)] \cdot [A_1(d_+) + A_2(d_0)] \\ &= A_1(d_0)A_2(d_0) + A_1(d_0)A_1(d_+) \\ &\quad + A_2(d_-)A_1(d_+) + A_2(d_-)A_2(d_0) \end{aligned} \tag{3.8}$$

where A_1 and A_2 are the amplitudes of the signals measured at times t_1 and $t_1 + \tau$ respectively. Signals returning from different non-overlapping ranges are not correlated, and therefore only the first term of the expansion will contribute when the ACFs of several pulse sequences are averaged. This principle, scaled up to contain a sequence of pulses at different time lags, chosen so that individual ranges can be resolved, is the principle behind SuperDARN radars.

Averaging is done to remove the noise from the uncorrelated signal. This works under the assumption that only the ionosphere at range d_0 is correlated and that the noise is random and therefore averages out given enough samples. This averaging time, called integration time, is typically 3-7 seconds. The averaged ACF for time lag $k\tau$, where k is an integer which denotes the lag, is a value given by

$$R(\tau) = \langle A(t_1) \cdot A(t_1 + k\tau) \rangle \sim P_k e^{i\phi_k} \tag{3.9}$$

where P_k is the power of the ACF at time lag $k\tau$ and

$$\phi_k = k\tau \langle \omega_D \rangle \tag{3.10}$$

is the phase of the ACF at time lag $k\tau$, with ω_D denoting the Doppler frequency shift. The Doppler line-of-sight velocity v_D can be calculated by inserting equation 3.10 into 3.5 giving

$$\langle v_D \rangle = \frac{c}{4\pi\tau f_0} \Delta\phi_k = \frac{c\langle \omega_D \rangle}{4\pi f_0} \tag{3.11}$$

Figure 3.4 shows a typical averaged ACF function $R(\tau)$ of a SuperDARN radar where τ is the ACF lag. The power of the averaged ACF function $|R(\tau)|$ is fitted with either an exponential or a Gaussian function. When using an exponential decay fit, as done in this thesis, the characteristic decay time τ_c is obtained from

$$|R(\tau)| = |P_k| = R_0 e^{-\tau/\tau_c} \tag{3.12}$$

where R_0 is the power of the ACF at $\tau = 0$ (called the zero-lag power) and τ_c is the time lag at which the power of the best fit decays by $1/e$. The spectral width SW is then given by

$$SW = \frac{2c}{4\pi f_0 \tau_c} \tag{3.13}$$

where c is the speed of light and f_0 is the transmitted frequency. The spectral width calculated from the characteristic decay time of the exponential fitting is called the Lorentzian

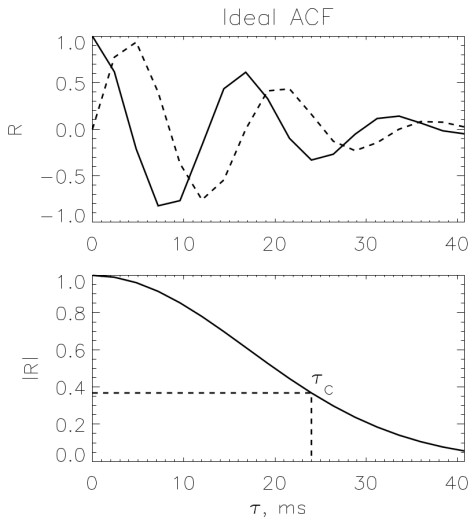

Figure 3.4: The upper graph shows a normalized ideal ACF from a SuperDARN radar, with the real and imaginary parts represented by the solid and dashed lines respectively. The lower graph shows the magnitude of the same ACF with the characteristic decay time τ_c. Figure taken from Ponomarenko and Waters (2006).

spectral width, while using the Gaussian fitting to find the characteristic time results in the Gaussian spectral width. The somewhat confusing nomenclatures come from using a frequency domain point of view: the Fourier transform of an exponential function is Lorentzian, while a Gaussian function has another Gaussian function as its Fourier transform. In this thesis, the Lorentzian spectral width is used.

A typical SuperDARN radar consists of a phased 1-D array made up of 16 dipole antennas with transmission and receiving capabilities. Some SuperDARN radars, like the Hankasalmi radar used in this thesis (shown in figure 3.5), are fitted with an auxiliary 1-D array of 4 receiving dipole antennas used to determine the elevation of the backscattered signal. Each radar has a field of view of $\sim 52^\circ$ in azimuth, with the furthest echoes received from a bit over $3000\,\mathrm{km}$ under optimal ionospheric conditions. Most SuperDARN radars provide data in real time. The primary data products are the signal-to-noise ratio, also known as the power, the line-of-sight Doppler velocity and the Doppler spectral width as defined in equations 3.11, 3.12 and 3.13 respectively. These parameters are usually displayed in two types of plots: time series of the velocity (or another primary data product) at all range gates along one beam, called range-time plots, or plots showing the velocities (or another primary data product) at all range gates along all beams for one time, called fan plots. This will be described in more detail in section 5.3. Combined data from all SuperDARN radars are also used, along with a model, to calculate the convection pattern in the F-region created by the Dungey cycle.

Figure 3.5: The SuperDARN radar in Hankasalmi, Finland. Picture from private correspondence.

3.3 Incoherent scatter radar

Incoherent scatter radars (ISR) use frequencies in the VHF or UHF (Very High or Ultra High Frequency) frequency band. The incoherent scatter radar technique has, since its introduction in the early 1960's, proven to give a wealth of detailed information about the ionosphere. Unlike other types of radars, such as coherent scatter radars, ISR can determine plasma parameters such as temperatures and electron densities. ISRs also have better spatial resolution (down to 5-10 km along the beam), but this comes at the cost of spatial coverage that other radars such as SuperDARN radars benefit of. Cost is also an issue, since due to the scattering ISR relies on, only a very small portion of the energy transmitted is backscattered by the plasma and these radars must emit large amounts of power and have large antennas to produce a satisfactory signal-to-noise ratio. The EISCAT Svalbard Radar (ESR) used in this thesis, as an example, sends $\sim 10^{6}$ W and receives only $\sim 10^{-14}$ W with a fixed transmission frequency of $500\,\mathrm{MHz}$. While SuperDARN radars are always turned on, the ESR is only active for about 1000 hours per year.

In the case of incoherent scatter radars, the scattering of the transmitted wave is caused by fluctuations in electron density due to two kinds of inherent wave modes in the ionosphere: ion acoustic waves and electron plasma waves (described in section 2.1.3 and 2.1.4 respectively). Individual electrons scatter the electromagnetic radiation emitted by the radar through a process called Thomson scattering, but these electrons themselves are controlled by the much slower and massive ions. If the Debye length is much smaller than the radar wavelength ($k^2\lambda_D^2 \ll 1$), which allows for the collective behaviour of the plasma to be observed, the observed ion acoustic waves and electron plasma waves will up- and down-shift the backscattered signal according to their phase speed. The backscatter

then contains information about these two wavemodes, which allows us to retrieve several ionospheric parameters.

The signal processing involved in retrieving these ionospheric parameters starts, as is the case for the data analysis in SuperDARN, by obtaining the averaged ACF of the received signal. The ACF can be fourier transformed into the power density spectra (PDS) which is shown in figure 3.6 in its idealized version. The theory behind the PDS is well known, and its shape can be theoretically determined given the plasma parameters and the radar wave vector k. Given this knowledge, the PDS can be fitted using an iterative fitting method to find the plasma parameters that best describe a plasma with the measured PDS (in the software, the ACF is fitted instead of the PDS since it is more computationally effective, but mathematically this is equivalent).

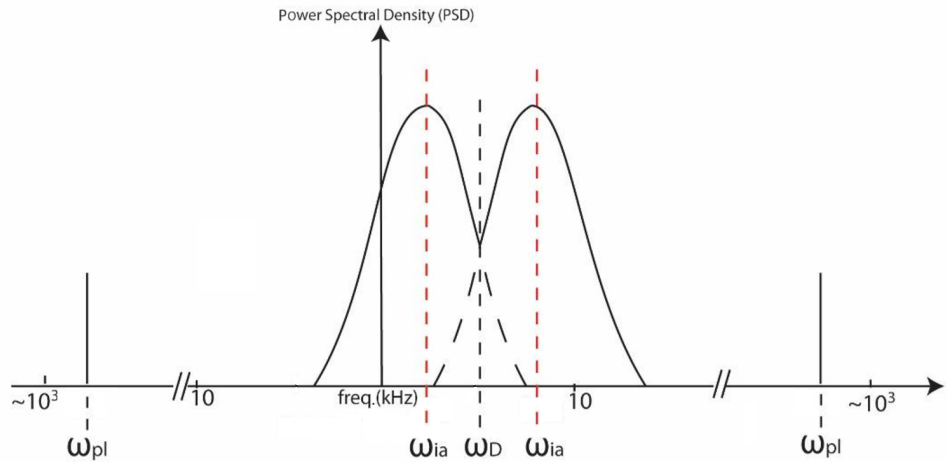

Figure 3.6: An example of a PDS for an incoherent scatter radar. Picture modified from Baddeley (2019).

The PDS is composed of two lines, the ion line in the KHz and the plasma line in the MHz. The fact that the spectrum is symmetric reflects the fact that the wave modes the radar detects propagate both towards and away from the radar line of sight.

The ion line consists of two peaks with tops at the ion acoustic frequency ω_{ia} given in equation 2.4 with $k_{ia} = k$

$$\omega_{ia} \approx kC_s = k\sqrt{\frac{k_B T_e + 3k_B T_i}{m_i}} \tag{3.14}$$

where $k = 2\pi f_0/c$ is the wavenumber of the transmitted pulse. As noted in section 2.1.4, to derive equation 2.4 we assume that the wavenumber of the transmitted pulse is much larger than the Debye length. With frequencies in the VHF or UHF band this is satisfied. This is also equivalent to saying that there the Landau damping is weak. Landau damping is the collisionless damping of a plasma wave that occurs due to waves in the plasma los-

ing energy to particles with slightly lower thermal velocity than the wave's phase velocity. Having weak Landau damping happens when $T_e \gg T_i$. Without Landau damping the peaks in the PDS would be close to delta functions, but the damping broadens the peaks and causes the two ion line peaks to merge. If the ion velocity in the plasma is not zero, the ion line will be Doppler shifted such that the midpoint is $\Delta\omega_D$ away from the transmitted frequency. The line-of-sight ion drift velocity is then given by $v_D = \Delta\omega_D/k$. The width of the ion line is proportional to $(T_e + T_i)/m_i$ and the depth of the valley between the peaks is proportional to T_e/T_i and reflects the amount of Landau damping. Thus, given the ion composition (which can be estimated from models), the electron and the ion temperatures can be determined. Last but not least, the electron density is proportional to the integral of the ion line. Thus from the ion line we can get four primary data products: the ion and electron temperatures, the ion line of sight velocity and the electron density. These data products can be combined with models to estimate many other parameters, amongst them the ionospheric conductivities. The Hall and Pedersen conductivities are calculated as described in section 2.4.2, with the electron density and the ion and electron temperatures taken from the primary data products while the neutral temperature and the neutral densities are taken from the Mass-Spectrometer-Incoherent-Scatter (MSIS) model.

The plasma line also has two peaks at the Langmuir frequency given in equation 2.3 with $k_{pl} = k$ and using the now familiar approximation $k^2\lambda_D^2 \ll 1$

$$\omega_{pl} = \omega_{pe}(1 + 3k^2\lambda_D^2) \approx \omega_{pe} \tag{3.15}$$

Since the plasma oscillation frequency ω_{pe} is proportional to the square root of the electron number density n_e, by measuring the frequency of the plasma line we can obtain a somehow independent measurement of n_e that can be compared with the one obtained from the ion line. However, all four primary data products of ISR radars (including n_e) are derived from the ion line.

The ESR consists of two parabolic antennas. The biggest one, with a diameter of 42m, is fixed roughly parallel to the direction of the magnetic field, while the 32m antenna is steerable. The 32m can also produce scans, but it can only move at $\sim 1^\circ$ per second and requires high densities in the ionosphere in order to achieve an acceptable signal-to-noise ratio while scanning. Figure 3.7 shows the two parabolic antennas and the building containing the electronics and the control station.

Summary plots showing altitude-time graphs for the four primary data products of all EISCAT experiments are available online. Figure 3.8 shows the summary plot of the data taken by the 42m dish of the ESR where the signature of the nightside aurora can be clearly seen from ∼18:50UT-19:10UT and from ∼19:45UT-20:05UT. The most obvious auroral signature in the data is the increased electron densities in the E- and F-region and the increased electron temperatures in the F-region. Figure 3.9 shows an example of cusp aurora appearing in the 42m dish field of view from ∼9:40UT and onwards, with the electron densities and temperatures both increasing in the F-region.

Figure 3.7: Picture of the EISCAT Svalbard Radar, with the 32m dish pointing towards the south on the left and the field-aligned 42m dish on the right. Figure courtesy of EISCAT.

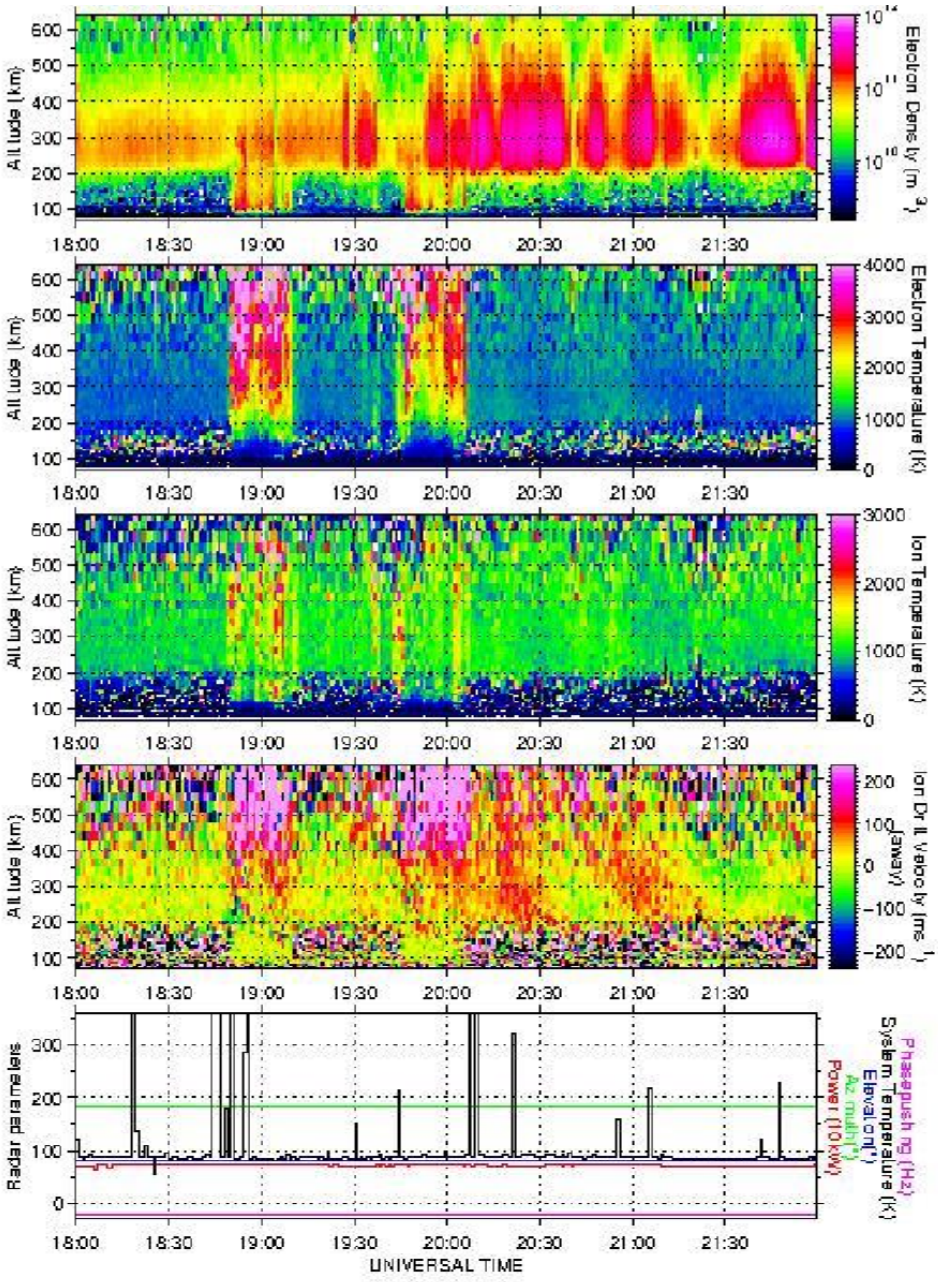

Figure 3.8: Summary plot of data taken by the 42m dish of the ESR. Nightside aurora can be seen in the field of view of the radar from 18:50UT-19:10UT and from 19:45UT-20:05UT.

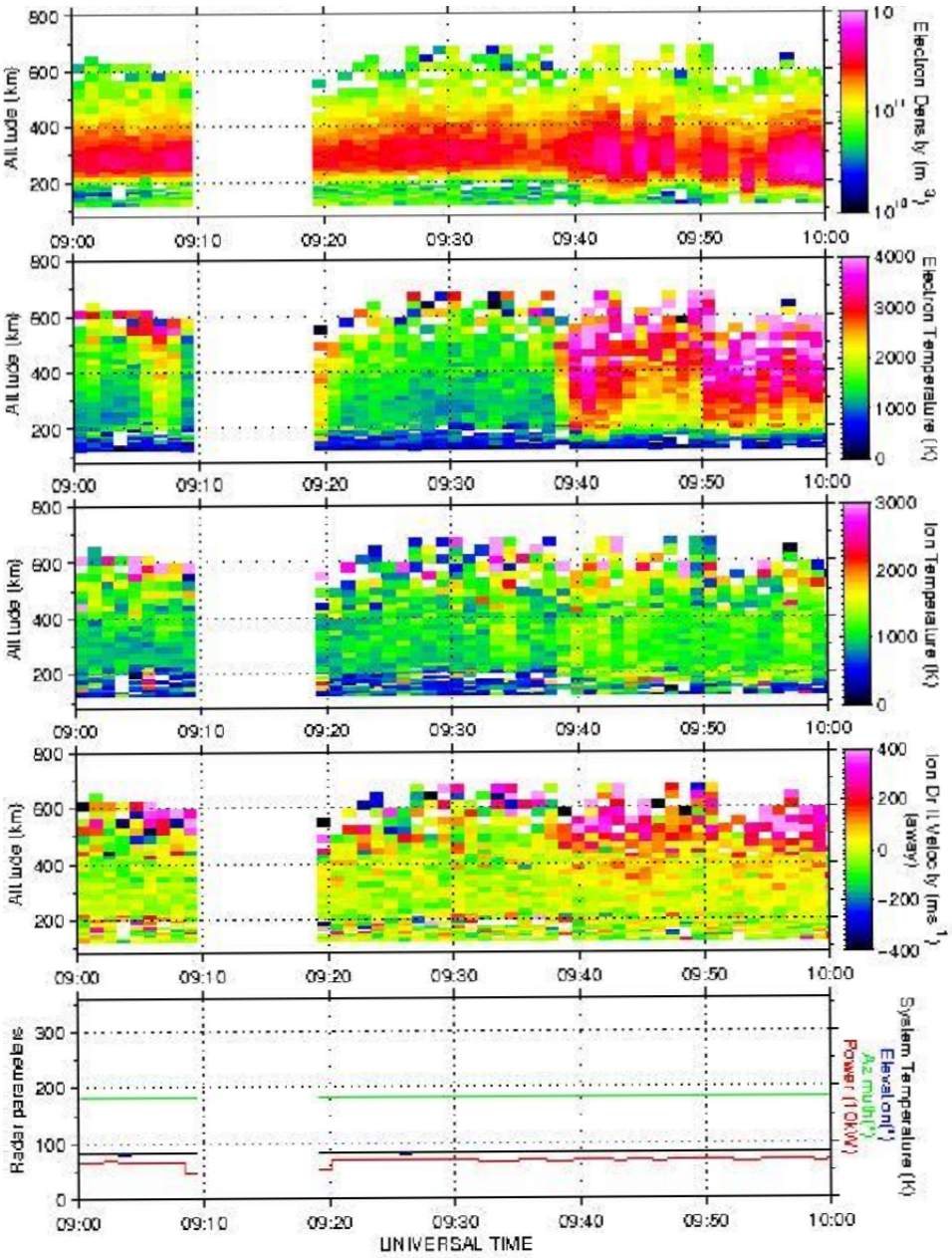

Figure 3.9: Summary plot of data taken by the 42m dish of the ESR. Cusp aurora can be seen in the field of view of the radar from 9:40UT and until the end of the experiment at 10:00UT.

3.4 Meridian scanning photometer

A Meridian Scanning Photometer (MSP) is an instrument used to study the motion of the aurora along the magnetic meridian. The MSP used in this thesis is located at the Kjell Henriksen Observatory (KHO) in Svalbard and has up to 5 channels. The channels measuring the $4278\,\text{Å}$, $5577\,\text{Å}$ and $6300\,\text{Å}$ emission lines have been in operation since the instrument was installed, while the other two channels have varied through the years. Each channel consists of a narrow bandpass filter with a bandpass of approximately $4\,\text{Å}$ mounted in front of a cooled photomultiplier and placed in front of a rotating mirror that scans the sky from north to south along the magnetic meridian (see figure 3.10 for an illustration). Each meridian scan takes $16\,\text{s}$ and has a 1° angular spatial resolution. The MSP is continuously in operation when the sun is more than 12° below the horizon. The data products are intensity as a function of elevation angles in the meridian plane for each channel. It is usually presented as a keogram with the intensity given in Rayleighs (R). This will be described in more detail in section 5.3.

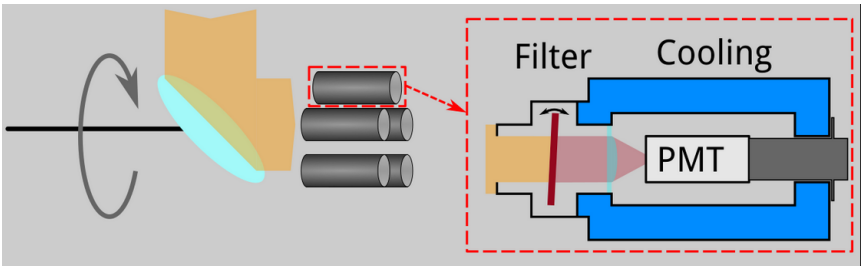

Figure 3.10: Illustration of the working components of the MSP at KHO. From private correspondence.

Chapter 4

Spectral Widths

This chapter is a summary of the aspects surrounding the spectral width parameter that are of importance in this thesis. While this would normally belong to the theory chapter, it is placed here because it is important to understand what the spectral width parameter is, something that is explained in the previous chapter on instrumentation. The geographic distribution of spectral widths is examined before doing a brief literature review on the possible causes of enhanced spectral widths.

4.1 Geographic distribution of spectral widths

Mathematically, the spectral width is proportional to the width of the velocity spectra measured by SuperDARN. High SWs are measured in two situations: when the velocity spectrum consists of a single, broad peak (called a single-component spectrum) and when it consists of several peaks (called a multi-component spectrum). A broad peak means the velocity measured (in a simple spectra, the velocity at the peak of the distribution) has an associated large SW. Although the individual components of a multi-component distribution might be narrow, the SuperDARN fitting algorithm works by assuming a single velocity in each range gate, and thus, such a spectrum will be interpreted as a mean velocity with a high SW. André et al. (2002) present a statistical analysis showing that single-component broad spectra are mostly seen in the night and morning sectors, while multi-component spectra are rare in the nightside, but common elsewhere above $\sim 75^{\circ}$ MLAT (including the cusp).

Baker et al. (1995) found that the distribution of SWs in the cusp can generally be described as Gaussian with a peak at about 220m/s, with the majority of the spectra found between $\sim 120\,\mathrm{km}$ to $320\,\mathrm{km}$, while the distribution in the LLBL is often described as an exponential distribution with a peak at 50m/s. While the authors also found a few cases of SW distributions in the LLBL that exhibit characteristics identical to cusp distributions,

the general pattern is clear: high SWs are associated with the cusp. Statistical studies, such as the one in Villain et al. (2002), have corroborated this correlation, and found that the SWs in the nightside sector also follow a similar pattern. The authors show that, statistically speaking, SWs become high (exceed $200\,\mathrm{m\,s^{-1}}$) at around 70°MLAT in the nightside, which is roughly the latitude at which the polarward boundary of the auroral oval is located. The latitude at which the SWs become high varies in MLT, but the SWs polarward of that latitude are recurrently high (before decreasing again at even higher latitudes). This can be seen in figure 4.1, which shows the distribution of the average SWs measured by all SuperDARN radars in the winter of 1996-1997.

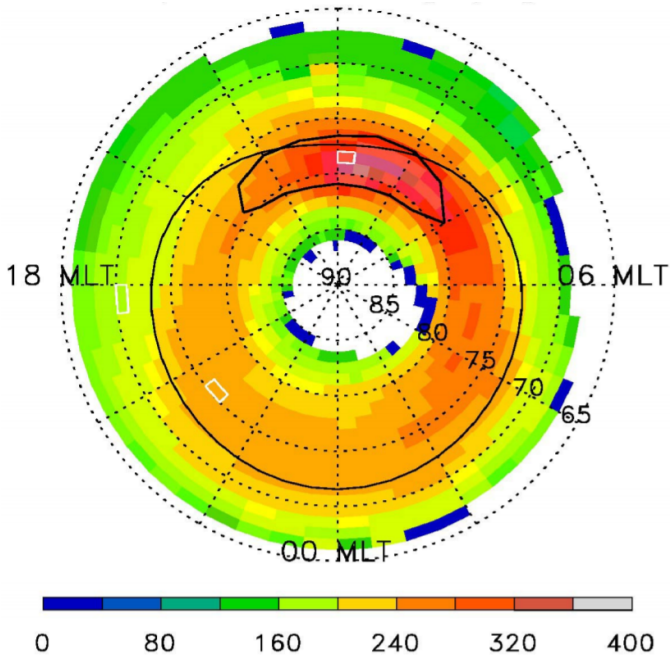

Figure 4.1: Average spectral widths measured by SuperDARN radars in the winter of 1996-1997. The large circle shows the poleward limit of the auroral oval for moderate activity, while the small one shows the LLBL/cusp/mantle contour. Figure taken from Villain et al. (2002).

The transition between low and high spectral widths, often referred to as the spectral width boundary (SWB), is not as sharp as the name implies. Indeed, it can occur over many SuperDARN range gates, meaning hundreds of kilometers (Chisham and Freeman 2004). Determining the boundary with an algorithm is not trivial and a number of studies use a subjective visual approach instead. Chisham and Freeman (2003) show that naive algorithms that involve looking for the first range gate (in the polarward direction) that has a SW above a chosen threshold, although widely used, are inaccurate. The authors show that because the SW distributions poleward and equatorward of the OCB have significant overlap, a more complicated algorithm involving filtering the data in time and space before applying the threshold algorithm is needed. This algorithm, called the 'C-F threshold

technique', is described in Chisham and Freeman (2004).

There have been several studies looking into whether the spectral width boundary can be used as a proxy for the OCB. Statistical studies by Chisham et al. (2004), Chisham et al. (2005a) and Chisham et al. (2005b) show that the SWB represents a good proxy for the OCB in parts of the dayside sector ($\sim$08-12 MLT) and the nightside sector ($\sim$00-02 MLT), but not in the morning sector ($\sim$02-08 MLT) where the OCB tends to be located polarward of the spectral width boundary. Case studies are not as unambiguous: Lester et al. (2001) shows that the SWB can sometimes (but not always) be used as a proxy for the OCB in the pre-midnight sector. Specifically, they show that the relationship between the SWB and the OCB breaks down during a substorm. Another example of breakdowns in the SWB-OCB relationship is demonstrated by Woodfield et al. (2002), who shows an example of a two hour period in the post-midnight sector where the OCB is significantly polarward of the SWB.

4.2 Causes of high spectral widths

It is generally accepted that high spectral widths are not caused by instrumental effects (e.g. Huber and Sofko 2000), and thus, a physical cause must be present. Physically, the spectral width parameter measured by the SuperDARN radars is a measure of the spatial and temporal structure in the scattering targets on scales of the order of, or less than, the integration period of the radar and the spatial area of the range gate. The physical mechanisms affecting this structuring are not fully understood, but several mechanisms have been proposed:

1. Intense soft electron precipitation ($\sim$100 eV) has been shown to be structured, specially in the cusp, and is associated with high SWs (Baker et al. 1995, Moen et al. 2000). Moen et al. (2000) proposed that large SWs are caused by re-structuring of the ionospheric plasma at scale lengths detected by SuperDARN ($\sim$10 m). Ponomarenko et al. (2007) argue that the spectral broadening at high latitudes (including the cusp) seems to be caused by the lifetime of the scattering targets being smaller than the integration time of the radar, and suggest that this might be caused by soft electron precipitation that shows high temporal variability in these timescales. Chisham et al. (2005a) reported a inverse relationship between the energy flux of the precipitating electrons and the SWs measured. High flux particle precipitation is known to enhance the height integrated Pedersen conductivity and thus suppress the strength of the ionospheric electric fields, which can overpower the small-scale ionospheric electric field structuring and thus suppress high SWs (Parkinson et al. 2004, Ponomarenko and Waters 2006)

2. Turbulence within the large-scale convection pattern caused by Kelvin-Helmholtz instabilities (see 2.4) can map down from the LLBL/magnetopause region to the ionosphere giving rise to velocity shears and vortices of down to a few kilometers width. Since the plasma flow is turbulent in scales similar or smaller to the Super-

DARN range gate, this will enhance SWs. (e.g. Huber and Sofko 2000, Schiffler et al. 1997)

3. Structured field aligned currents caused by the structured precipitation can also cause vortices leading to enhanced SWs. Such a current can have a negative inner core and a positive outer core given by the charge exchange between the precipitating ions and the neutrals. if this is the case, the resulting radial electric field will produce a vortice around the filament. Such vortices would be smaller than SuperDARN range gate and could thus enhance SWs. (Huber and Sofko, 2000)

4. A type of ultra low frequency (ULF) waves (in the frequency band denoted Pc1/2 band) commonly present in the cusp and in the auroral oval could modulate the movement of the electric field (and thus the associated irregularities) and produce increased spectral widths. However, the simulation that André et al. (2000) used to quantify the impact of the waves on the SWs was shown by Ponomarenko and Waters (2003) to contain an error. In the same paper, the authors revised the model and found the impact of ULF waves to the SWs to be small, concluding that these waves cannot be the main mechanism producing large spectral widths.

5. The geometry of the radar with respect to the convection patters caused by the Dungey cycle (see section 2.3.1) can theoretically influence SW measurements. Ionospheric convection results in areas with large velocity gradients. If these velocity gradients are in the field of view of the radar, and the geometry is such that the radar (that measures only the line-of-sight velocity) is able to detect them, the velocity spectra will have multiple components leading to increased SWs. Large velocity gradients are more likely to be found in the proximity of the OCB (e.g. Sotirelis et al. 2005) and could thus contribute to the higher spectral widths seen polarward this boundary. However, this has mechanism has been shown to have only a small effect in SW measurements (André et al., 2000). The importance of the large-scale convection pattern is further reduced for polar-looking radars, since it is only when the velocity gradient has a component orthogonal to the field of view of the radar that it affects the spectral width recorded.

Chapter 5

Experimental methodology

In this thesis, data from the EISCAT Svalbard Radar and the SuperDARN radar at Hankasalmi, Finland as well as the MSP at the Kjell Hensiksen Observaroty in Svalbard are used. This section discusses the acquisition and processing of data from these three instruments.

5.1 Obtaining the data

All EISCAT data, as well as data from some other instruments used in upper atmospheric science, can be freely accessed from the Madrigal database [1]. The data can be downloaded directly from their website. However, since data for over 200 days was needed, this was not practical. To automate the process the remote Madrigal API [2] developed by the MIT Haystack Observatory was used instead. The downloaded analysed data included the four primary data products (electron and ion temperature, electron density and ion velocity) as well as the Hall and Pedersen conductivities, which are derived as explained in section 2.4.2 and 3.3. The routine that does the fitting to retrieve these parameters is called GUISDAP (Grand Unified Incoherent Scatter Design and Analysis Package). The standard integration time of 1 minute was used.

The SuperDARN database is not accessible online. Instead, the data were obtained through the UNIS SuperDARN computers, which have remote access permission to a SuperDARN data mirror at the British Antarctic Survey (BAS). The raw data files (.raw files) for the dates of interest were downloaded and analysed using the Radar Software Toolkit (RST) [3], an open source package specifically made to analyze and visualize SuperDARN data. This produces files in the fitacf format that were read in with the Python library

[1] http://cedar.openmadrigal.org
[2] http://cedar.openmadrigal.org/madrigaldownload
[3] https://github.com/SuperDARN/rst

DaViT-py [4] (now deprecated with the release of PyDARN [5]). These files contain all the data and metadata produced by the radar, including the spectral widths. The integration time for each beam is $\sim 4\,\mathrm{s}$, and a full scan contains 16 beams and thus takes $\sim 1\,\mathrm{min}$ to complete in the standard scan mode.

The MSP data from KHO, referred to simply as MSP from here on, are stored locally. The data are available as text files with the intensities of all the emission wavelengths at each angle for each scan. One scan lasts 16s.

Due to the variable data formats, processing languages and data sources the time taken to get the data into coherent, readily accessible formats was considerable. Dealing with SuperDARN data was specially challenging as DaViT-py stopped being supported a few years ago, and as such there was significant debugging needed. The replacement library PyDARN was not released at the time.

5.2 Forming an event list

The starting point for this thesis was a list compiled by X.C. Chen and co-workers that detected 276 events between 1997 and 2014 where the MSP was turned on and its field of view was mostly cloud-free while ionospheric backscatter (measured by the Hankasalmi radar) was observed over latitudes comparable to those covered by the field of view of the MSP. This list was the starting point for the Chen et al. (2016) paper where the authors compared the spectral width boundary as measured by the Hankasalmi radar to the 6300Å boundary as measured by the MSP.

For this thesis, co-located data from the ESR as well as the MSP and the Hankasalmi radar are needed. While the Hankasalmi radar is always operative, the ESR is only turned on occasionally. Other factors, described below, further narrowed down the event list to the final list of 10 events used in this thesis. The process of obtaining the final event list from the original list of 276 events was mostly automated, although a manual inspection was preformed towards the end of the process. The steps are described below.

Step 1: Finding overlapping measurements

The first step was to find the events that had overlapping data from the Hankasalmi radar and the ESR. In order for the data to be considered overlapping, they must satisfy both of these requirements:

1. The measurements must be simultaneous.

   Because the integration time of the ESR is longer than that of the Hankasalmi radar, the measurements were defined as simultaneous if the Hankasalmi radar measurement was within the $1\,\mathrm{min}$ integration time of the ESR measurement.

[4] https://github.com/vtsuperdarn/davitpy
[5] https://github.com/SuperDARN/pydarn

2. The measurements must be co-located.

   First of all, the measurements must be taken at approximately the same height. For EISCAT radars, the altitude of the midpoint of each range gate is given in the analysed data files. SuperDARN radars use a virtual height model which assumes (at the range gates under study here) an F-region altitude of 350km for the irregularities (Chisham et al.). This is not a big issue since this study is focused on the F-region, where the plasma parameters over large altitude ranges vary very little (due to the large scale height). In this thesis, ESR measurements within an altitude range of $250\,\mathrm{km}$ to $350\,\mathrm{km}$ are said to match the altitude of the Hankasalmi radar measurements.

   Secondly, the horizontal position must also match. In order to define this, it is necessary to first discuss how the positions for the measurements from each of the radars are found:

   - For an ESR range gate, the geographic coordinates of the midpoint of the range gate given its position in local coordinates (that is, the elevation, azimuth and range) were calculated. This was done by using a function of a third-party script called EiscatScanPlot [6]. The local coordinates of the midpoint of each range gate, for a given integration time, are give in the analysed data files. The geographic coordinates were then converted to Altitude Adjusted Corrected Geomagnetic (AACGM) coordinates by using the AACGMv2 package [7] and setting the altitude to the altitude of the range gate, which is also given in the analysed data file. AACGM coordinates provide an accurate representation of the actual magnetic field by giving points along a given magnetic field line the same coordinates and thus, as the name suggests, take into account the altitude of the observations. They were developed by Baker and Wing (1989). The AACGMv2 package is an implementation of the work published by Shepherd (2014). AACGM latitudes are referred to as MLAT from here on for simplicity.
   - For a Hankasalmi radar range gate, DavitPy was used to find the geographic coordinates of the corners of said range gate. Again, the AACGMv2 package was used to convert those to magnetic coordinates using an altitude of 300km.

   Once this is done, defining a horizontal overlap is easy: the ESR range gate coordinate must be inside the trapezoid created by the corners of the Hankasalmi radar range gate in order for them to be considered co-located. This was checked by using a Python library called Shapely [8].

Step 2: Removing unusable data

A significant portion of overlapping measurements contained unusable data and had to be removed. Here, an overlapping measurement refers to the measurements from one ESR

[6] https://github.com/cmeeren/eiscatscanplot
[7] https://github.com/aburrell/aacgmv2
[8] https://github.com/Toblerity/Shapely

range and the simultaneous measurements from the co-located Hankasalmi range gate. The overlapping measurements were removed if they included data that satisfied at least one of the following:

1. The backscatter from the Hankasalmi radar was classified by the fitting algorithm as ground scatter. This classification is done using the algorithm presented in Blanchard et al. (2009) that relies on narrow spectral widths and low Doppler velocities as criteria.

2. At least one of the following data products was either infinite, ≤ 0 or otherwise not a number: electron and ion temperature and electron density from the ESR and spectral width from the Hankasalmi radar. These values are obviously not physical and are due to bad fittings.

Step 3: Averaging the data

The Hankasalmi radar has range gates that cover a larger geographical area than the ESR range gates. On the other hand, the integration periods are longer for ESR than for the Hankasalmi radar. This means that the overlapping measurements had to be averaged in both time and space.

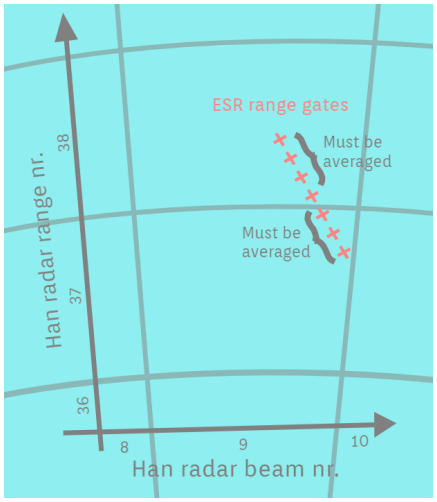

Figure 5.1: Illustration of a typical geometry of the Hankasalmi (Han) radar range gates with ESR range gates at altitudes between 250 km to 350 km superposed.

Figure 5.1 shows a typical scenario that requires averaging in space since several ESR range gates overlap with a single Hankasalmi radar range gate. In cases like this the ESR data (electron and ion temperature and electron density) from the range gates inside any one Hankasalmi radar range gate had to be averaged, as showed in the figure.

In some cases, averaging in time was also needed. This was typically the case when the Hankasalmi radar had been running a special program with a scanning pattern that has made it so the beams with the overlapping range gates were sampled with a frequency $>1\,\mathrm{min}$. When this was the case, the spectral width measurements taken over the $>1\,\mathrm{min}$ integration time of ESR were averaged.

From here on, for simplicity, these averaged overlapping measurements will be referred to as *datapoints*.

Step 4: Removing bad quality events

After averaging the data there is never more than one datapoint per Hankasalmi radar range cell per minute, but there can be less, or even none if the ESR is not turned on or the Hankasalmi radar does not receive backscatter from the range gates that overlap with the ESR range gates. The later happens because SuperDARN radars only receive backscatter from a certain range gate when there are ionospheric irregularities present in it and the Bragg condition is satisfied (see section 3.2 for a more detailed explanation). Events with less than 20 datapoints were automatically removed. This left approximately 50 events that were visually inspected to remove the events that were either too short (less than $\sim 1\,\mathrm{h}$ long) or that had a too low datapoint density (less than approximately one datapoint per second minute). A few events where the ESR radar was not in a fixed position were also removed. This left the list of 10 events presented in table 5.1. Note that at the geographic locations where the events occur, MLT≈UT+3h.

Event date	**Location**	**UT range**
11-12-1999	1	06:10-09:40
15-11-2001	2	01:30-05:30
08-01-2003	1	03:00-07:30
22-12-2003	1	07:40-10:00
08-01-2012	1	18:00-22:00
	3	18:00-24:00
21-02-2012	4	19:00-21:30
13-12-2012	2	10:30-13:20
14-12-2012	1	01:00-05:00
	2	09:00-12:30
04-02-2013	1	00:00-05:00
05-02-2013	1	02:30-04:40

Table 5.1: List of events, including the geographical location as given in figure 5.2 and the approximate time range in UT (MLT≈UT+3h). Some events contain large data gaps.

Figure 5.2 shows the field of view of the Hankasalmi radar in blue with the field of view of the MSP superposed. The 10 events are all located in one (or two) of the four locations marked in green.

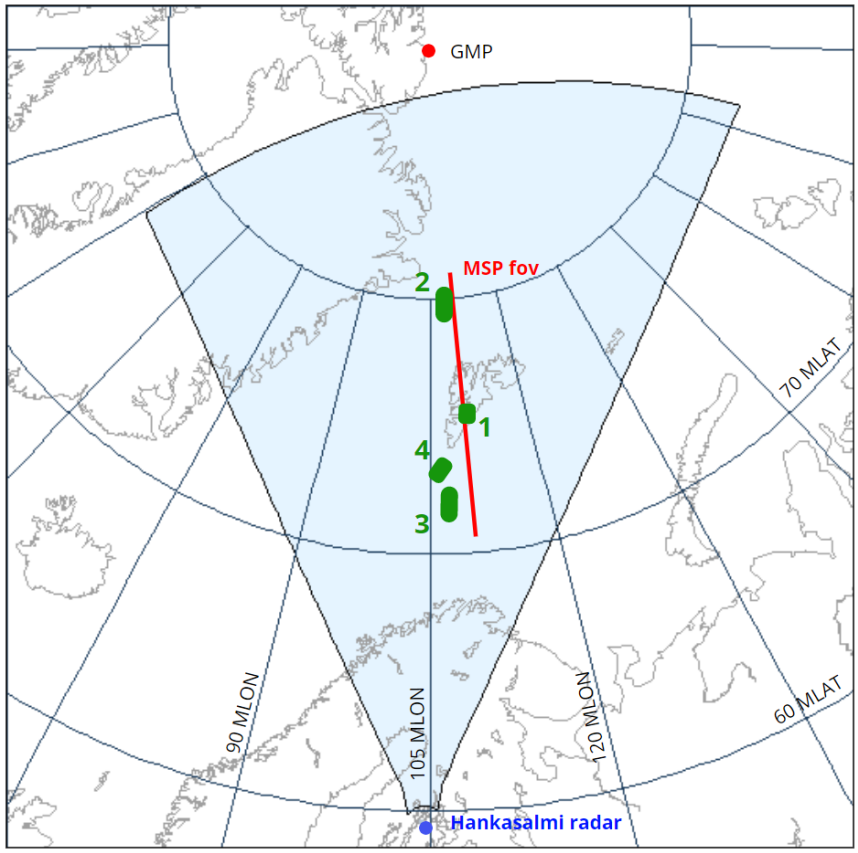

Figure 5.2: Field of view of the Hankasalmi radar with the field of view of the MSP at Longyearbyen superposed. The areas in green mark the regions with ESR and Hankasami radar backscatter. Region 1 is illuminated by the ESR in the field aligned position, while regions 2-4 are illuminated by the 32m dish in different positions.

5.3 Analysis and display of events

Since a significant part of the results in this thesis are based on case studies, the data from different events is presented in similar ways. In this section the data analysis done for each plot type is explained. In addition, other information relevant to understand the plots is also given.

Time series plots

These plots show a time series of the electron and ion temperature and the spectral width measured at each datapoint for an event. Figure 6.16 shows an example of such a plot.

Each subplot displays the spectral width measurements for a particular Hankasalmi radar beam range gate, and the averages of the electron and ion temperatures for the ESR range gates within it (as described in section 5.2). The magnetic and geographic latitudes of the middle of the Hankasalmi radar range gate are written on top of each subplot.

For some events the Pedersen and Hall height integrated conductivities are also shown. I have calculated the height integrated conductivities by integrating the conductivities as given in the analysed ESR data files from $80\,\mathrm{km}$ to $300\,\mathrm{km}$.

Sometimes it is possible to make a good estimate of whether the datapoints are on open or closed field lines by using MSP and ESR data. For the time periods and at the latitudes where this is the case, the subplots are shadowed to reflect this. Green indicates closed field lines whereas periods on open field lines are shadowed in red.

MSP plots

These plots show the intensities, in Rayleigh, measured by the MSP in the 6300Å and 5577Å wavelengths. Figure 6.14 shows an example of such a plot. Each scan of the MSP along the magnetic meridian is presented as a vertical line in these plots, with the y-axis indicating the elevation angles from 0° (northward-looking) to 180° (southward-looking). 90° indicates the zenith.

Green horizontal lines are used to mark the estimated elevation corresponding to the magnetic latitudes at which the overlapping Hankasalmi radar and ESR measurements were made for the event. More specifically, they mark the elevation corresponding to the magnetic latitude at the mid-point between the southernmost and northernmost magnetic latitude for the Hankasalmi radar range gate that overlaps with the ESR measurements. In order to convert between magnetic latitude and elevation, the altitude of the emissions is needed. In reality, this is not possible, since emissions do not come from *one* altitude, but rather from an altitude *range*. Here, the 5577Å emissions are assumed to come from an altitude of 130km, while the 6300Å emissions are assumed to come from 250km altitude. The error in the MLAT to elevation conversion is larger the further from zenith one goes. When the ESR is used in the field-aligned position it illuminates a volume that, at the altitudes studied, overlaps with two adjacent Hankasalmi radar range gates at $\sim$75MLAT. This is shown in the MSP graphs as two green lines around zenith. The measurements from the steerable 32 meter ESR dish overlap with up to six Hankasalmi radar range gates when the ESR dish is pointing at low elevations.

SW and MSP boundaries plot

A plot showing the relative position of the spectral width boundary and the polarward boundary in the 6300Å emissions is used to illustrate one of the events in the nigthside (figure 6.6).

In the nigthside, where there is only precipitation on closed field lines, the polarward edge of the 6300Å emissions is a well known proxy for the OCB (see for example Blan-

chard et al. 1995). For this event, the 6300Å emissions boundary is close to a step function and using a cutoff gives a boundary that upon visual inspection seems plausible. Starting at an elevation of 0° (north) and moving equatorward, the first elevation at which the intensity measured by the 6300Å channel of the MSP surpasses 1kR is taken as the boundary for that scan. The elevation angle is converted to a magnetic latitude as done in section 5.3. This is repeated for every scan.

To find the spectral width boundary for this event, a simplified algorithm inspired in the C-F threshold method (described in section 4.1) is used. The steps are as follows:

1. For every time step, start at first range gate, which is the range gate at the lowest latitude.

2. Move polarward until a range gate with a spectral width $\geq 200\,\mathrm{m\,s^{-1}}$ is found. This is range gate n.

3. Check that range gates $n+1$ and $n+2$ (the two range gates directly polarward of range gate n) have ionospheric backscatter. If this is not the case, go back to step 2.

4. If the average of the SW in range gates n to $n+2$ is $\geq 200\,\mathrm{m\,s^{-1}}$, range gate n is defined as the SWB for this time step. Otherwise, go back to step 2.

Note that a spectral width boundary is not found at every time step.

Hankasalmi radar plots

There are mainly two types of plots used, range-time plots and field-of-view plots. Both are plotted using RST.

- Range-time plots show the timeseries of one Hanksalmi radar beam (an example of such a plot can be seen in figure 6.17). The line-of-sight velocity, the spectral width and, for one event, the signal power are shown as individual range-time plots. Each point in these plots shows data from one range gate in the chosen beam, with the y-axis showing the magnetic latitude of said range gates. Areas in white show range gates from which there either was no backscatter, or the backscatter was determined to be ground scatter by the FITACF method, which uses the algorithm presented in Blanchard et al. (2009).

- Field-of-view plots show one parameter (in this case the line-of-sight velocity) for all range gates in all beams in one scan (approximately 1 minute). Ground scatter is marked in grey, while white means that there is no backscatter from that range gate.

In both types of plots, line-of-sight velocities towards the radar are positive, while negative velocities indicate that the plasma has a velocity component pointing away from the radar.

ESR overview plots

The ESR plots are plotted using a GUISDAP function called *vizu*, which is specifically designed to visualize EISCAT data. In the plots of the field-aligned data, the y-axis shows the altitude. In the plots of the data acquired by the 32m dish pointing at low elevations, the y-axis shows the geographic latitudes, with the magnetic latitudes in parenthesis. All four primary data products (electron density, electron and ion temperature and ion velocity) are shown. Ion velocities away from the radar are positive, while velocities towards the radar are negative. It is worth noting that the signs are opposite to those used for the plasma velocity measured by SuperDARN radars (for no particular reason other than convention).

Chapter 6

Results and discussion

Space physics deals with complex systems where processes are often controlled by a number of mechanisms that interact with one another. The instruments used to probe the plasma further complicate the analysis of the data by introducing sources of uncertainty. Given the complexity of the systems in play, the results must be valid to a high degree of certainty in order to be able to determine any cause and effect relationship. Statistical studies, which by their very nature incorporate larger datasets, are therefore the best way to mathematically determine and test competing theories. The challenge is that, as is the case in this thesis, it is often hard to find large enough datasets, specially when there is a need to combine data from multiple instruments that probe a common ionospheric volume (both spatially and temporally). This is not to say that case studies are of no value and indeed, studies of single events are routinely published (for example the Woodfield et al. (2002) study that gave the idea for this thesis) and help shed light into possible correlations that can be subsequently proved or disproved by statistical studies.

The aim of this thesis is to look at whether phenomena linked to particle precipitation, and thus temperatures and conductivities, have an effect on spectral widths. Particle precipitation is ultimately controlled by the interaction between the solar wind and the earth's magnetosphere and its properties differ according to its source region in the magnetosphere/magnetosheath. As such, its characteristics vary greatly with MLT, with latitude, and depending of whether the precipitation is on open or closed field lines. In order for a statistical approach to be effective the number of variables in the data must be restricted, but with only 10 events, this is challenging. Thus, most of the data analysis is done in the form of case studies. Four events, two in the nightside and two in the dayside, are chosen to be treated as case studies. Additionally, a small statistical study is done with the data in the flanks (that is, events that are neither in the dayside or the nightside).

6.1 Limitations in the data

Before we can start considering the events, it is important to look at the limitations in the data and how these might affect their interpretation. There are two main obstacles to finding cause and effect relationships with the data in this thesis. Firstly, there are uncertainties in the data, which can be divided in two groups: uncertainties that arise when comparing radar data, and uncertainties in locating the OCB. Secondly, and perhaps most importantly, missing and incomplete data is an issue. A discussion of these limitations is presented below.

6.1.1 Uncertainties in comparing coherent/incoherent radar data

In this thesis data from a coherent and an incoherent radar are directly compared. There are two things to keep in mind:

First and most importantly, the data for the two instruments might not always be co-located. The signal from SuperDARN radars propagates in the ionosphere before being backscattered, and the propagation path is dependent on ionospheric conditions. This means that a simple time of flight estimate is not enough, on its own, to determine the location of the backscatter (in this case, which range gate it comes from). Additionally, an assumption must be made as to the altitude of the backscattered signal. In the SuperDARN analysis a virtual height model is used. This leads to an uncertainty of $\pm$1-2 range gates when mapping the backscatter (see for example Yeoman et al. 2008). The significance of this in this study is that the spectral width measured at one datapoint can, in fact, come from up to $\sim$100km away from the electron and ion temperatures measured by the ESR.

Secondly, the difference in spatial resolution between SuperDARN radars and the ESR implies that the temperatures measured by the ESR might not be representative of the temperatures in the SuperDARN range gate as a whole. This is because an individual SuperDARN range gate covers a much bigger horizontal area ($\sim 45\,\mathrm{km} \times 45\,\mathrm{km}$) than the horizontal area covered by the scattering volume of the ESR ($\sim 3\,\mathrm{km} \times 3\,\mathrm{km}$ at F-region heights when the beam is field aligned). Imagine, for instance, a short-lived enhanced electron temperature. This would indicate particle precipitation in the scattering volume of the ESR, but this precipitation might be localized and affect only a small portion of the SuperDARN range gate. In such a situation, interpreting a SW measurement in terms of the ESR data could be misleading. This is one of the reasons why one should not, when looking at case studies, draw conclusion from individual datapoints, but rather from trends in the data.

6.1.2 Uncertainties in the location of the OBC

For long periods of time in most of the events, and particularly in the flanks, there is no clear signature of the OCB in the MSP data. This is due to meoscale structuring in the aurora which in the MSP is seen as high spatial and temporal variability in the emissions.

Areas of open and closed field lines appear to ”mix”, meaning that the the change from open to closed and viceversa is too quick to find a boundary for any significant amount of time.

Another issue is that when converting from the elevation angle of the MSP to a latitude, the altitude of the emissions must be assumed (as described in section 5.3). This leads to uncertainties in mapping the emissions to latitudes that increase the further from zenith one goes. Thus, the location of the OCB as seen in MSP data cannot necessarily be converted to the real latitude of the OCB, specially when the OCB is observed at low elevations (northwards or southwards) in the MSP. This is specially an issue for radar data at locations 2-4 in figure 5.2.

On top of that, the MSP only sees a 2-D section of the ionosphere. Some of the events have radar data from areas up to $\sim$100km away from the field of view of the MSP as shown in figure 5.2. The placement of the OCB is obviously location dependent, so this leads to uncertainties, specially when the OCB is close to the latitude at which the radar data are taken.

6.1.3 Size of dataset and incomplete data

The certainty in the results is reduced due to having a limited number of events, as mentioned in the introduction to this chapter.

The main driver behind the exclusion of events from the original list of 276 events is lack of overlapping data from the Hankasalmi radar. SuperDARN radars receive backscatter from an ionospheric volume only when the Bragg scatter condition is satisfied. For this to happen, there must be irregularities in the magnetic field in the decameter scale as well as a propagation path that makes the signal from the radar orthogonal to the irregularities. Often, these conditions are not met for the Hankasalmi radar range gates that overlap with the ESR beam, leading to the exclusion of events. Apart from excluding events, this also causes data gaps in the events. Even though the 10 events selected all include data from the Hankasalmi radar, sporadic lack of backscatter is still a problem. When the ionospheric conditions change, the propagation path also changes. If it changes enough, the backscatter from the range gates overlapping the ESR beam is lost and there is no overlapping data for a time period. Often, the overlapping data comes from the edges of the area where the Hankasalmi radar receives F-region backscatter. When this is the case, the backscatter is intermittent and there are recurrent small gaps in the data.

Lack of ESR data is also a problem. Some events are excluded due to the ESR not being turned on. There are also examples of lack of data in the 10 events used in this thesis, although this is a smaller problem. Specifically, some of the ESR data the 11th of December of 1999 cannot be fitted by GUISDAP. It is not clear why this is the case, but there are several factors known to lead to a failure to fit data, including a high signal-to-noise ratio due to high background noise (internal, due to electronics, or external) and/or low electron densities in the ionosphere, the plasma being non-thermal (meaning the velocity distribution is not Maxwellian) or not correlated within the one-minute integration time due to high variability. This results in lack of conductivity data for this event. Additionally, there

are some instances of short-lived lack of ESR data in some of the other events, but these last only for a few minutes and are only a minor contribution to the data gaps.

For some events, the MSP data is unclear due the presence of a cloud layer. This is rare as the original dataset had already been filtered with lack of MSP data being an exclusion criteria. However, some events with bad MSP data remained and one event that would otherwise have been included, had to be removed from the final dataset.

6.2 Case studies

To provide some structure the case studies are divided according to whether the radar data is mainly from the nightside or the dayside. For this propose nightside is defined as as MLT 00 ± 3h and dayside as MLT 12 ± 3h. As this thesis looks at the relationship between temperatures and spectral widths, the main aim is to either support or challenge the theories that involve particle precipitation. Additionally, the velocities measured by the Hankasalmi radar are used to look for indications of large scale velocity shears.

6.2.1 8th of January 2012, nightside

This event contains overlapping data for intermittent periods between 18UT and 00UT. It includes data from the 32m dish pointing south at low elevation, which overlaps with the Hankasalmi radar between 71.0-72.3MLAT (corresponding to range gates 27-30 of beam 8, marked as position 3 in figure 5.2) as well as some data from the field aligned ESR dish which overlaps the Hankasalmi radar backscatter at 75.1-75.5MLAT (corresponding to range gates 37 and 38 of beam 9, marked as position 1 in figure 5.2):

- At **75.1-75.5MLAT**, the Hankasalmi radar only received a signal for the first hour of the event (18-19UT) and for short periods of time around 21UT. Between 18-19UT, the MSP data in figure 6.1 shows occasional precipitation at both wavelengths, although most of the 5577Å precipitation is equatorward of the latitudes in question. Data from the 42m ESR dish in figure 6.2 shows evidence of short lived hard precipitation for a few minutes at the beginning of the event (before 18:05UT). It seems thus that this first hour is mostly on open field lines, with occasional closed lines mixing in. This is typical of the period before and after magnetic midnight. For most of the remaining event duration, the data is taken polarward of the OCB as evidenced by the lack of 5577Å precipitation shown in the MSP data. The period between 20:50UT and 21:10UT is the exception, shown clearly to be on closed field lines in the MSP data. This is corroborated by ESR data from the 42m dish showing increased E-region electron densities and increased F-region electron temperatures during that time, which are typical signs of high-energy ($>$1-10keV) auroral precipitation. The weak arcs that can be seen in the 6300Å plot for most of the event are the result of polar cap patch structures on opened field lines being transported anti-sunward due to the Dungey cycle. Polar cap patches are regions of increased

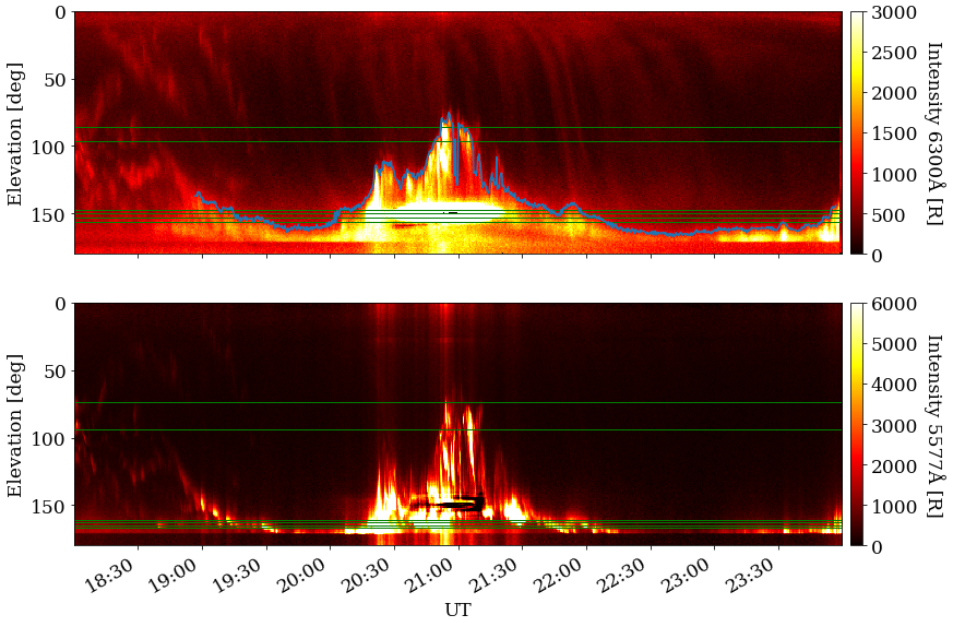

Figure 6.1: Elevation-time plot of the MSP for the 6300Å channel (top) and 5577Å channel (bottom) on the 8th of January 2012. The green lines show the latitude at which the data are taken. The blue line shows the boundary where the 6300Å precipitation intensity goes above 1000R.

electron densities that form due to EUV solar radiation in the dayside and convect towards midnight.

- At **71.0-72.3MLAT**, the Hankasalmi radar receives a signal for most of the event duration. However, placing it in relation to the OCB is not trivial. These latitudes correspond to very low elevations in the MSP data, and thus large uncertainties arise when mapping the auroral precipitation into a latitude. However, even accounting for this uncertainty the period between 20:15UT and 21:00UT is clearly on closed field lines given how the 5577Å channel shows precipitation at and around the measured latitudes. For the rest of the event, the most reliable method for assessing the position of the OCB is using the 32m dish ESR data shown in figure 6.3. When the 32m dish is pointing at low elevation in this manner, the method outlined by Aikio et al. (2006) can be used to accurately track the OCB. Briefly, this method is based on using the electron temperature enhancements associated with precipitating particles on closed field lines. At the latitudes of interest (71.0-72.3MLAT corresponding to 73.5-74.7GLAT), the electron temperatures are clearly increased between 18:30UT and approximately 19:40UT, as well as between 20:15UT and approximately 22:10UT and for the last 15 minutes of the event. Thus, during these periods, the measurements are on closed field lines. Between 19:40UT and 20:15UT, as well as between 22:10UT and approximately 23:10UT, the temperatures are low (less than $\sim$1000K) and the measurements are on open field lines. This is confirmed

by similar electron temperatures measured by the 42m dish located further poleward. Outside of these time periods, the data is inconclusive.

The auroral activity observed between ∼20UT and 21:30UT is associated with a substorm. This is confirmed by ground magnetometer data from the IMAGE network, which show evidence of a substorm occurring in that time period. This is most clearly observed in the X-component (north-south component, see figure 7.1 in appendix) of the magnetometer data, which shows a dip in this period corresponding to an enhancement in the East-West ionospheric current system, which is typical of substorms (Brekke, 2013).

The most notable feature in the spectral width measurements from the lower latitudes (71.0-72.3MLAT) shown in figure 6.4 is the jump seen at ∼21:30UT at 71.0-71.8MLAT (there is only sporadic data at 72.2MLAT at this time). The SWs increase from less than $50\,\mathrm{m\,s^{-1}}$ right before the jump to an average of $\sim 180\,\mathrm{m\,s^{-1}}$. This increase happens while on closed field lines, as defined using the ESR data itself, so a change from closed/open field lines cannot be used to explain the SW change. The temperatures do not provide any obvious clues either: The electron temperatures at 71.0-71.4MLAT show an increase of ∼500K about 10min before the SW jump, and the ion temperatures show a decrease of the same magnitude, but this happens mostly after the SW jump. A considerable decrease in both temperatures at 22:10UT, coinciding with the change from close to open field lines, does not lead to any marked change in the SWs which remain moderate (above $100\,\mathrm{m\,s^{-1}}$) for the rest of the event. What, then, could be causing this SW jump? One possibility is ionospheric turbulence caused by the polar cap patches seen in the MSP 6300Å emissions. Jin et al. (2014) showed that regions of enhanced plasma irregularities such as polar cap patches can be highly turbulent, specially when merging with the auroral region. The jump in SWs, which happens in a region close to the polarward boundary of the auroral region, could thus be explained by polar cap patches merging with the auroral oval.

Another interesting phenomenon seen in the timeseries in figure 6.4 is the fact that the increase in SW at ∼21:30UT appears to happen on closed field lines. Figure 6.6 shows the spectral width boundary together with the 6300Å boundary (which is a proxy for the OCB) for this event. The boundaries are calculated as described in section 5.3. Note that the 6300Å boundary is also plotted in the MSP plot in figure 6.1 for context. The first thing to notice is that, throughout most of the event, the SW boundary is not well-defined. One exception is the period between 21:40UT and 22.00UT where the SW boundary is well-defined and can be clearly seen moving equatorward from approximately 71°MLAT to 68°MLAT. At the same time, the OCB as defined by the 6300Å boundary is located up to 3° polarward of the SW boundary. The OCB as defined by the ESR is also located several degrees polarward of the SW boundary, which corroborates the fact that, for this 20 minute period, the SW boundary is located exclusively on closed field lines. Woodfield et al. (2002) showed in a case study that the SWB in the post-midnight sector (6-9MLT) could be located on closed field lines. Our results extend those findings into the midnight sector (∼1MLT) and support the theory presented in Lester et al. (2001), which noted that substorms might cause a breakdown of the relationship between the SWB and the OCB.

Other features worth noting are two periods of sustained low SWs (less than $50\,\mathrm{m\,s^{-1}}$) in this event at latitudes 71.0-71.8MLAT (see figure 6.4): for ∼40min the start of the event,

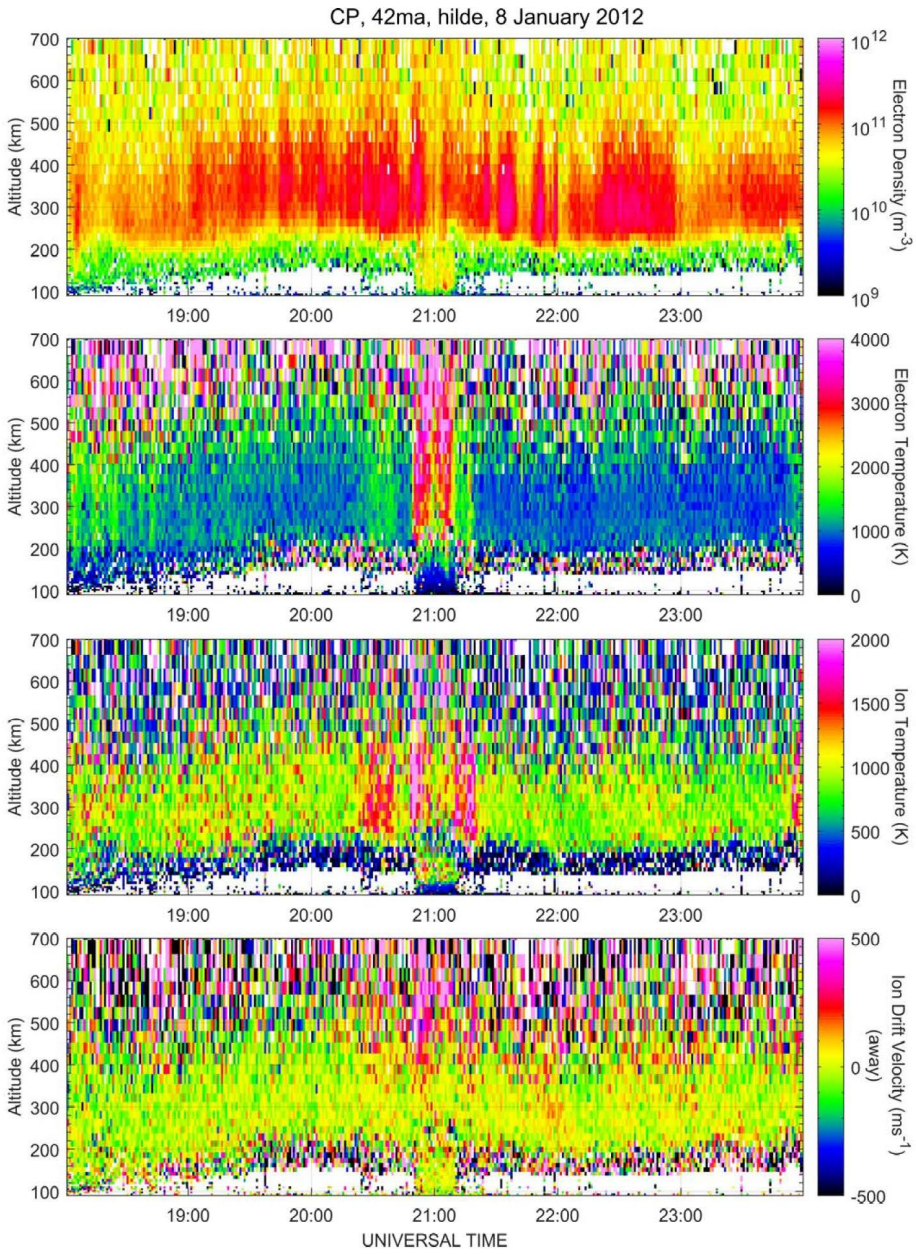

Figure 6.2: Altitude-time plot of the electron densities, ion and electron temperatures and ion line-of-sight velocities measured by ESR field aligned dish on the 8th of January 2012.

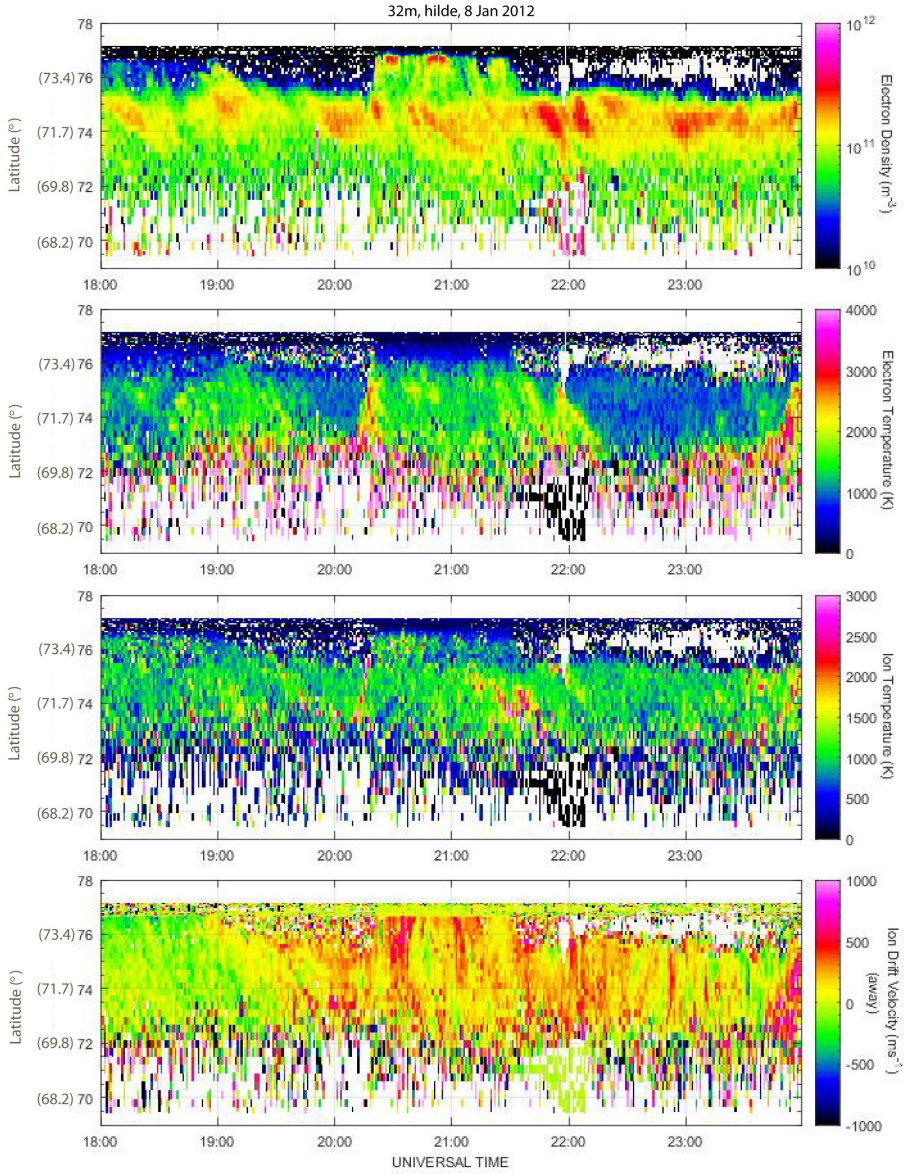

Figure 6.3: Geographic latitude vs time plot of the electron densities, ion and electron temperatures and ion line-of-sight velocities measured by the 32m ESR dish looking low elevation south on the 8th of January 2012. Corresponding magnetic latitude in parenthesis.

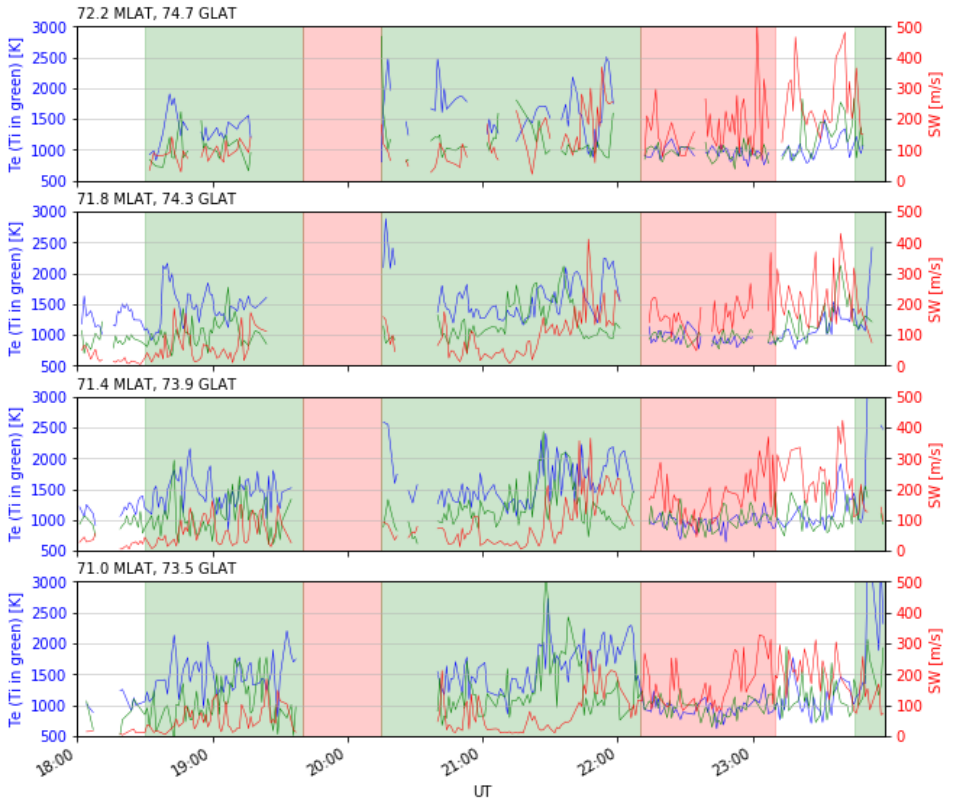

Figure 6.4: Timeseries of electron temperatures (blue), ion temperatures (green) and spectral widths (red) on the 8th of January 2012. The temperatures are measured by the ESR 32m dish pointing at low elevation towards the south. The SWs are measured by the Hankasalmi radar. Green and red shading indicate close and open field lines respectively.

and for a ∼20min period from 21UT. Could these periods be associated with high-energy precipitation? Neither of the low SW periods happen on open field lines, and so precipitation is indeed a possibility. However, if that was the case, we would expect to see a simultaneous increase in F-region electron temperatures, something that we do not see. Where we do see high electron temperatures is in the short period on closed field lines between 20:50UT and 21:10UT at 75.5MLAT, as shown in figure 6.5. Electron temperatures of up to 3000K together with the MSP data clearly show that there is high-energy precipitation. The Pedersen and Hall conductivities also show a peak in this period. By 21:15UT the electron temperatures have decreased to 1000K, and the conductivities have fallen to below 1 S. Despite this clear change of regimes, the spectral widths remain stable around $150\,\mathrm{m\,s^{-1}}$. Thus, for this event we do not see signs of high-energy precipitation suppressing SWs, as had been proposed by Parkinson et al. (2004) and Ponomarenko and Waters (2006).

Figure 6.5: Timeseries of electron temperatures (blue), ion temperatures (green) and spectral widths (red) on the 8th of January 2012. The temperatures are measured by the ESR field aligned dish and the SWs are measured by the Hankasalmi radar. Green and red shading indicate close and open field lines respectively. Height integrated Hall (green) and Pedersen (blue) conductivities are also shown.

Figure 6.7 shows a range-time plot of beam 8 of the Hankasalmi radar. Visually comparing the line-of-sight velocities and the SWs shows that SWs are enhanced close to, and polarward of, the region where the velocities start to increase. This is not unusual: this ”velocity boundary” is how the boundary at which the plasma flow in the ionosphere reverses direction from sunward to anti-sunward (due to the Dungey cycle) is expected to appear in this MLT sector. This boundary is called the Convection Reversal Boundary (CRB), and it is widely accepted to be located close to the OCB (see for instance Sotirelis et al. 2005). Thus, figure 6.7 mostly shows what we already know: the SWs increase in the vicinity of the OCB. It also shows that polarward of the OCB/CRB the velocities seem to be not only higher but also more variable. Although velocity gradients, specially near the CRB, could contribute to the higher SWs by creating velocity shears and thus turbulence, it is not possible to reach a conclusion from this data.

All in all, there is remarkably little correlation between temperatures and SWs for this event. This gives reason to suspect that it is not particle precipitation but some other variable that is at play. One possibility is turbulence due to polar cap patches, but the data is not conclusive and other options, like ULF waves or Kelvin-Helmholtz instabilities cannot be ruled out. Furthermore, there is no evidence that highly energetic particle precipitation suppresses SWs. This event also re-enforces the notion that in the midnight sector the SWB is not a reliable proxy for the OCB.

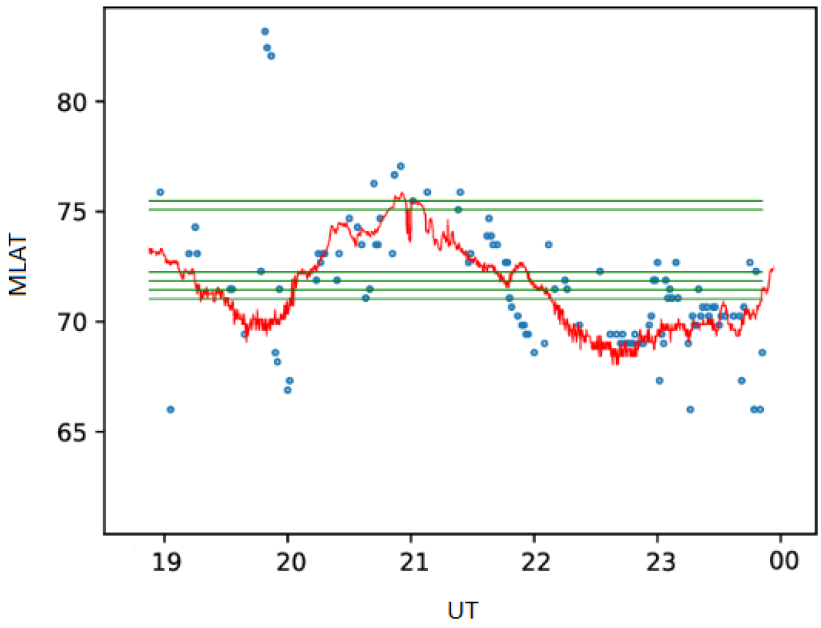

Figure 6.6: 6300Å boundary (red), spectral width boundary (blue dots) and location where the overlapping radar data are taken (green) for the 8th of January 2012.

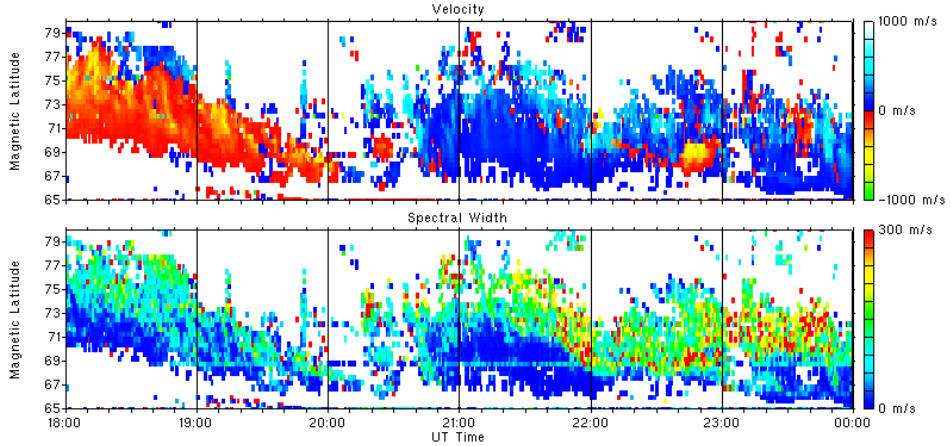

Figure 6.7: Magnetic latitude vs time plots of the line-of-sight velocity and spectral widths measured by beam 8 of the Hankasalmi radar on the 8th of January 2012. Velocities towards the radar are positive, away from the radar are negative.

6.2.2 21st of February 2012, nightside

This event lasts from 19UT to 20:30UT. While both ESR dishes are active, only the 32m dish that is pointing at 45° elevation towards the south intersects a volume from which the Hankasalmi radar has backscatter. The SW measurements come from range gate 32 of beam 7 and range gate 33 of beam 8. This is marked as position 4 in figure 5.2. Since the datapoints come from a non-field aligned dish, it it not possible to calculate the height integrated conductivities.

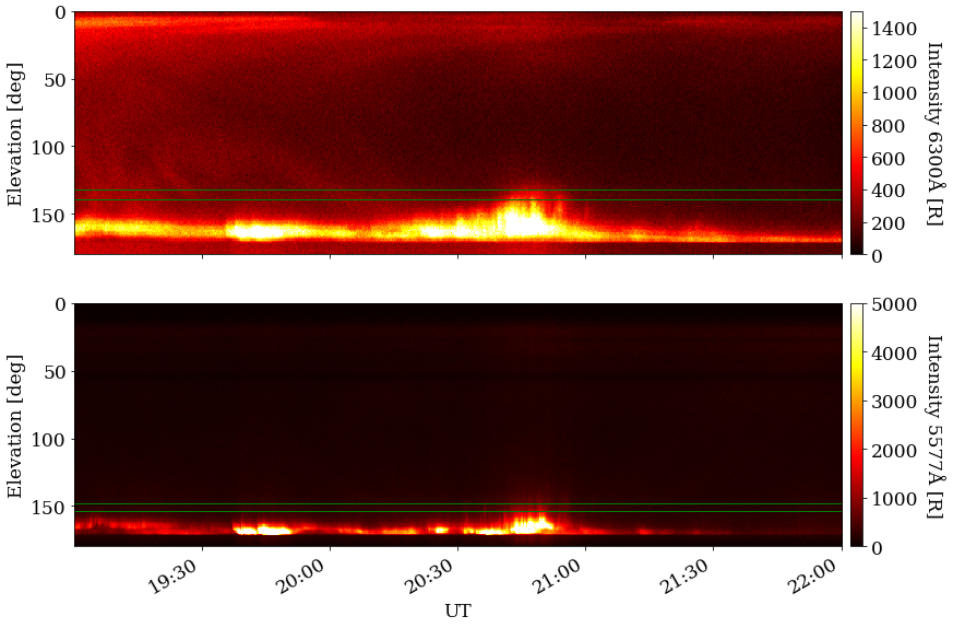

Figure 6.8: Elevation-time plot of the MSP for the 6300Å channel (top) and 5577Å channel (bottom) on the 21st of February 2012. The green lines show the latitude at which the data are taken.

From the MSP data in figure 6.8 it is obvious that the data is located polarward of both emissions, and thus on open field lines, for nearly the whole event. There is a possible exception to this around 20:45UT where the precipitation is close enough to the datapoints in latitude that it could, when allowing for some error in the elevation-latitude conversion, potentially be co-located. However, the ESR data shown in figure 6.9 shows no electron temperature enhancements at the latitudes of interest (73-73.5MLAT, equivalent to 75.2-75.8GLAT). There are some weak electron density enhancements during the first hour of the event, but since the electron temperatures remain low ($\sim$1000K), particle precipitation is not present and thus it is quite clear that all of the event is on open field lines. The MSP 6300Å emissions show no indication of polar cap patches like the ones seen in the 8th of January 2008 event.

Figure 6.10 shows the temperatures and SWs timeseries for the event. The electron and the ion temperatures are low and stable for the whole event, fluctuating slightly around

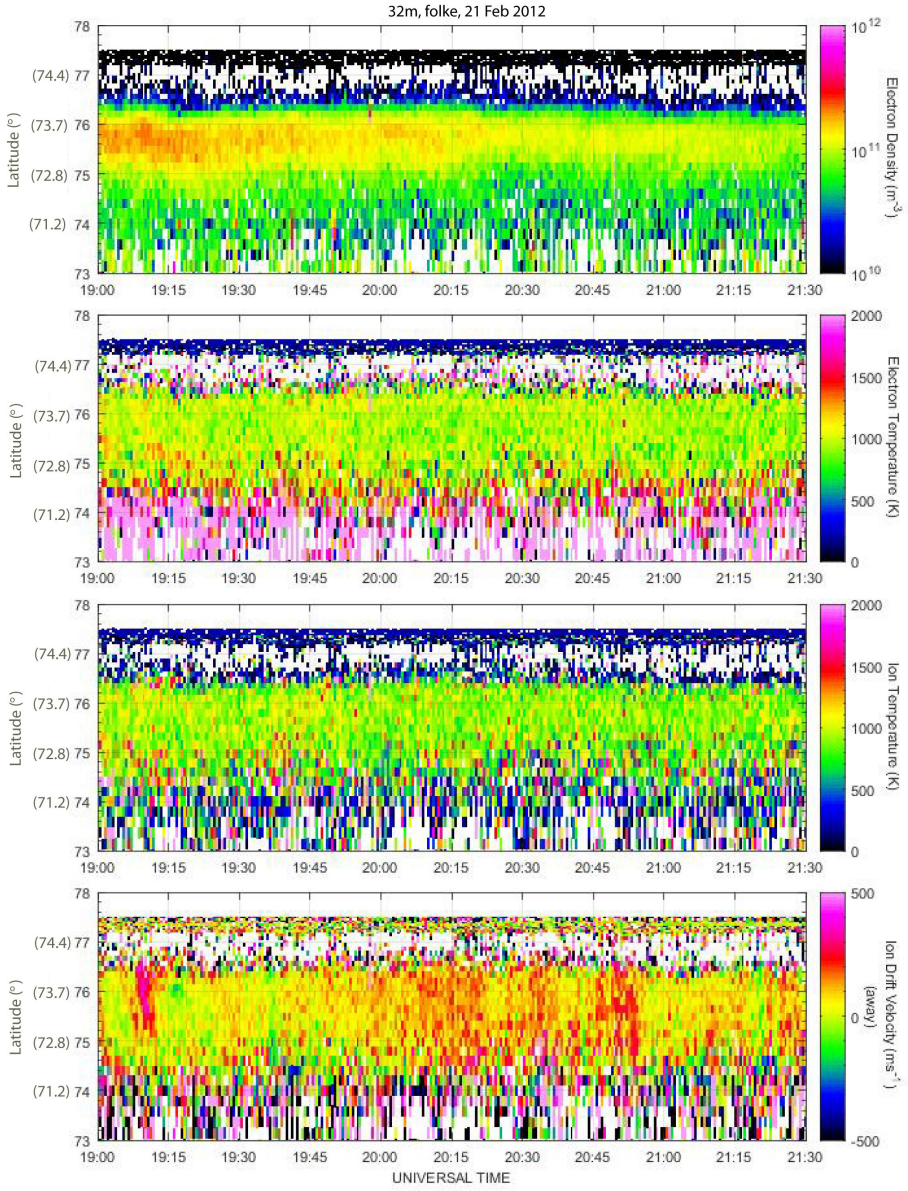

Figure 6.9: Geographic latitude vs time plot of the electron densities, ion and electron temperatures and ion line-of-sight velocities measured by the 32m ESR dish looking low elevation south on the 21st of February 2012.

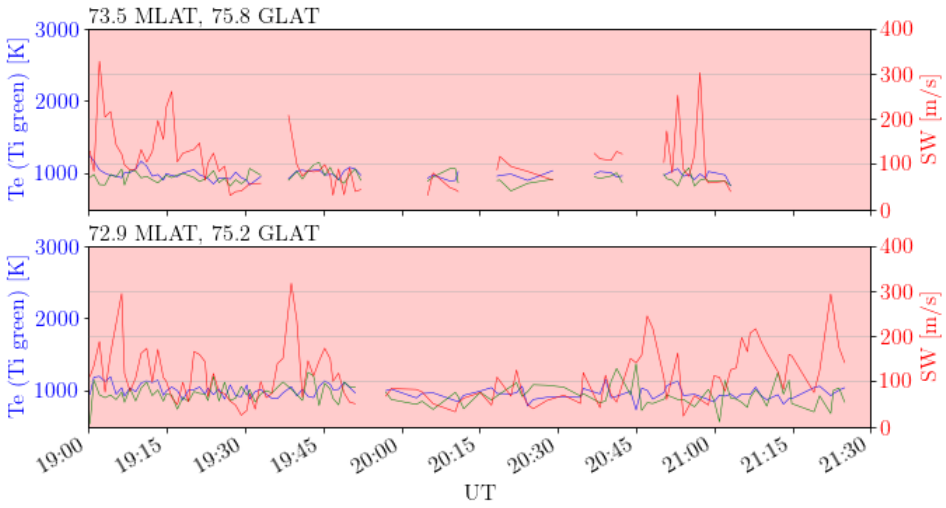

Figure 6.10: Timeseries of electron temperatures (blue), ion temperatures (green) and spectral widths (red) on the 21st of February 2012. The temperatures are measured by the ESR southward-looking dish. The SWs are measured by the Hankasalmi radar. Red shading indicates that the data are taken on open field lines.

1000K. This is as expected on open field lines in the nightside. The spectral widths are moderate, with most measurements being in the $60\,\mathrm{m\,s^{-1}}$ to $120\,\mathrm{m\,s^{-1}}$ range. This is significantly lower than the SWs seen on open field lines during the 8th of January 2012 event, something that could be linked to the lack of polar cap patches in this event. Although the SWs are moderate, there are peaks of up to $300\,\mathrm{m\,s^{-1}}$ at the start (until ∼19:45UT) and more sustained increases towards the end (from ∼20:40UT) of the event. The temperatures are stable throughout the event, and thus these SW increases are not correlated with temperature changes.

Figure 6.11 shows the backscatter received by beam 8 of the Hankasalmi radar (beam 7 shows very similar scatter). The spectral width plot shows that, for most periods, the SWs are higher and more sustained equatorward of 73-73.5MLAT where the data are taken. This is consistent with the general decrease in SWs seen polarward of the spectral width boundary reported by Villain et al. (2002) (see section 4.1). Figure 6.11 also shows that the plasma is moving towards the radar at higher latitudes, and away from the radar at lower latitudes. This matches the prevailing flow direction inside the polar cap in the nightside. Figure 6.12 shows the velocities across the field of view of the Hankasalmi radar at 20:00UT, which supports this. At 20:45UT, the flow becomes more unstable, particularly in the region south of Svalbard. This is shown in figure 6.13, which shows a sequence of field-of-view velocity plots from 20:45UT to 21:35UT at 10 minutes intervals. This suggests that the increases in SW after 20:40UT could be related to the turbulent flow in the vicinity and slightly poleward of the OCB.

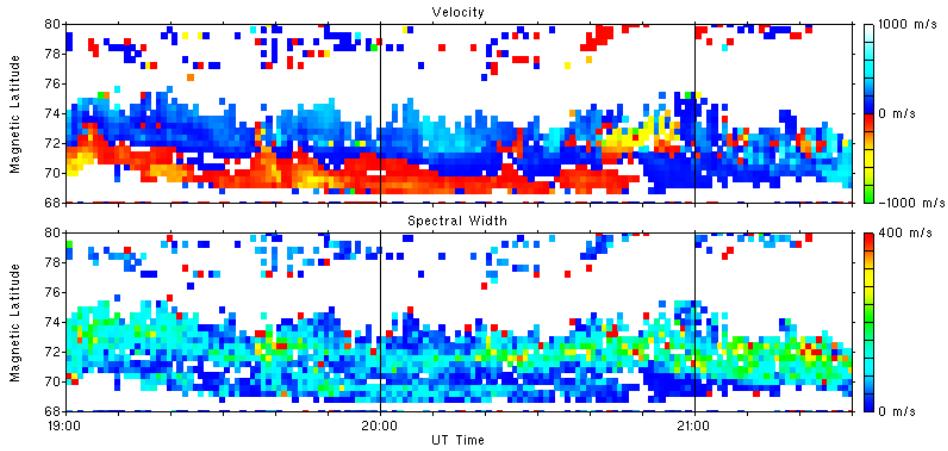

Figure 6.11: Magnetic latitude vs time plots of the line-of-sight velocity and spectral widths measured by beam 8 of the Hankasalmi radar on the 21st of February 2012. Velocities towards the radar are positive, away from the radar are negative.

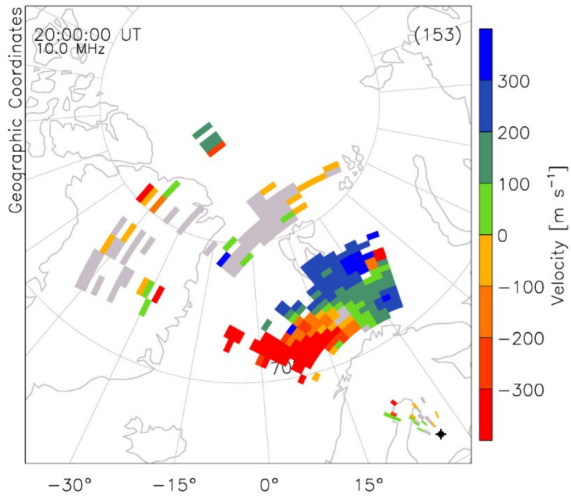

Figure 6.12: Field-of-view plot of the Hankasalmi radar on the 21st of February 2012 at 20UT. Velocities towards the radar are positive, away from the radar are negative. Ground scatter marked in grey.

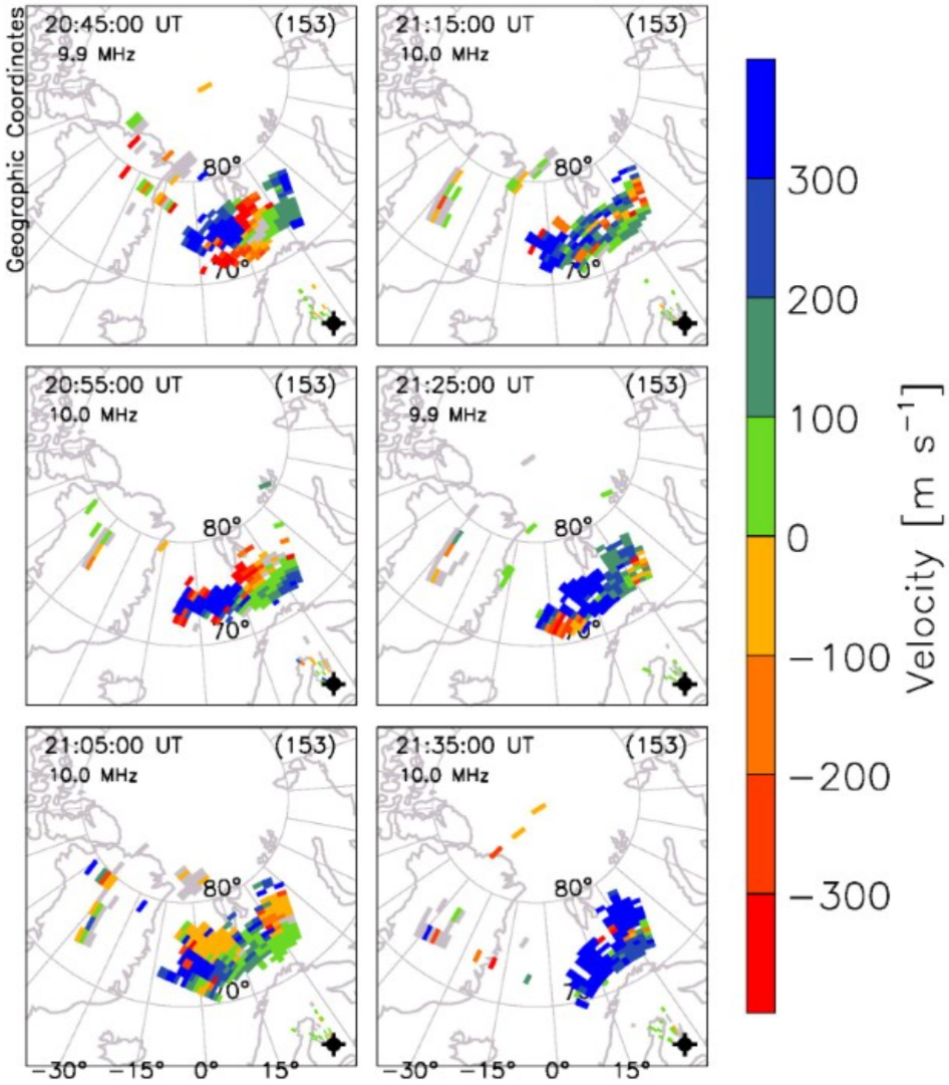

Figure 6.13: Field-of-view plots of the Hankasalmi radar on the 21st of February 2012 between 20:45UT and 21:35UT. Velocities towards the radar are positive, away from the radar are negative. Ground scatter marked in grey.

6.2.3 11th of December 1999, dayside

This event includes data from 06UT to 09:40UT. The SW measurements come from range gates 37 and 38 of beam 9, which intersect the field-aligned ESR beam from the 42 meter dish in the F-region. This is marked as position 1 in figure 5.2. The data density for these range gates is good, while the range gates intersecting the 32 meter ESR dish at the altitudes of interest show scatter that is too sparse to be included.

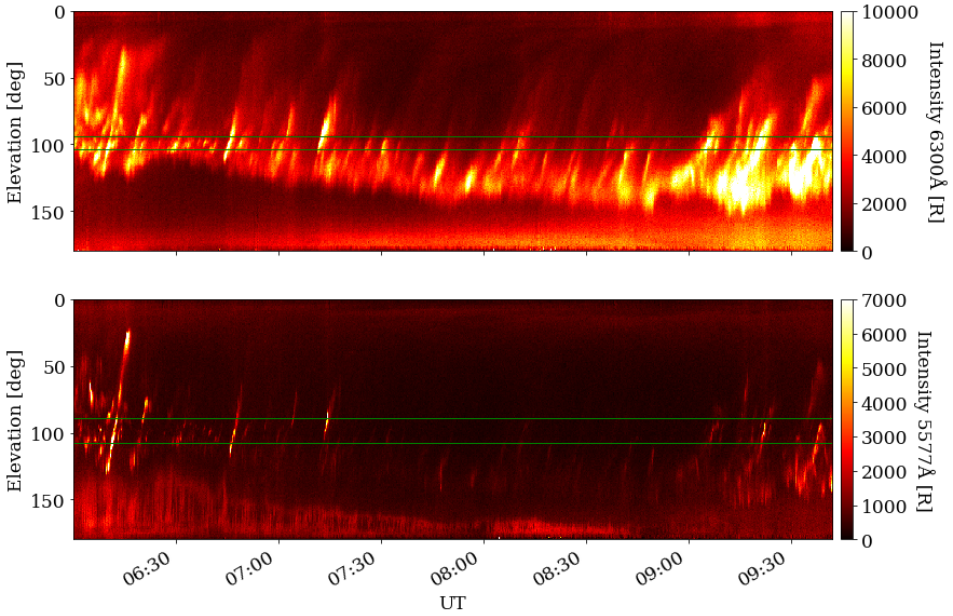

Figure 6.14: Elevation-time plot of the MSP for the 6300Å channel (top) and 5577Å channel (bottom) on the 11th of December 1999. The green lines show the latitude at which the data are taken.

The 6300Å MSP plot in figure 6.14 shows that emission enhancements in this wavelength, indicative of low-energy (<1keV) precipitation, start equatorward of the latitudes at which the measurements are taken at all times. However, the 5577Å MSP plot shows intermittent activity at the latitudes of interest, predominantly before 07:20UT and after 09:10UT. Since the high-energy particles (>1-10keV) needed to create these emissions precipitate along closed field lines, the occasional presence of strong green emissions in areas otherwise dominated by red emissions indicates a mixture of open and closed field lines. What we are seeing before 07:20UT and after 09:10UT is likely the ionospheric footprint of the low-latitude boundary layer (LLBL) which contains a mixture of low-energy magnetosheath particles and high-energy magnetospheric particles (Moen et al. 1996) and is though to be on a mixture of closed and opened field lines (see for example Dong et al. 2019). The measurements from 07:20UT to 09:10UT are mostly on open field lines, as the bulk of the green emissions happen equatorward of the latitudes of interest. The latitudes dominated by 6300Å emissions between these times are indicative of the cusp, and thus the radar measurements at these times are taken from both inside the cusp

and polarward of the cusp. Polarward moving auroral forms (PMAFs) are seen as 6300Å emissions extending polarward of the the latitudes of highest auroral activity. PMAFs are known to appear in the cusp (see for example Frey et al. 2019), and thus strengthen the suspicion that the radar measurements between 07:20UT to 09:10UT are indeed taken in or polarward of the cusp.

An increase in electron density in the E-region as shown by an altitude-time ESR plot would show without ambiguity that the ESR beam illuminates an area with high-energy precipitation (and thus on closed field lines). For this event, seeing whether there are such increases in E-region density at the time periods where the beam is suspected to illuminate the the ionospheric footprint of the LLBL (before 07:20UT and after 9:10UT) could confirm such suspicions. Figure 6.15 shows that this is indeed the case before 06:15UT, when enhanced E-region densities are seen. However, in this case, most of the ESR data below $\sim 300\,\mathrm{km}$ between 06:15UT and 07:40UT and below $\sim 250\,\mathrm{km}$ between 07:40UT and 09UT could not be fitted by GUISDAP (shown as white gaps in figure 6.15). This could be due to an instrumental artifact or it could be a function of the plasma measured having too low densities. This also makes calculating the height integrated conductivities impossible, since conductivities are calculated from primary ESR data (electron density and temperatures) and the largest contribution to the height integrated conductivities comes from the E-region.

Figure 6.16 shows the time series of the SWs and the F-region electron and ion temperatures for this event. The electron temperatures before 07:20UT are mostly above 2000K and fall below that after 08:00UT, before increasing again after 09:10UT. The higher electron temperatures are related to the increased particle precipitation (both red and green) shown in the MSP. The spectral widths show a marked increase sometime between 07:20UT and 08:00UT, where they go from being mostly $<150\,\mathrm{m\,s^{-1}}$ to mostly $>150\,\mathrm{m\,s^{-1}}$. At the same time, the variability in the SWs increases. It has been shown that spectral widths in the cusp show high variability (see section 4.1). The times with high and variable SW roughly match the time period where the MSP observed no green emissions at the latitudes of interest. This could be interpreted as fitting in with the theory that, while structured low-energy precipitation leads to higher spectral widths, high-energy precipitation suppresses them. After 09:10UT, however, the SWs do not noticeably decrease, even though the electron temperatures increase and the MSP shows 5577Å emissions in that region. It is not clear why this is the case, but it can indicate that some other mechanism unrelated to high-energy particle precipitation is also leading to the low-medium SWs before 07:20UT.

The range-time plots of the Hankasalmi radar's line-of-sight velocities and spectral widths in figure 6.17 show that the spectral width boundary is located slightly polarward of 75MLAT between 06:00UT and 07:00UT. There are periodic increases in the velocities equatorward of this boundary (between 72MLAT and 75MLAT) during this period, while the SWs remain low. Fast flows are thus not responsible for the increased SWs in this event. Throughout the event, the velocities polarward of the spectral width boundary are consistently high and anti-sunward as expected from the Dungey cycle.

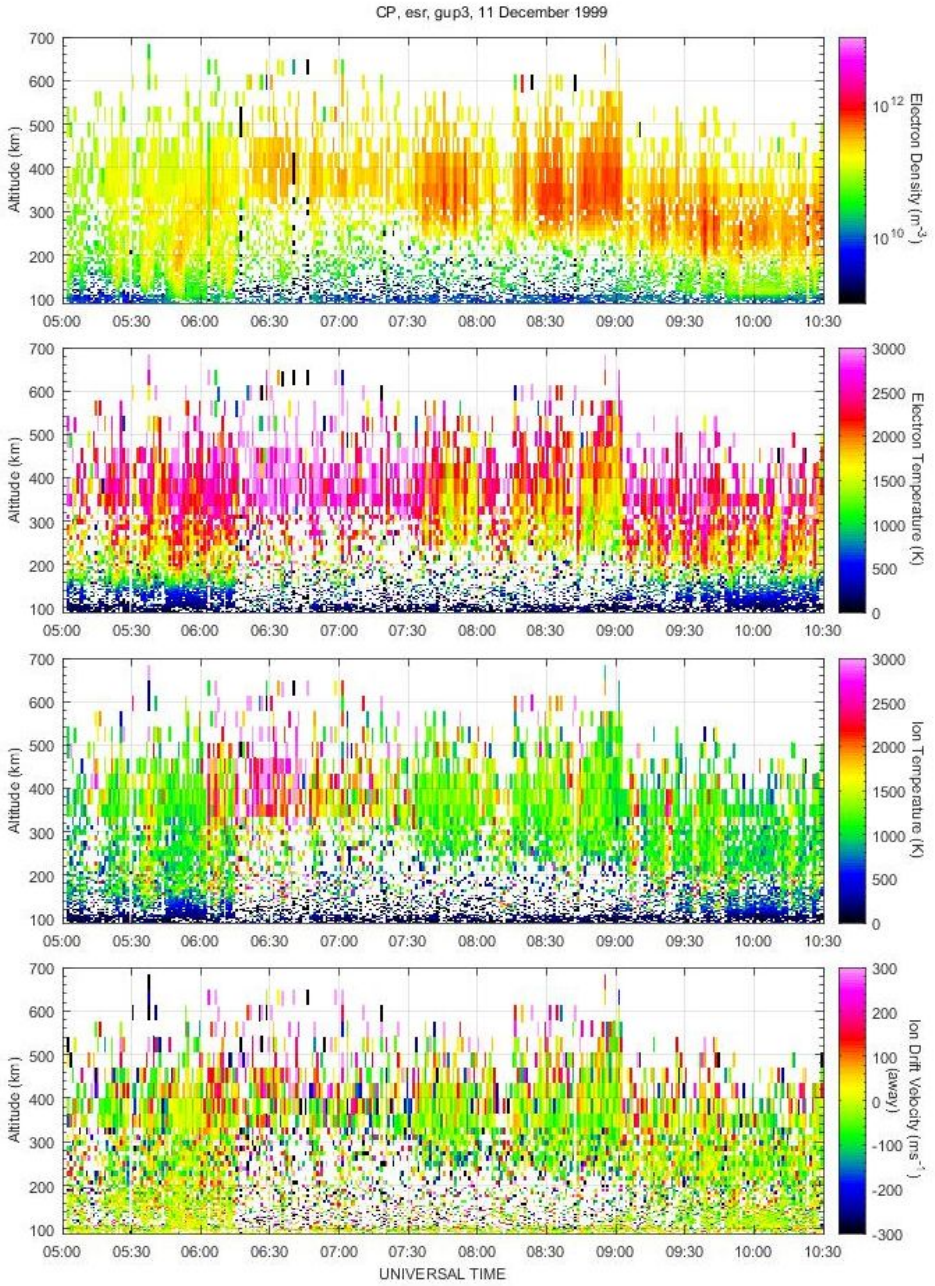

Figure 6.15: Altitude-time plot of the electron densities, ion and electron temperatures and ion line-of-sight velocities measured by ESR field aligned dish on the 11th of December 1999.

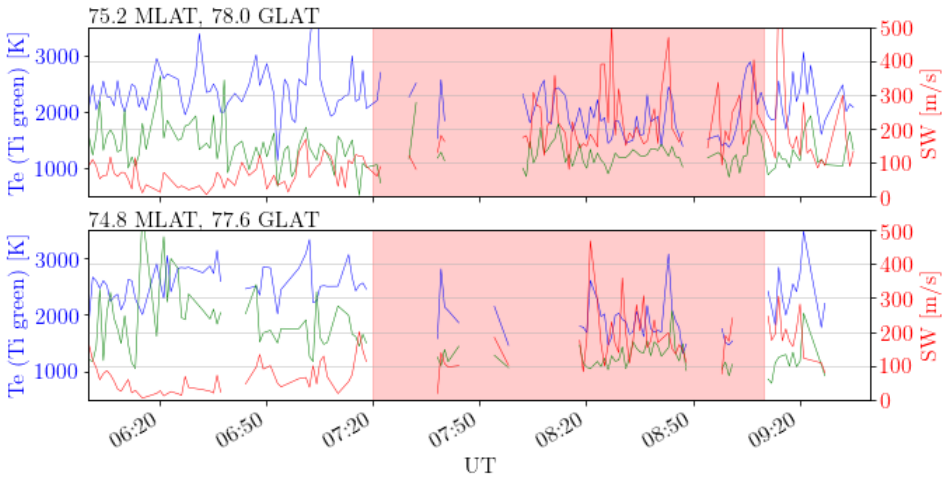

Figure 6.16: Timeseries of electron temperatures (blue), ion temperatures (green) and spectral widths (red) on the 11th of December 1999. The temperatures are measured by the ESR field aligned dish. The SWs are measured by the Hankasalmi radar. Red shading indicates that the data are taken on open field lines.

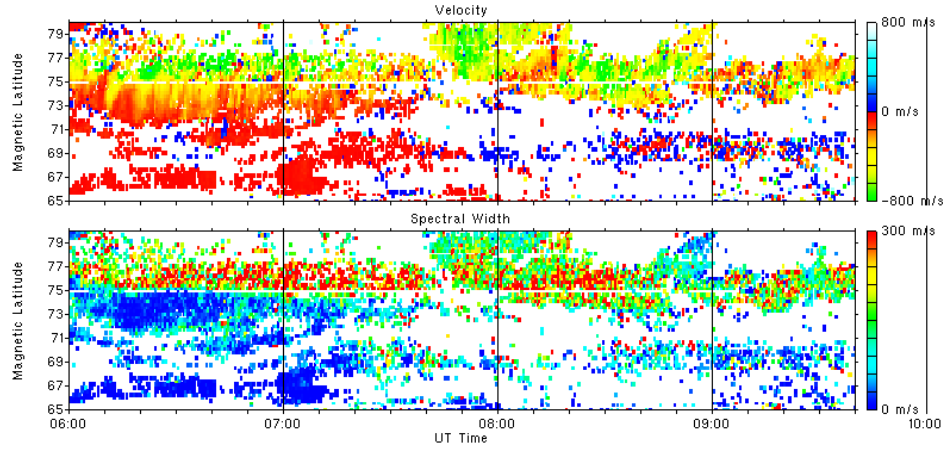

Figure 6.17: Magnetic latitude vs time plots of the line-of-sight velocity and spectral widths measured by beam 9 of the Hankasalmi radar on the 11th of December 1999. Velocities towards the radar are positive, away from the radar are negative.

6.2.4 22nd of December 2003, dayside

For this event there is sufficiently high data density between 07:40UT and 10:00UT. The radar data come from the Hankasalmi radar range gates 37 and 38 of beam 9 at 74.9MLAT and 75.3MLAT, which overlap with the ESR in the field aligned position. This is marked as position 1 in figure 5.2.

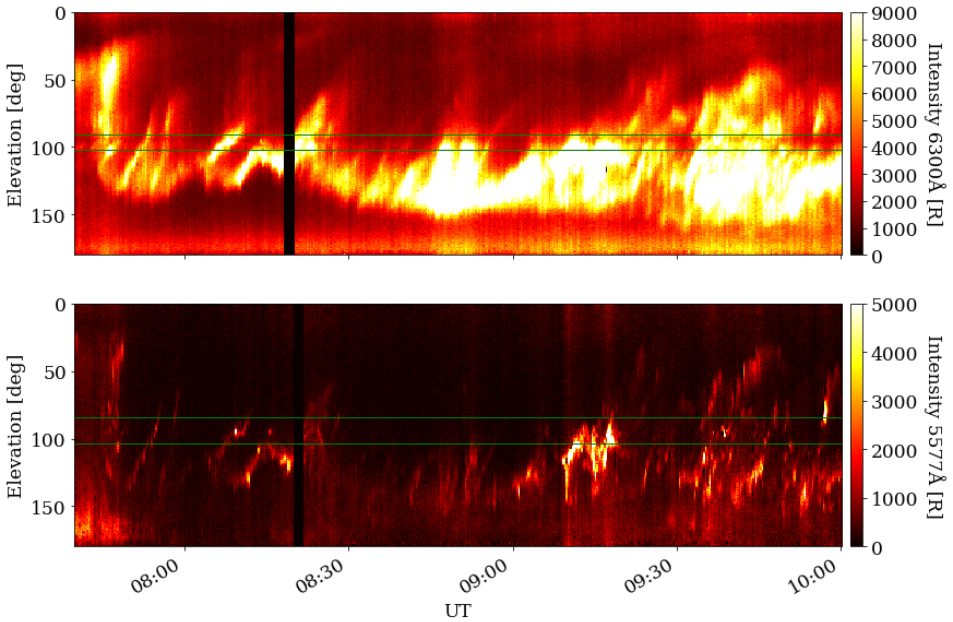

Figure 6.18: Elevation-time plot of the MSP for the 6300Å channel (top) and 5577Å channel (bottom) on the 22nd of December 2003. The green lines show the latitude at which the data are taken.

Figure 6.18 shows the MSP plot for this event. There are two short periods, marked in black, where the data is missing due to instrumental malfunction. From ∼08:30UT to ∼09:00UT, 5577Å emissions are recorded exclusively equatorward of the radar data, and this period must thus be on open field lines. The situation outside of this period is more complex, as there is a mixture of 5577Å and 6300Å precipitation. As it was the case in the 11th of December 1999 event, this is probably the ionospheric footprint of the LLBL and thus on a mixture of open and closed field lines. The ESR plot in figure 6.19 shows no evidence of E-region precipitation between 08:30UT and 09:00UT, thus confirming that the radar measurements in this period are polarward of the OCB. This period might in fact extend until 9:10UT. However, the fact that the precipitation at this time reaches the upper E-region (150km altitude), together with the weak 5577Å emissions seen in the MSP at the altitudes of interest makes it uncertain whether the this ten minute period is exclusively on open field lines. What is indeed clear is that the radar beam illuminates a region of closed field lines with high-energy precipitation between 9:10UT and 9:20UT, as shown by the increases in E-region electron densities. The same is true for a ∼5 minute

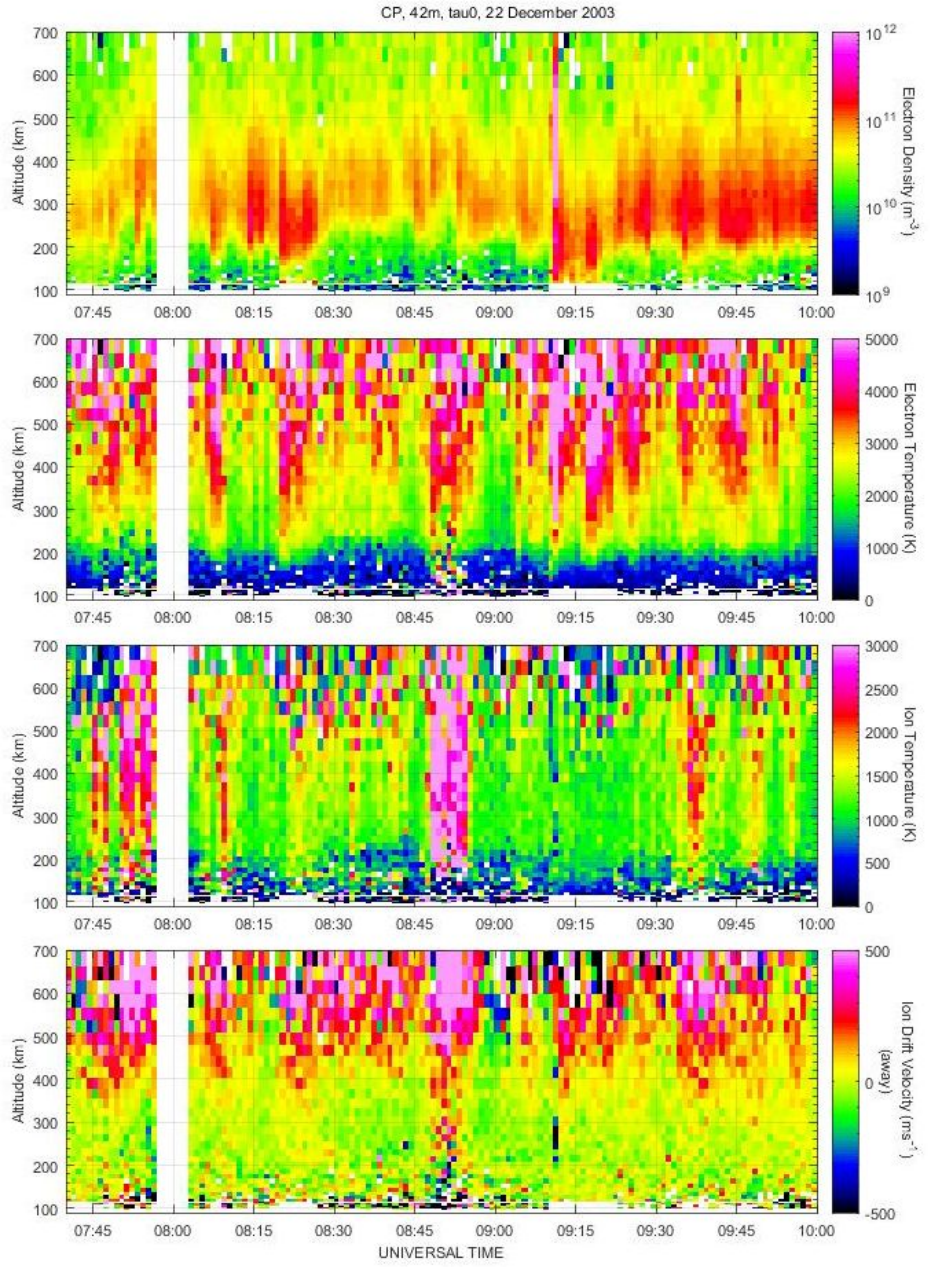

Figure 6.19: Altitude-time plot of the electron densities, ion and electron temperatures and ion line-of-sight velocities measured by ESR field aligned dish on the 22nd of December 2003.

period from 8:20UT. Short-lived density increases in the upper E-region can also be seen sporadically before 08:20UT as well as after 09:20UT, corroborating the theory that this region is quickly varying between open and closed field lines. It is also worth noting the sharp increase in ion and electron temperatures at 8:47UT lasting until 08:55UT, which are a sign of frictional heating. The ion up-flow generated by the frictional heating can be seen in the ion line-of-sight velocities in figure 6.19.

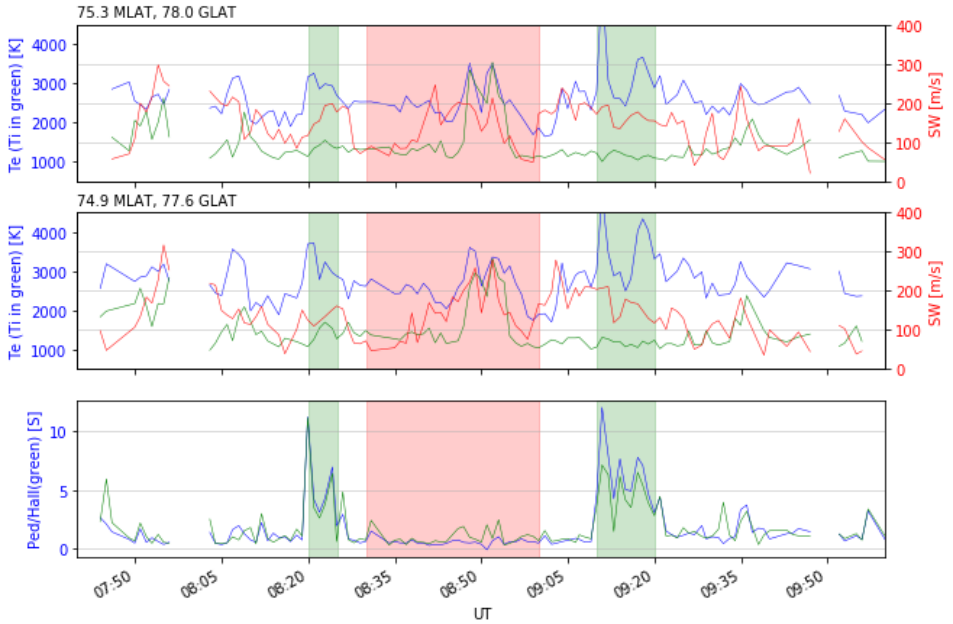

Figure 6.20: Timeseries of electron temperatures (blue), ion temperatures (green) and spectral widths (red) on the 22nd of December 2003. The temperatures are measured by the ESR in the field aligned position. The SWs are measured by the Hankasalmi radar. Red shading indicates that the data are taken on open field lines, green is closed field lines.

This increase in F-region temperatures is also shown in the timeplot in figure 6.20. The timeplot shows two peaks in the temperatures centered around 08:50UT. At the peaks, the ion temperatures are doubled from 1500K before the increases to 3000K and the electron temperatures increase by ∼1000K to over 3000K. These two peaks happen at the same time as the two regions of 6300Å emissions seen in the MSP in figure 6.18. The temperature increase is accompanied by a SW increase with SWs of up to $250\,\mathrm{m\,s^{-1}}$ at 74.39MLAT and up to $200\,\mathrm{m\,s^{-1}}$ at 75.3MLAT. It is worth noting that the increased SWs do not perfectly match the period with increased temperatures, as evidenced by the SW peak at 75.3MLAT at 08:40UT. However, the trend is clear and shows a positive correlation between SWs and temperatures on open field lines for this event. The cause of the high SWs could be the intense soft particle precipitation itself, through either structuring of the scattering targets as argued by Ponomarenko et al. (2007) or structured field aligned currents as proposed by Huber and Sofko (2000). However, subsequent increases in elec-

tron temperatures are not correlated with SW increases. The line-of-sight velocity plot of the Hankasalmi radar in figure 6.21 show a period of horizontal flows of up to $800\,\mathrm{m\,s^{-1}}$ around 08:50UT. This fast flow is probably the cause of the frictional heating and subsequent ion up-flow, and a more likely explanation for the increased SWs is thus that they are caused by turbulence resulting from a combination of the horizontal and vertical velocities.

The timeseries also shows a peak in the SWs at 07:50UT. However, the range-time plot of the Hankasalmi radar reveals a large area of intermittent scatter in this region that appears to be noise. This suspicion is confirmed by the very low power received from this region (see the upper panel in figure 6.21). The same applies to the period after 09:45UT. Because of this, the spectral width data cannot be trusted in either of these periods.

Other features seen in the timeseries are the sharp increases in the conductivities during the two periods that are exclusively on closed field lines. This is expected given the density increases in the E-region. The SWs remain in the moderate to high range ($100\,\mathrm{m\,s^{-1}}$ to $200\,\mathrm{m\,s^{-1}}$) during these periods, and so there is no evidence, in this event, that hard precipitation nor the subsequent high conductivities suppress the SWs.

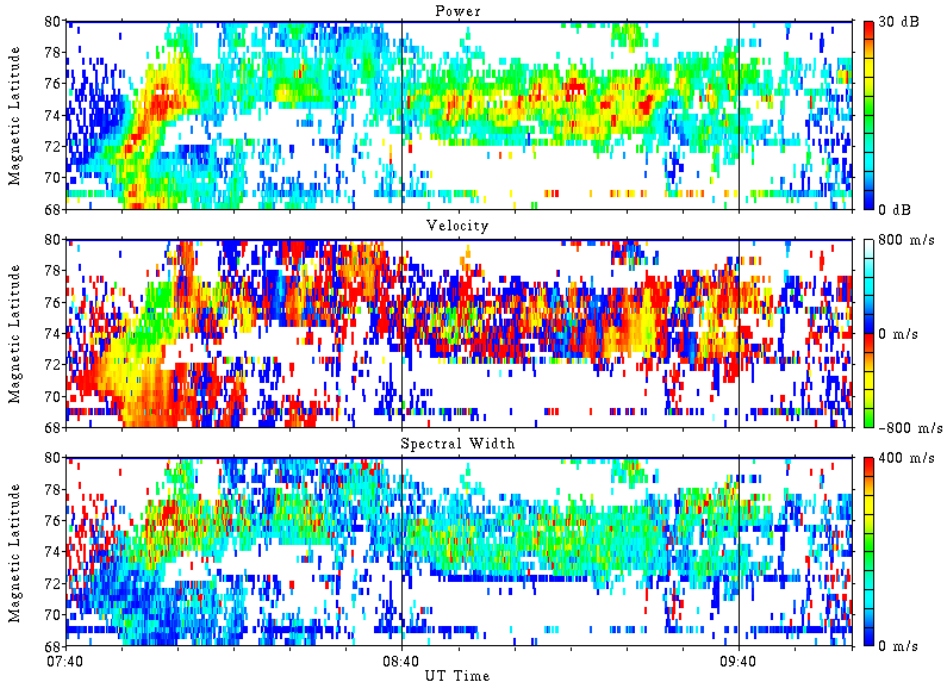

Figure 6.21: Magnetic latitude vs time plots of power, line-of-sight velocity and spectral widths measured by beam 9 of the Hankasalmi radar on the 22nd of December 2003. Velocities towards the radar are positive, away from the radar, negative.

6.3 Statistical analysis

In an ideal situation, with enough events in the different MLT ranges classified according to their position with respect to the OCB, the first step towards a statistical analysis of the data would be to make temperature vs spectral width histograms for the different combinations of MLAT, MLT, and OCB (open or closed field lines) regions. Unfortunately, this is not possible with the dataset available.

The only combination of events that leads to enough data (more than 3 events with at least 6 hours of data combined) is using the 5 events with data in the nightside or the flanks (MLT 12-06h) at MLAT 74-75° (position 1 in figure 5.2). The data in these events are both polarward and equatorward of the OCB. In fact, much of the data is from regions changing quickly between open and close field lines, which makes it impossible to classify it in any meaningful way. However, the temperatures, particularly the electron temperatures, are indicative of the amount of energy input to the ionosphere (and thus the precipitation flux). Precipitation along open field lines only happens in the dayside region, and since this data is not included, it is a good approximation to assume that the electron temperature changes are only created by precipitation along closed field lines. Frictional heating can also cause temperature increases, but it is not as common.

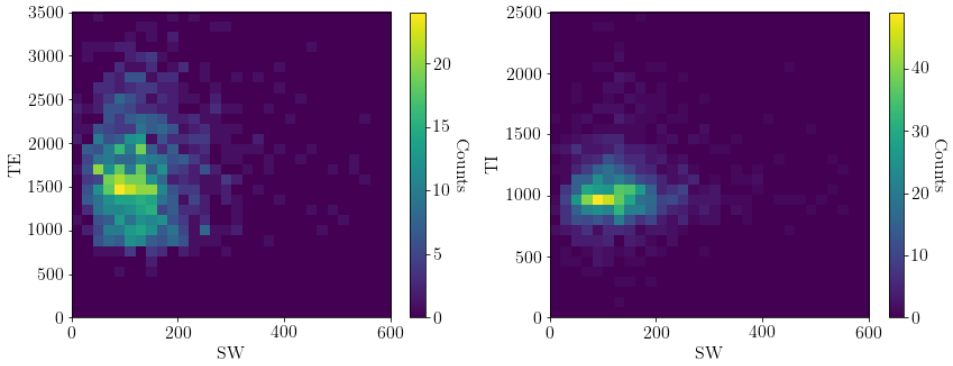

Figure 6.22: Histograms showing electron temperature (left) and ion temperature (right) versus SW for 5 events on the nigthside and the flanks.

The histograms for the aggregated data from these 5 events is shown in figure 6.22. The electron temperatures range from approximately 700K to 3000K, while the ion temperatures have a much narrower range between 700K and 1500K. Neither the average spectral width nor the distribution around this average seems to change substantially with the temperatures.

The fact that the spectral widths do not decrease at high electron temperatures (above ∼2000K) could indicate that high-energy particle precipitation does not suppress high SW. There is, however, a problem with this conclusion: There are few datapoints with high electron temperatures and the ion temperatures are low for virtually all datapoints. One explanation for this is that the flux of high-energy precipitation remains low throughout the

data periods included. This is also consistent with most of the data being from the flanks, since most high-energy particles will precipitate in the nightside sector. Additionally, the latitudes at which the data are obtained are usually polarward of the auroral oval and thus, high flux precipitation is not frequent. What can be concluded from these histograms is only that a low flux of high-energy precipitation does not necessarily lower spectral widths.

Chapter 7

Conclusion and further research

For the events included in this thesis, spectral widths are not strongly correlated with electron temperatures, and thus with particle precipitation. We find instances of periods with high flux high-energy precipitation without the suppression of SWs that has been reported in literature. The lack of correlation between electron temperatures and SWs in the midnight and flank sectors further indicates that high-energy precipitation and elevated SWs can co-exist. It appears, thus, that processes unrelated to particle precipitation play a significant role in the SW variability. There is some evidence pointing to the role of large scale turbulence with varying origins as the cause of high spectral widths in the four case studies reviewed. In one event in the nightside sector, high SWs on open field lines seem to be correlated with polar cap patches merging with the auroral oval. Recent work shows that this merging process can cause turbulence, which would provide a plausible mechanism for the increased SWs observed. In both the dayside and the nightside sectors, there is evidence that some SW increases are correlated with large scale velocity shears on scales larger than the SuperDARN radar range gates. For one of the events in the dayside sector, ion up-flow is observed at the time of a spectral width increase. These velocity shears, both horizontal and vertical, could cause turbulence at scales smaller than the SuperDARN range gates, which would manifest as increased SWs.

Another interesting finding relates to the use of the spectral width boundary as a proxy for the OCB. While there certainly are examples in literature of the SWB closely following the OCB, this thesis proves that this is not always the case. During a 20 minute period in the midnight sector, the SWB is located exclusively on closed field lines. Our results show that the SWB is not always a reliable proxy for the OCB in the midnight sector. The fact that this lack of agreement between the OCB and the SWB happens during a substorm might be relevant, and is something that warrants further study.

In this thesis we set out to provide evidence on the causes of the high SWs seen in the polar ionosphere. What was originally expected to be a statistical study developed into four case studies, due to the size of the dataset after the data processing was completed.

This illustrates the difficulties when combining datasets from different instruments with different operating parameters, strengths and weaknesses. To make similar studies more successful, the study design should be modified in a way that maximizes the odds of gathering a large dataset. To study the role of high-energy precipitation on SWs, using data from SuperDARN/ISR radar pairs in auroral latitudes would give the highest chances of success. The Tromsø EISCAT radar in Norway and the SuperDARN radar in Pikkvibaer, Iceland, are an example of a radar pair with overlapping fields-of-view in auroral latitudes. Another option would be to use overlapping SuperDARN/ISR data from only the mid-latitudes. The advantage with this option is that one could assume that the measurements were always taken on closed field lines which would remove the need for optical data. Most data would be located equatorward of the oval, thus without precipitation and of limited interest, with precipitation only present in periods of increased solar activity. However, there would be no need to manually check optical data, making it very easy to filter large quantities of data and, potentially, end up with a dataset large enough for a statistical study. This method, however, would not work if one wishes to study the role of precipitation in the cusp. It is not possible to exclude regions on closed field lines while including the latitudes at which the cusp is found, since the location of the cusp is highly dynamic. To study the effect of soft cusp precipitation on SWs in a statistical manner, an algorithm to detect the OCB, either from MSP or satellite data would be needed.

Bibliography

Aikio, A.T., Pitkänen, T., Kozlovsky, A., Amm, O., 2006. Method to locate the polar cap boundary in the nightside ionosphere and application to a substorm event. Annales Geophysicae 24, 1905–1917. doi:10.5194/angeo-24-1905-2006.

André, R., Pinnock, M., Villain, J.P., Hanuise, C., 2000. On the factors conditioning the doppler spectral width determined from superdarn hf radars. International Journal of Geomagnetism and Aeronomy 2, 77–86.

André, R., Pinnock, M., Villain, J.P., Hanuise, C., 2002. Influence of magnetospheric processes on winter hf radar spectra characteristics. Annales Geophysicae 20. doi:10.5194/angeo-20-1783-2002.

Baddeley, L., 2019. Course Compendium, UNIS AGF223: Radar Systems for Ionospheric Research.

Baker, K.B., Dudeney, J.R., Greenwald, R.A., Pinnock, M., Newell, P.T., Rodger, A.S., Mattin, N., Meng, C.I., 1995. Hf radar signatures of the cusp and low-latitude boundary layer. Journal of Geophysical Research: Space Physics 100, 7671–7695. doi:10.1029/94JA01481.

Baker, K.B., Wing, S., 1989. A new magnetic coordinate system for conjugate studies at high latitudes. Journal of Geophysical Research: Space Physics 94, 9139–9143. doi:10.1029/JA094iA07p09139.

Baumjohann, W., Treumann, R.A., 1997. Basic space plasma physics. Imperial College Press.

Blanchard, G.T., Lyons, L.R., Samson, J.C., Rich, F.J., 1995. Locating the polar cap boundary from observations of 6300 Å auroral emission. Journal of Geophysical Research: Space Physics 100, 7855–7862. doi:10.1029/94JA02631.

Blanchard, G.T., Sundeen, S., Baker, K.B., 2009. Probabilistic identification of high-frequency radar backscatter from the ground and ionosphere based on spectral characteristics. Radio Science 44. doi:10.1029/2009RS004141.

Bland, E.C., 2016. High frequency remote sensing of Pc5 ultra-low frequency waves using the Super Dual Auroral Radar Network. Ph.D. thesis. La Trobe University, Australia.

Brekke, A., 2013. Physics of the Upper Polar Atmosphere. Second ed., Springer.

Chen, X.C., Lorentzen, D.A., Moen, J.I., Oksavik, K., Baddeley, L.J., Lester, M., 2016. F region ionosphere effects on the mapping accuracy of superdarn hf radar echoes. Radio Science 51, 490–506. doi:10.1002/2016RS005957.

Chisham, G., Freeman, M., 2003. A technique for accurately determining the cusp-region polar cap boundary using superdarn hf radar measurements. Annales Geophysicae 21, 983–996. doi:10.5194/angeo-21-983-2003.

Chisham, G., Freeman, M., Lam, M.M., Abel, G., Sotirelis, T., Greenwald, R., Lester, M., 2005a. A statistical comparison of superdarn spectral width boundaries and dmsp particle precipitation boundaries in the afternoon sector ionosphere. Annales Geophysicae 23, 3645–3654. doi:10.5194/angeo-23-3645-2005.

Chisham, G., Freeman, M.P., 2004. An investigation of latitudinal transitions in the superdarn doppler spectral width parameter at different magnetic local times. Annales Geophysicae 22, 1187–1202. doi:10.5194/angeo-22-1187-2004.

Chisham, G., Freeman, M.P., Sotirelis, T., 2004. A statistical comparison of superdarn spectral width boundaries and dmsp particle precipitation boundaries in the nightside ionosphere. Geophysical Research Letters 31. doi:10.1029/2003GL019074.

Chisham, G., Freeman, M.P., Sotirelis, T., Greenwald, R.A., Lester, M., Villain, J.P., 2005b. A statistical comparison of superdarn spectral width boundaries and dmsp particle precipitation boundaries in the morning sector ionosphere. Annales Geophysicae 23, 733–743. doi:10.5194/angeo-23-733-2005.

Chisham, G., Yeoman, T.K., Sofko, G.J., . mapping ionospheric backscatter measured by the superdarn hf radars; part 1: A new empirical virtual height model .

Clausen, L., 2014. Lecture notes FYS3610. UiO. URL: https://www.uio.no/studier/emner/matnat/fys/nedlagte-emner/FYS3610/h14/documents/handouts/h03.pdf.

Dong, X.C., Dunlop, M.W., Trattner, K.J., Wang, T.Y., Pu, Z.Y., Zhao, J.S., Cao, J.B., Giles, B., Russell, C.T., 2019. Electron sublayers and the associated magnetic topologies in the inner low-latitude boundary layer. Geophysical Research Letters 46, 5746–5753. doi:10.1029/2019GL081998.

Frey, H., Han, D.s., Kataoka, R., Lessard, M., Milan, S., Nishimura, Y., Strangeway, R., Zou, Y., 2019. Dayside aurora. Space Science Reviews 215. doi:10.1007/s11214-019-0617-7.

Gurnett, D.A., Bhattacharjee, A., 2005. Introduction to plasma physics: with space and laboratory applications. Cambridge University Press.

Huber, M., Sofko, G.J., 2000. Small-scale vortices in the high-latitude f region. Journal of Geophysical Research: Space Physics 105, 20885–20897. doi:10.1029/1999JA000417.

Jin, Y., Moen, J.I., Miloch, W.J., 2014. Gps scintillation effects associated with polar cap patches and substorm auroral activity: direct comparison. Journal of Space Weather Space Climate 4, A23. doi:10.1051/swsc/2014019.

Kelley, M.C., 2009. The earths ionosphere: plasma physics and electrodynamics. Academic Press.

Kivelson, M.G., Russell, C.T., 1995. Introduction to space physics. Cambridge University Press.

Lester, M., Milan, S.E., Besser, V., Smith, R., 2001. A case study of hf radar spectra and 630.0 nm auroral emission in the pre-midnight sector. Annales Geophysicae 19, 327–339.

Moen, J., Carlson, H.C., Milan, S.E., Shumilov, N., Lybekk, B., Sandholt, P.E., Lester, M., 2000. On the collocation between dayside auroral activity and coherent hf radar backscatter. Annales Geophysicae 18, 1531–1549. doi:10.1007/s00585-001-1531-2.

Moen, J., Evans, D., Carlson, H.C., Lockwood, M., 1996. Dayside moving auroral transients related to llbl dynamics. Geophysical Research Letters 23, 3247–3250. doi:10.1029/96GL02766.

Moen, J.I., 2004. Lecture notes FYS3610. UiO. URL: https://www.uio.no/studier/emner/matnat/fys/nedlagte-emner/FYS3610/h04/undervisningsmateriale.

Newell, P.T., Ruohoniemi, J.M., Meng, C.I., 2004. Maps of precipitation by source region, binned by imf, with inertial convection streamlines doi:10.1029/2004JA010499.

Parkinson, M.L., Chisham, G., Pinnock, M., Dyson, P.L., Devlin, J.C., 2004. Magnetic local time, substorm, and particle precipitation-related variations in the behaviour of SuperDARN Doppler spectral widths. Annales Geophysicae 22, 4103–4122.

Ponomarenko, P., Waters, C., 2003. The role of pc1-2 waves in spectral broadening of superdarn echoes from high latitudes. Geophysical Research Letters - GEOPHYS RES LETT 30, 22–1. doi:10.1029/2002GL016333.

Ponomarenko, P., Waters, C., Menk, F., 2007. Factors determining spectral width of hf echoes from high latitudes. Annales Geophysicae 25. doi:10.5194/angeo-25-675-2007.

Ponomarenko, P.V., Waters, C.L., 2006. Spectral width of superdarn echoes: measurement, use and physical interpretation. Annales Geophysicae 24, 115–128. doi:10.5194/angeo-24-115-2006.

Richmond, A.D., 2007. Ionosphere. Springer Netherlands, Dordrecht. pp. 452–454. doi:10.1007/978-1-4020-4423-6_159.

Rodger, A., 2000. Ground-based imaging of magnetospheric boundaries. Advances in Space Research 25, 1461–1470. doi:10.1016/S0273-1177(99)00657-2.

Russell, C., 2001. The dynamics of planetary magnetospheres. Planetary and Space Science 49, 1005 – 1030. doi:https://doi.org/10.1016/S0032-0633(01)00017-4. magnetosphere of the Outer Planets Part II.

Schiffler, A., Sofko, G., Newell, P.T., Greenwald, R., 1997. Mapping the outer llbl with superdarn double-peaked spectra. Geophysical Research Letters 24, 3149–3152. doi:10.1029/97GL53304.

Schunk, R.W., Nagy, A.F., 2000. Collisions. Cambridge University Press. Cambridge Atmospheric and Space Science Series, p. 66–103. doi:10.1017/CBO9780511551772.004.

Shepherd, S.G., 2014. Altitude-adjusted corrected geomagnetic coordinates: Definition and functional approximations. Journal of Geophysical Research: Space Physics 119, 7501–7521. doi:10.1002/2014JA020264.

Sigernes, F., Holmen, S.E., Dyrland, M., Bækken, A.L., Brekke, P., Chernouss, S., Lorentzen, D.A., Deehr, C.S., 2012. Auroral oval forecast on mobile platforms. URL: http://kho.unis.no/doc/Sigernes_Ovals_50ARS.pdf. 50 Years of Science - Anniversary Symposium at Andøya Rocket Range.

Sotirelis, T., Ruohoniemi, J.M., Barnes, R.J., Newell, P.T., Greenwald, R.A., Skura, J.P., Meng, C.I., 2005. Comparison of superdarn radar boundaries with dmsp particle precipitation boundaries. Journal of Geophysical Research: Space Physics 110. doi:10.1029/2004JA010732.

Villain, J.P., André, R., Pinnock, M., Greenwald, R., Hanuise, C., 2002. A statistical study of the doppler spectral width of high-latitude ionospheric f-region echoes recorded with superdarn coherent hf radars. Annales Geophysicae 20. doi:10.5194/angeo-20-1769-2002.

Woodfield, E., Davies, J., Eglitis, P., Lester, M., 2002. A case study of hf radar spectral width in the post midnight magnetic local time sector and its relationship to the polar cap boundary. Annales Geophysicae 20. doi:10.5194/angeo-20-501-2002.

Yeoman, T.K., Chisham, G., Baddeley, L.J., Dhillon, R.S., Karhunen, T.J.T., Robinson, T.R., Senior, A., Wright, D.M., 2008. Mapping ionospheric backscatter measured by the superdarn hf radars; part 2: Assessing superdarn virtual height models. Annales Geophysicae 26, 843–852. doi:10.5194/angeo-26-843-2008.

Appendix

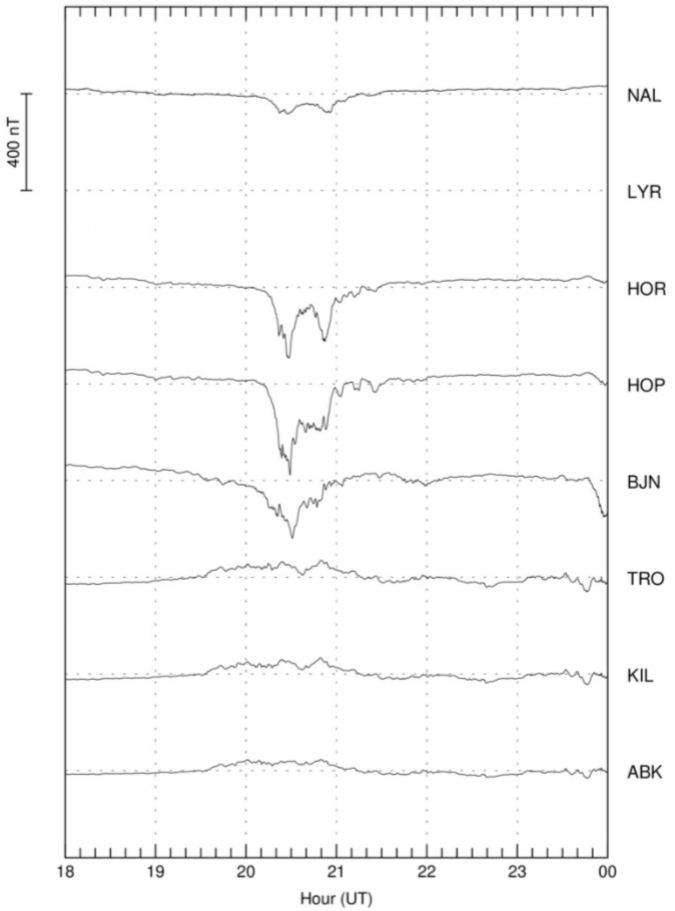

Figure 7.1: North-south component of the magnetic field on the surface of the Earth as measured by magnetometers of the IMAGE network on the 8th of January 2008. Stations, from top to bottom: Ny-Ålesund, Longyearbyen (missing), Hornsund, Hopen, Bjørnøya, Tromsø, Kilpisjärvi, Abisko.

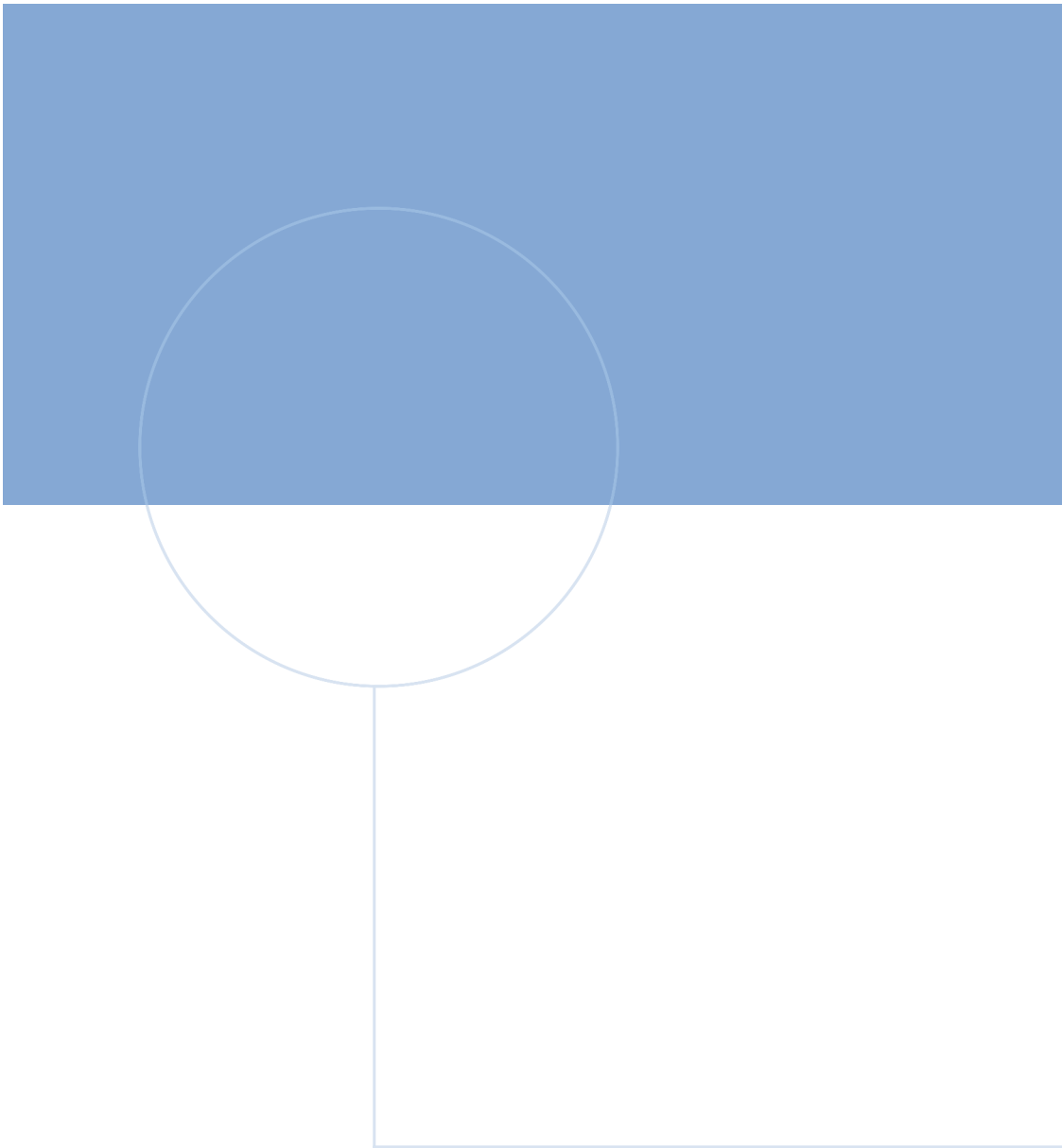

NTNU
Norwegian University of
Science and Technology

UNIS